3 Results and discussion

Summary

This chapter contains the discussion of the results concerning the development of ODS bondcoats and the investigation on the mechanisms of formation of Cr-rich diffusion coatings. As far as the development of ODS bondcoats is concerned, the results of the characterization tests performed on the milled powders are explained first. Then the discussion focuses on the characterization of ODS coatings and the evaluation of their high temperature behavior. In particular, *section one* concerns the deposition of ODS coatings by APS and HVOF using the M20 and M30 powders (see Section 2.1.1). Different process parameters are examined. The oxidation mechanisms and the thermal cycling resistance of hybrid TBCs are then discussed.

Section two concerns the analysis of full ODS bondcoats and thin ODS layers deposited with modified powder batches N10, N20 and N30 (Section 2.1.1). After the microstructural investigation, the analysis of the isothermal oxidation resistance is examined.

As far as the development of Cr-rich diffusion coatings is concerned, the analysis of the results starts with the characterization tests performed on the pack-mix components before and after the pack-chromizing process (Section 2.2). The discussion then shifts to the detailed investigation of the effect of the process parameters on the mechanisms of formation of diffusion coatings.

3.1 Development of ODS bondcoats

3.1.1 Powder analysis

Section one

Effect of the milling time

The particle size distribution curve related to the sample M20 milled for 1 hour is trimodal (fig. 3.1.1b). As confirmed by the optical microscope pictures (fig. 3.1.1a), this particular distribution curve indicates that completely distinct powder particles (pure CoNiCrAlY powder and pure ceramic particles) are still present. This occurs because during the first step of the milling cycle the collisions between the milling media and the powder led mostly to the flattening of the ductile particles and to the refinement of the hard phase fraction [1,2]. In the early stages of the process the welding and alloying mechanisms only affected a limited amount of particles. The alloyed particles consist of a layered structure, based on flattened metal lamellae surrounded by oxides. The microstructure is not homogenous and the oxide regions feature a large number of pores.

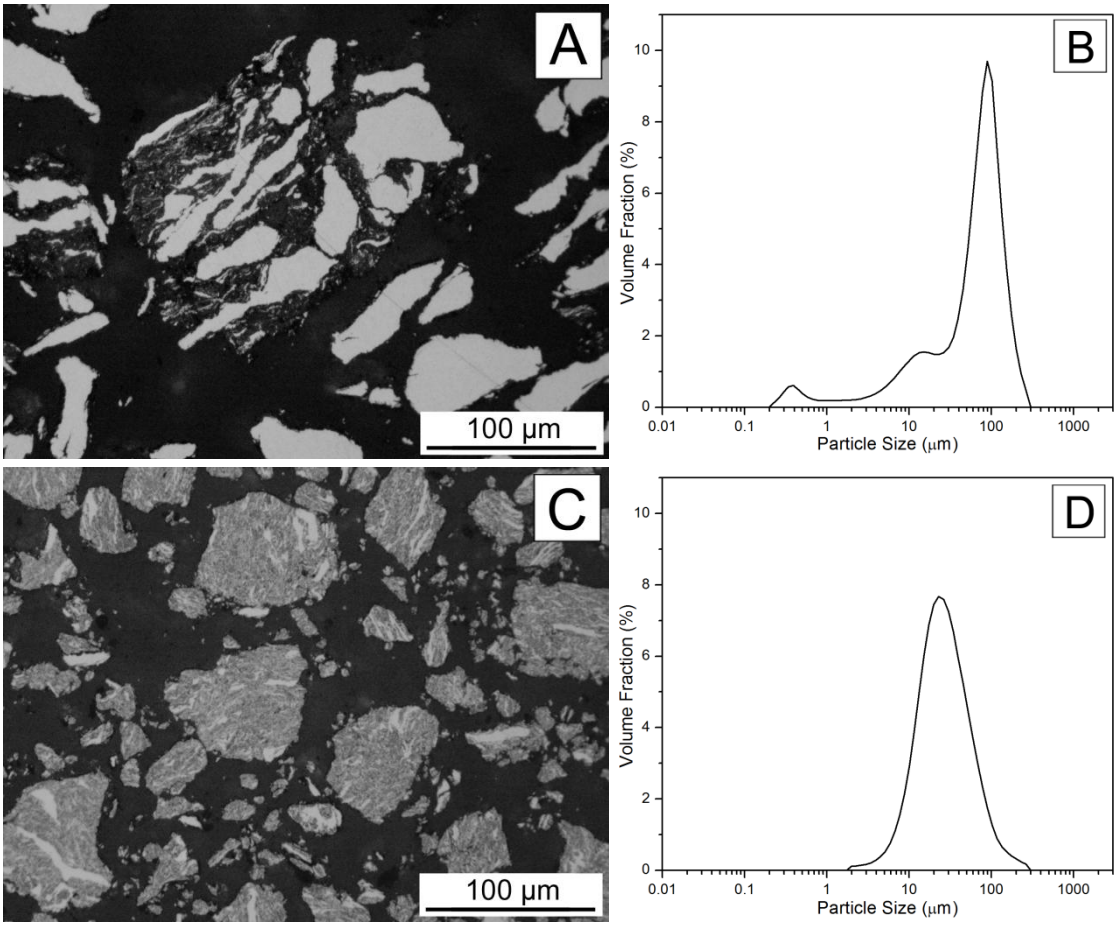

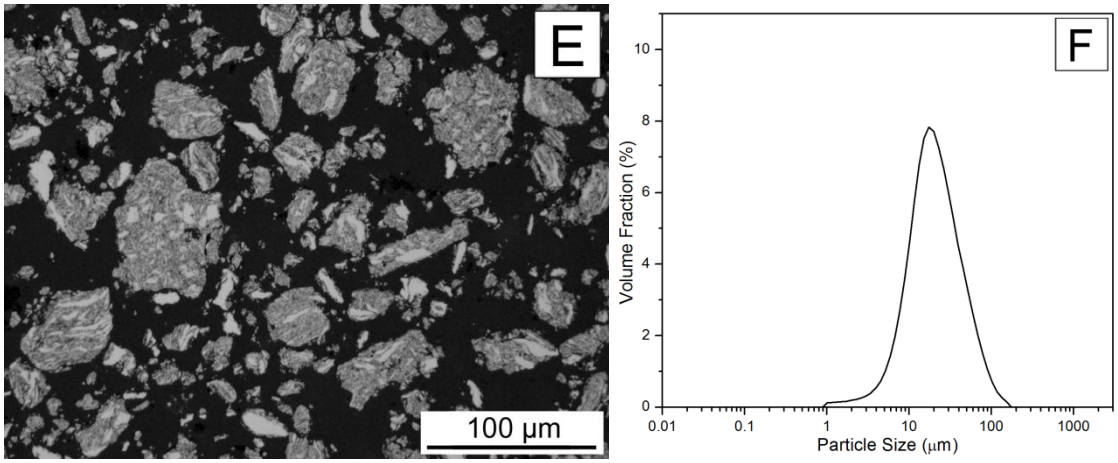

Figure 3.1.1 – optical microscope images and particle size distribution curves of the ODS powder M20 (20 wt.% of Al_2O_3) milled at 1600 rpm for 1 hour (a,b), 4 hours (c,d) and 6 hours (e,f).

Increasing the milling time made the particle size distribution curve narrower (fig. 3.1.1c,d): after 4 hours particles exhibit a more homogeneous microstructure and morphology. Unalloyed particles are now barely visible. The continuous ball-powder collisions promoted cold welding, fracturing and rewelding phenomena, leading to a refinement of the powder microstructure. The intrinsic nature of the selected phases, i.e. a ductile material and a hard phase, gradually led to the inclusion of the small oxide particles inside the metal matrix.
Powders milled for 5 and 6 hours (fig. 3.1.1e,f) are very similar to the powders milled for 4 hours. The particle size distribution is only slightly finer.

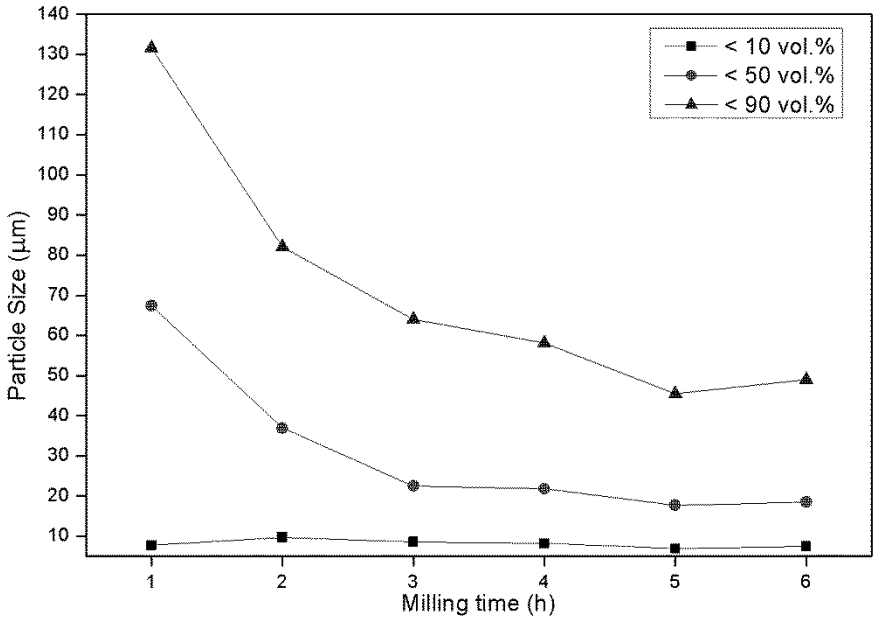

Figure 3.1.2 – percentile results (D10, D50, D90) of the six powder batch (M20, ConiCrAlY-Al_2O_3 80-20 wt. %) as a function of the milling time.

Fig. 3.1.2 shows the percentile results (D10, D50, D90) of the six powder batches (M20, CoNiCrAlY-Al_2O_3 80-20 wt. %) as a function of the milling time. As previously mentioned, the particle size of the powder batches decreases increasing the milling time, up to 3 hours. After that time no important changes in the particle dimension were detected, apart from a slight refinement.

Optical microscope images (fig. 3.1.1) show the evolution of the particle microstructure during the milling process. The lamellar structure of powders milled for 1-2 hours was gradually converted into a more homogeneous microstructure, in which the hard phase is better embedded inside the metal matrix.

A milling time of 4 hours was found to be a good compromise between the particle microstructure and the duration of the milling process.

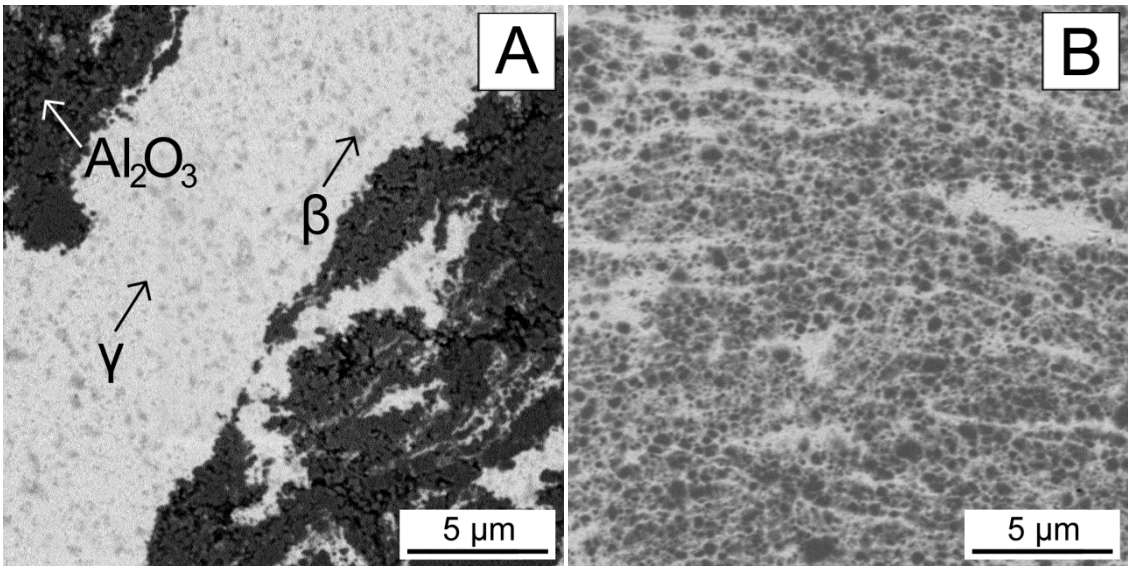

Figure 3.1.3 – SEM pictures of ODS powder M20 after 1 hour (a) and 4 hours (b) milling at 1600rpm.

SEM pictures (fig. 3.1.3) also reveal differences in the crystallographic main phases: after 4 hours milling, the β-(Ni,Co) phase, which was easily detected in the CoNiCrAlY powder used as a metal matrix (XRD pattern in fig. 3.1.4) and in the powder milled for 1 hour (SEM picture in fig. 3.1.3a), is barely visible (fig. 3.1.3b and XRD patterns in fig. 3.1.4). This variation was probably caused by the transformation of the ductile phase microstructure that took place during the milling process, due to cold welding, fragmentation and rewelding phenomena and due to the embedding of the hard particles inside the metal matrix. These assumptions are confirmed by previous investigations concerning the mechanical milling of CoNiCrAlY powders, which reveals the dissolution of the β-phase as well [3,4]

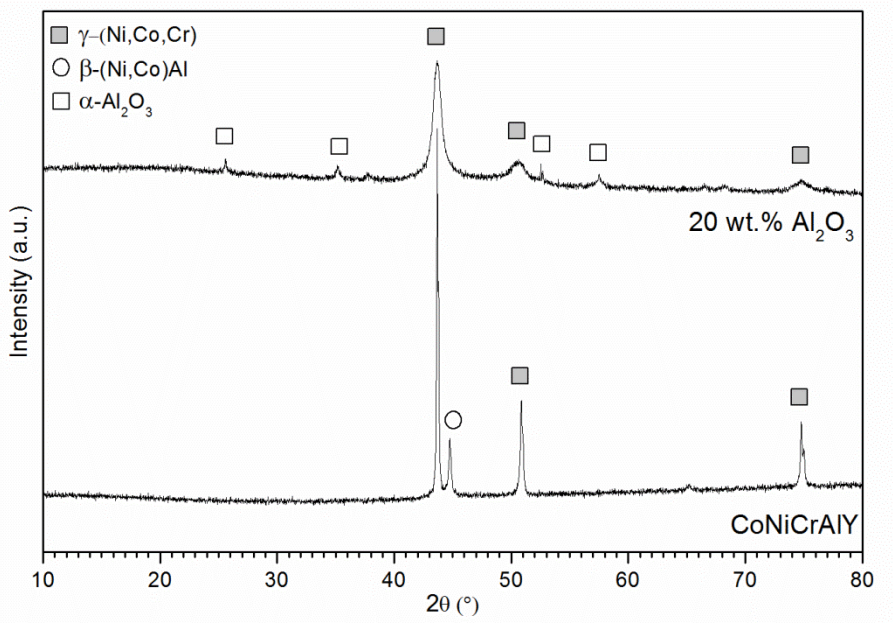

Figure 3.1.4 – XRD patterns of the CoNiCrAlY powder used as metal matrix and ODS powder containing 20 wt.% of alumina after 4 hours milling.

These phenomena are also responsible of the broadening of the peaks in the XRD patterns reported in fig. 3.1.4, caused by the work hardening of the CoNiCrAlY matrix, which results in the accumulation of lattice defects due to the large plastic strain and/or in the formation of much finer recrystallised grains.

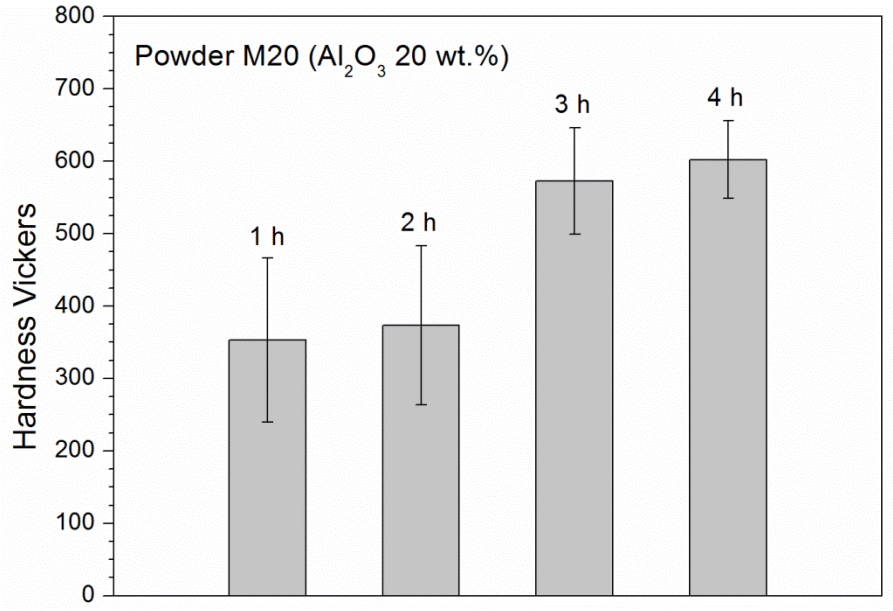

Figure 3.1.5 – Hardness values of the ODS powder containing 20 wt.% of alumina plotted as a function of the milling time

The evolution of the microstructure of the milled powders during the process is also shown in fig. 3.1.5, which contains the Vickers hardness values plotted as a function of the milling time.

The hardness of the particles increases according to the milling time, due to the continuous embedding of the hard phase within the CoNiCrAlY matrix and due to the work hardening phenomena which affected the metal phase.

Effect of the milling speed

The particle size distribution curves (fig. 3.1.6b,d) of powders milled at 1200 and 1400 rpm (labeled M20-I and M20-II respectively) show that reducing the process speed affected the particle size, because the energy generated by the ball-particle collisions changed. Both batches show bimodal particle size distribution curves even after 4 hours milling, indicating the presence of both alloyed and unalloyed particles, as previously discussed.

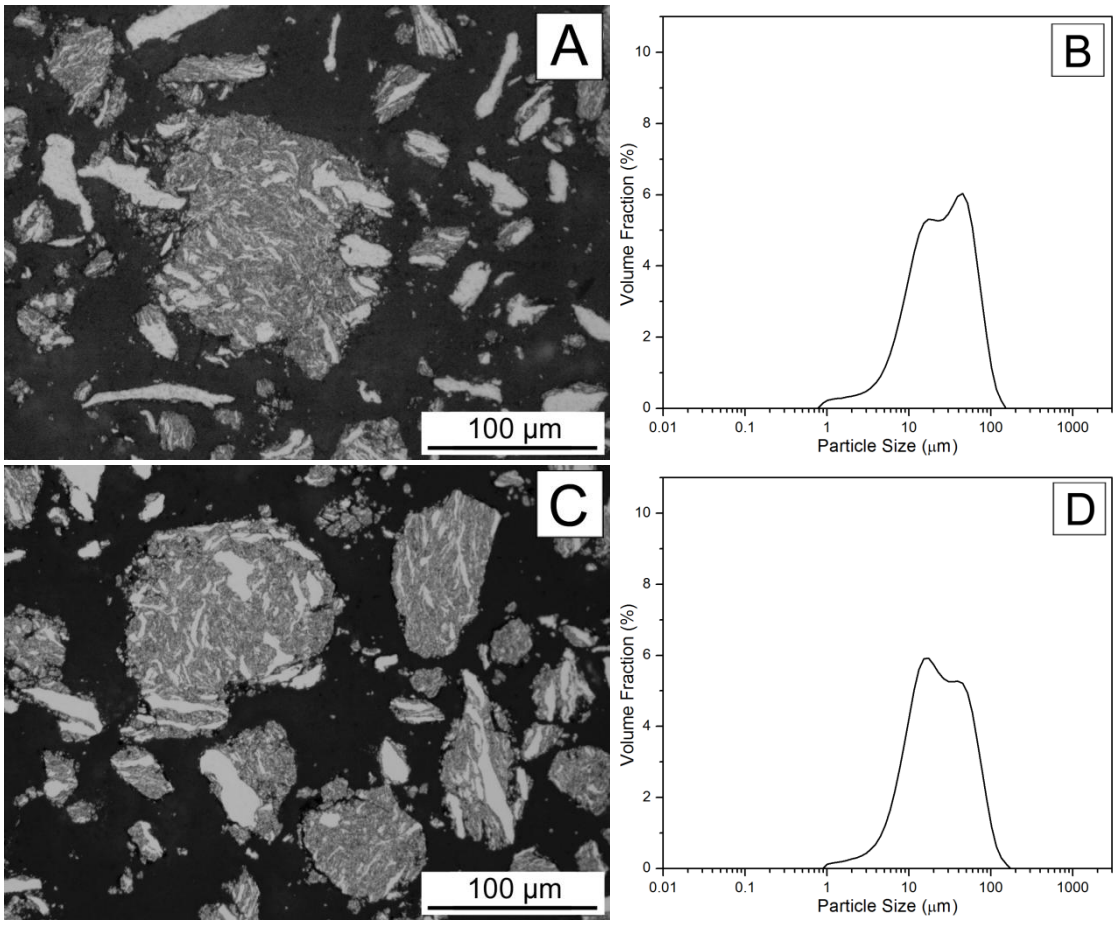

Figure 3.1.6 – optical microscope images and particle size distribution curves of powders milled at 1200 rpm (a,b) and at 1400 rpm (c,d) for 4 hours.

The optical microscope images (fig. 3.1.6a,c) confirm the previous assumptions, revealing a high amount of pure metal lamellae and partially alloyed particles even at the end of the milling process (4 hours).

Therefore a milling speed of 1600 rpm together with a process time of 4 hours was found to be the best parameters for producing ODS-powders.

Effect of the oxide phase amount

The higher content of CoNiCrAlY powder (90 wt. %) inside the sample M10 led to an increase of the particle size (fig. 3.1.7b). This occurs because the higher fraction of ductile phase promoted agglomeration and welding phenomena during the milling process.

The pictures taken by optical microscope (fig. 3.1.7a) show a good homogeneity between the hard phase and the metal matrix even if some flattened metal particles are still present.

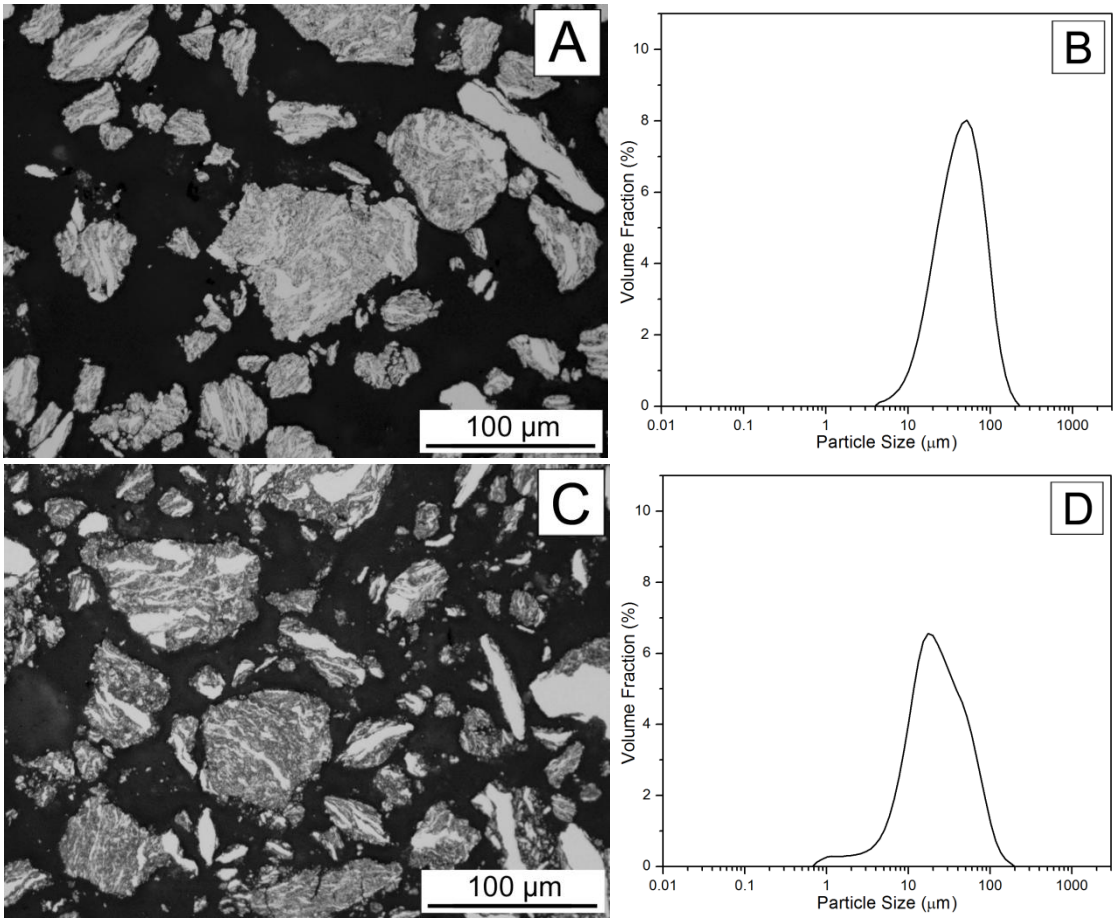

Figure 3.1.7 – optical microscope images and particle size distribution curves of powders M10 (a,b) and M30 (c,d) milled at 1600 rpm for 4 hours.

The comparison between samples containing different amounts of alumina (10, 20 and 30 wt. %) reveals that increasing the hard phase amount brought to finer powders (after a 4 hours milling cycle), because increasing the alumina concentration made the particles more brittle and promoted fragmentation phenomena (fig. 3.1.7d).

Optical microscope images (fig. 3.1.7c) clearly reveal the higher fraction of hard phase embedded in the metal matrix even if this did not affect the microstructure, which is very similar to the previously observed powder batches.

Section two

Section 2 contains the results of the microstructural investigation performed on the modified powder batches N10, N20, N30, containing different amounts of alumina and different sources of starting materials.

These powder batches were obtained using a slightly higher ball-to-powder mass ratio.

Regardless of the alumina source and amount, all the three powder batches (labeled N10, N20 and N30 respectively) show a similar microstructure. The particle size distribution curve of each powder is affected by the amount of the hard phase, because it affects the agglomeration/fragmentation phenomena during the process (fig. 3.1.8), consistent with the previous observations.

The fragmentation phenomena brought to a decrease of the particle dimensions and to a broadening of the particle size distribution curve. The broadening of the curve mainly affects the finer fraction of the powder (i.e. the left side of the curve), indicating that this phenomenon is caused by the fragmentation of a large amount of powder into finer particles.

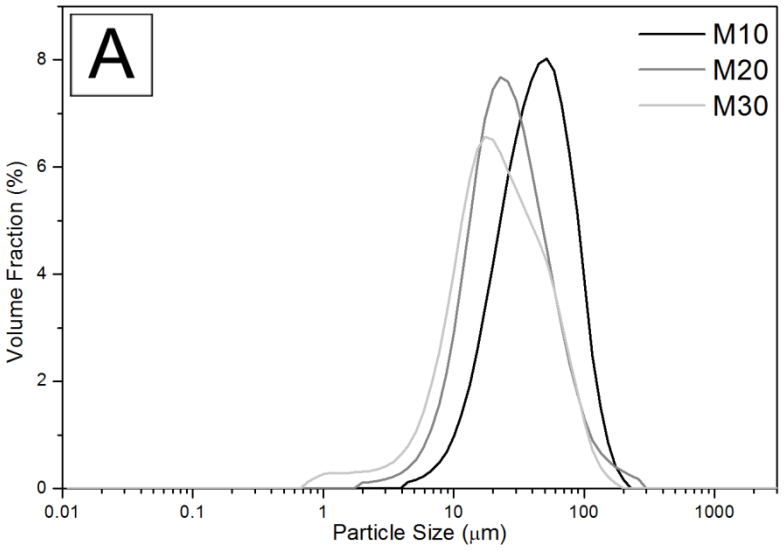

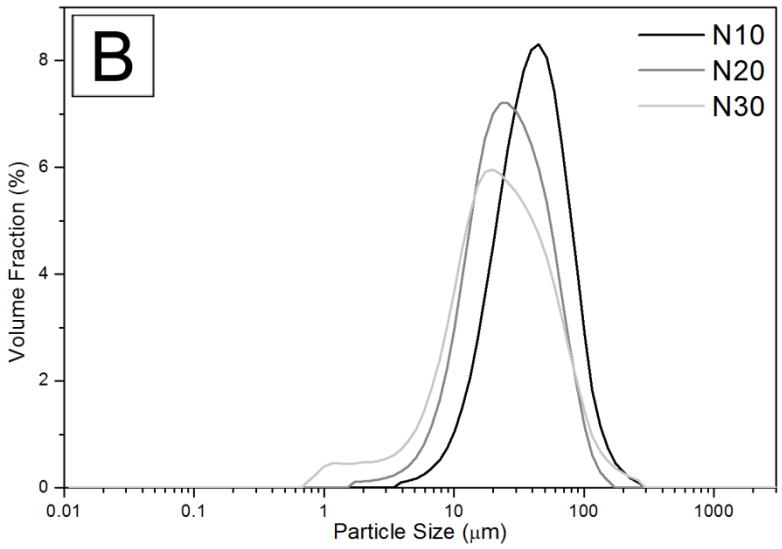

Figure 3.1.8 – Particle size distribution curves of powder batches containing different amount of alumina: plot a shows the ODS powders M10, M20 and M30, plot b shows the ODS powders N10, N20 and N30.

Comments

The different Al_2O_3 sources did not affect the final amount of oxide inclusions embedded within the milled powders. The composition of the different powder batches, determined by EDS measurements on the cross-section of the milled particles, is given in table 3.1.1. In order to improve the accuracy of the EDS analysis in the quantification of Al, the built-in calibration reference for that element was replaced by calibrating the Al peak using an Al alloy of known chemical composition (where the amount of Al was previously determined by quantometric analysis): this way, the matrix effects in the calibration standard and in the samples are similar.

M10, N10 (10 wt.% of Al_2O_3)			**M20, N20 (20 wt.% of Al_2O_3)**			**M30, N30 (30 wt.% of Al_2O_3)**		
Element	**At. %**	**Wt. %**	**Element**	**At. %**	**Wt. %**	**Element**	**At. %**	**Wt. %**
O	9.4	23.82	**O**	16.9	36.57	**O**	22.7	43.76
Al	14.9	22.35	**Al**	19.3	24.78	**Al**	24.2	27.66
Cr	18.1	14.13	**Cr**	15.4	10.26	**Cr**	12.8	7.57
Co	30.9	21.34	**Co**	25.7	15.07	**Co**	21.3	11.14
Ni	26.2	18.12	**Ni**	22.3	13.16	**Ni**	18.5	9.69
Y	0.5	0.23	**Y**	0.4	0.17	**Y**	0.5	0.18

Table 3.1.1 – Results of the EDS analysis performed on the cross-sections of ODS powders containing different amount of alumina

Despite the different amounts of aluminum oxide, no important differences were detected in the XRD patterns of powder batches containing 20 and 30 wt. % of strengthening phase (fig. 3.1.9).

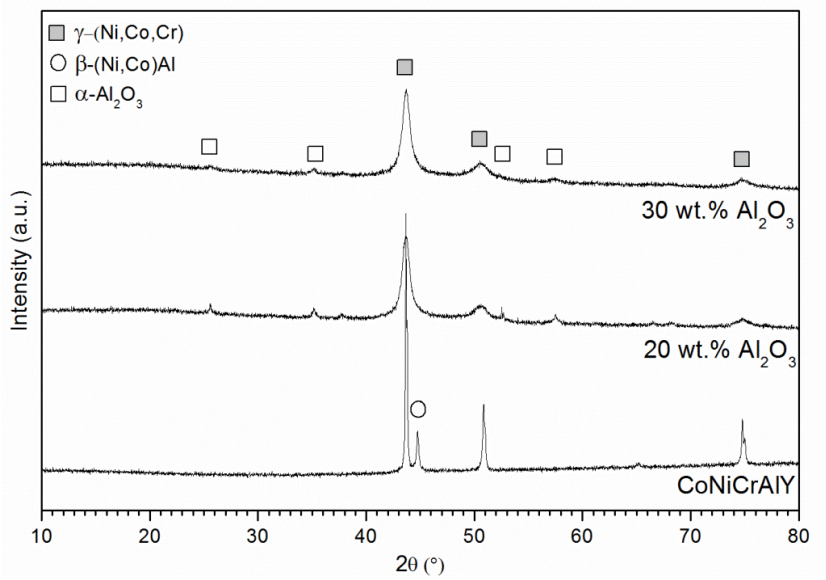

Figure 3.1.9 – XRD patterns of ODS powders containing different amount of alumina. The XRD pattern related to the commercially available CoNiCrAlY powder used as a metal matrix is shown as a comparison.

3.1.2 Coating analysis, Section one

Section one concerns the discussion of the microstructural investigations performed on ODS coatings deposited using the feedstock powders M20 and M30, milled for 4 hours.

A comparison between bondcoats deposited by HVOF and APS is reported.

Then the results of the thermal cycling oxidation test performed on the hybrid TBCs are discussed.

Coating deposited by HVOF

Optical microscope and SEM pictures (fig. 3.1.10a, 3.1.11a) show that the coating M20-H-1 is dense and homogenous, even if some metal particles without alumina inclusions are still present. Despite this, the majority of the coating consists of a composite material based on small oxide particles perfectly embedded in the metal matrix.

Sample	Percent porosity
M20-H-1	1.1
M20-H-2	2.0
M20-H-3	1.5

Table 3.1.2 – Percent porosity calculated by using an image analysis software.

Compared to the coating M20-H-1, the sample M20-H-2 (fig. 3.1.10b) appears less dense, especially near the surface: increasing the spraying distance (from 200 to 250 mm) led to a more porous microstructure, because the higher distance reduces the peening effect. The porosity, calculated using the image analysis software ImageJ, increased from 1.1% up to 2.0% (table 3.1.2).

The peening effect in thermally sprayed coatings consists in the hardening and densification of the coating caused by the continuous impact of droplets on the underlying sprayed layer. This effect mainly occurs in process in which the buildup of the coating depends more on the kinetic energy of the projected particles than on the temperature of the flame (*i.e.* HVOF, Cold Spray).

Increasing nitrogen, oxygen and hydrogen flow rates did not affect the microstructure of the coating M20-H-3 (fig. 3.1.10c), which is very similar to that of the sample M20-H-1.

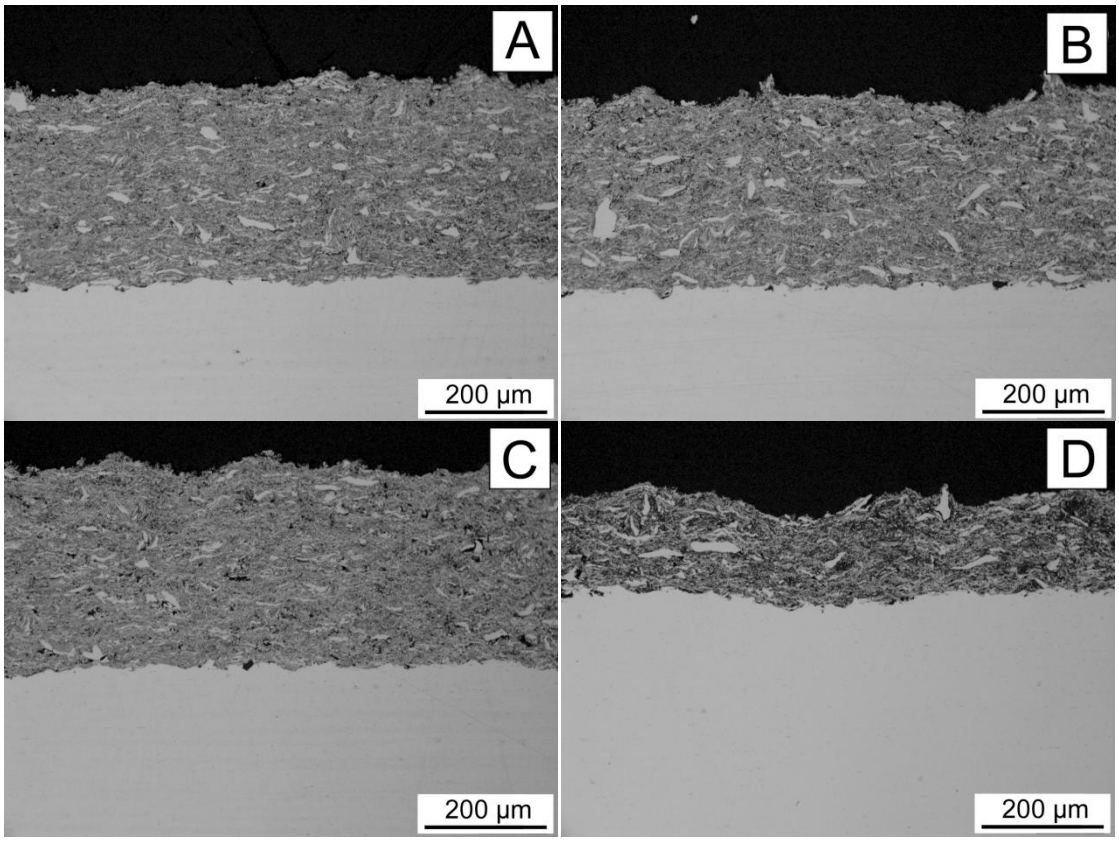

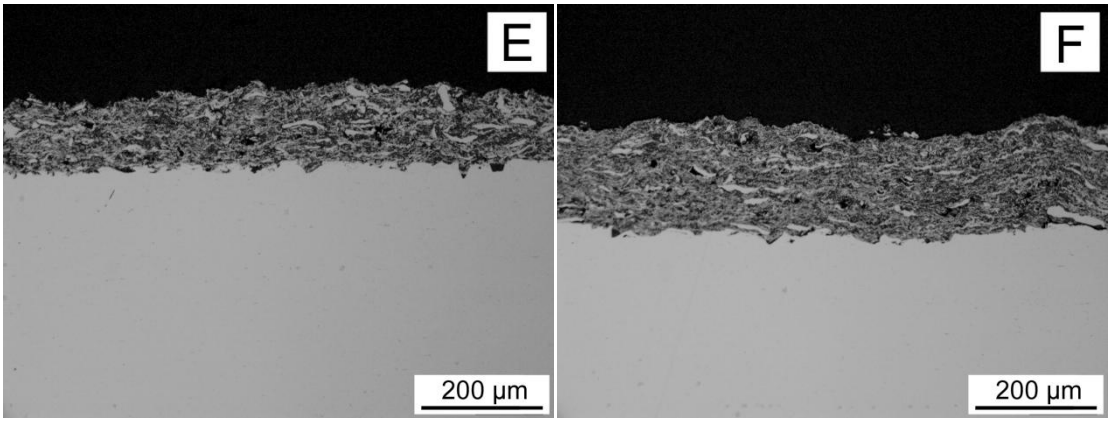

Figure 3.1.10 – Optical microscope images of full ODS coatings deposited by HVOF: M20-H-1 (a), M20-H-2 (b), M20-H-3 (c), M30-H-1 (d), M30-H-2 (e), M30-H-3 (f).

The ODS coatings containing 30 wt.% of Al_2O_3 generally exhibit higher porosity (table 3.1.3) and their microstructure appears more heterogeneous (fig. 3.1.10d,e,f).

Compared to the coatings deposited using the powder M20, the overall thickness of the layers containing the higher fraction of alumina is lower, revealing a reduced deposition efficiency.

Sample	Percent porosity
M30-H-1	2.2
M30-H-2	2.9
M30-H-3	4.9

Table 3.1.3 – Percent porosity calculated by using an image analysis software.

The defects and the lower deposition efficiency are probably caused both by the microstructure of the feedstock powders and by the deposition conditions. The powder M30 features a less homogenous microstructure than that of the powder M20, due to the higher fraction of hard phase; this results in more heterogeneous coatings. Furthermore the harder particles probably needed more energy during the spraying process to buildup a dense coating and the deposition parameters employed were not optimized for that powder batch.

Also in this case, the coating deposited using a spraying distance of 250 mm is less dense than coatings applied with a spraying distance of 200 mm (fig. 3.1.10d,e,f).

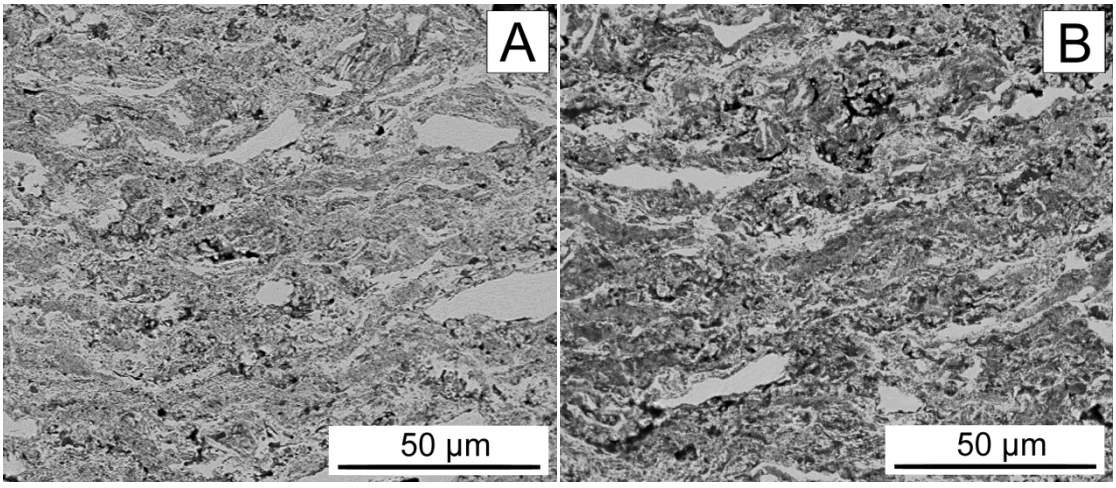

Figure 3.1.11 – SEM pictures of coatings M20-H-1 (a) and M30-H-1 (c).

M20-H-1			M30-H-1		
Element	**Wt.%**	**At.%**	**Element**	**Wt.%**	**At.%**
O	14.61	33.31	**O**	17.5	37.06
Al	17.1	23.11	**Al**	21.22	26.64
Cr	16.4	11.5	**Cr**	14.57	9.49
Co	28.04	17.35	**Co**	25	14.37
Ni	23.4	14.54	**Ni**	21.18	12.22
Y	0.46	0.19	**Y**	0.54	0.21

Table 3.1.4 – Results of the EDS analysis performed on the cross-sections of the ODS coatings

The amount of aluminum, detected by the EDS analysis performed on the cross section of coatings M20-H-1 and M30-H-1 (table 3.1.4), is moderately lower compared to its concentration inside the milled powders (table 3.1.1). This may be due to rebounding of some particles with higher hard phase content during spraying.

It should be clarified that the EDS analysis was performed on the as-sprayed ODS layer and this could result in a different concentration of the elements within the coating. Further investigations (showed in the following sections) revealed that after the vacuum heat treatment, due to interdiffusion phenomena, the aluminum amount in the ODS coating increases.

Furthermore, as previously stated, the microstructure of both powders and coatings is not completely homogenous and therefore the EDS measurements could be affected by heterogeneous regions, such as unalloyed particles and pores.

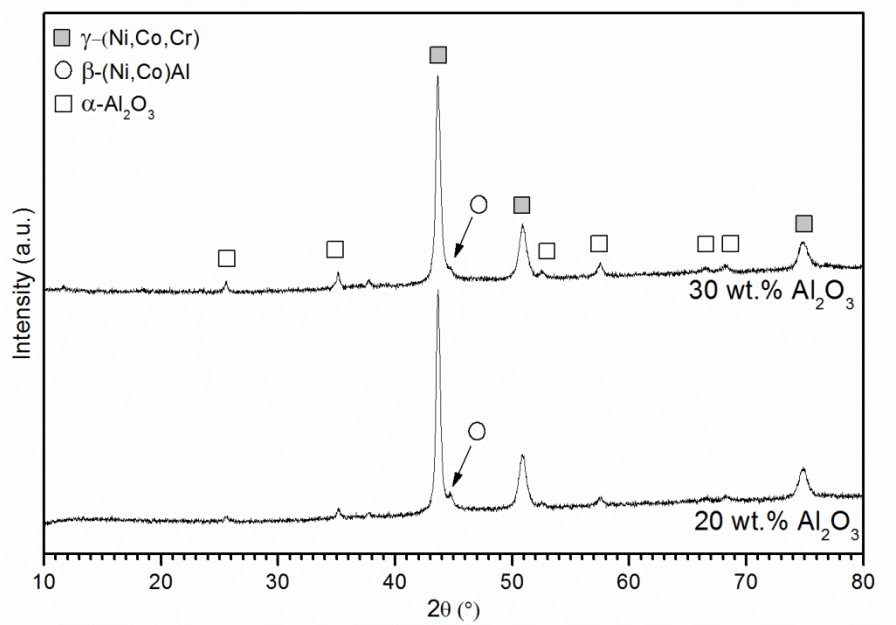

Figure 3.1.12 – XRD patterns of the as sprayed coatings M20-H-1 and M30-H-1.

The XRD patterns (fig. 3.1.12) of the as sprayed freestanding coatings M20-H-1 and M30-H-1 clearly show the α-Al_2O_3 peaks, related to the hardening media, and the γ-(Ni,Co,Cr) phase, related to the metal matrix. The β-(Ni,Co)Al peaks are barely visible. Compared to the XRD patterns of the ODS powders, the diffraction peaks of the as sprayed coatings are narrower, indicating a more ordered crystalline structure. This effect could be caused by the fact that heating of the particles during the deposition process led to a partial recovery of the plastic deformation that affected the particles during the milling procedure.

Despite the different amounts of alumina, the XRD patterns do not show relevant differences between these two freestanding coatings.

Furthermore no phases related to mixed oxides were detected, indicating that oxidation phenomena did not take place to a significant extent during the deposition process.

The Vickers hardness of the ODS coatings is affected by the amount of strengthening phase dispersed within the metal matrix. The sample M30-H-1, due to its higher amount of alumina, features higher hardness values. Compared to the standard bondcoat, both the ODS layers have an increased hardness.

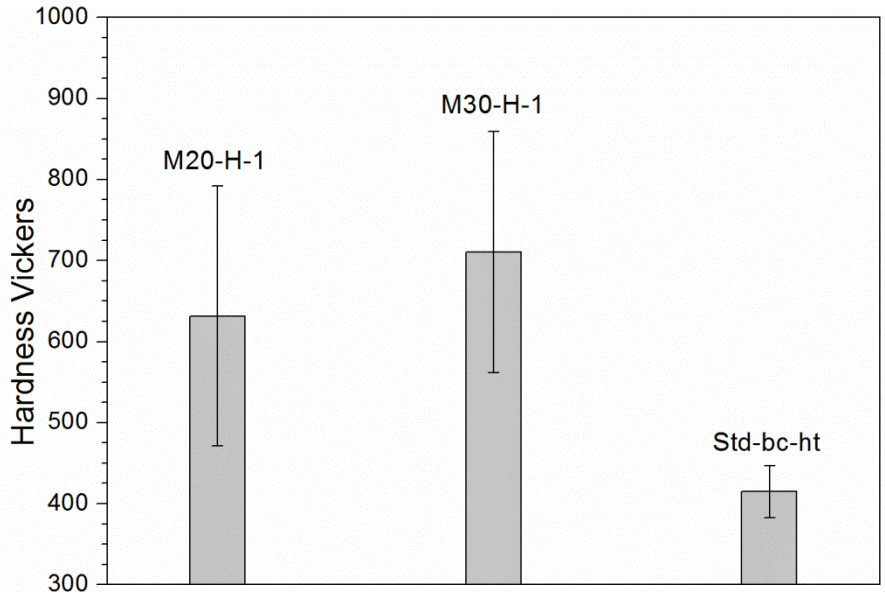

Figure 3.1.13 –Vickers Hardness of a standard bondcoat (Std-bc-ht) and of ODS coatings containing 20 and 30 wt.% of alumina (M20-H-1 and M30-H-1 respectively).

Sample name	Atmosphere	CTE (K^{-1})
M20-H-1	Air	$14.2*10^{-6}$ K^{-1}
M30-H-1	Air	$12.9*10^{-6}$ K^{-1}
M20-H-1	Ar/H_2	$14.6*10^{-6}$ K^{-1}
M30-H-1	Ar/H_2	$12.8*10^{-6}$ K^{-1}

Table 3.1.5 – Coefficient of thermal expansion measured using freestanding ODS bondcoats containing 20 and 30 wt.% of alumina. The CTE was calculated in air and in Ar/H_2 atmosphere.

The CTE, determined in Air and Ar/H_2 atmosphere, is strongly affected by the Al_2O_3 particles embedded inside the CoNiCrAlY matrix (tab. 3.1.5). Alumina has a lower CTE than the CoNiCrAlY alloy, therefore the addition of this oxide reduces the overall CTE of the composite system.

The plot reported in fig. 3.1.14 shows the CTE values of a standard bondcoat, ODS coatings and YSZ ceramic topcoat. It can be easily noticed that the oxide dispersion strengthened systems have a CTE in the range between the pure bondcoat and the ceramic coating. The introduction of an ODS layer could effectively reduce the thermal expansion mismatch among these different layers mitigating the thermal stresses that usually arise upon cooling, during the working life of the TBCs.

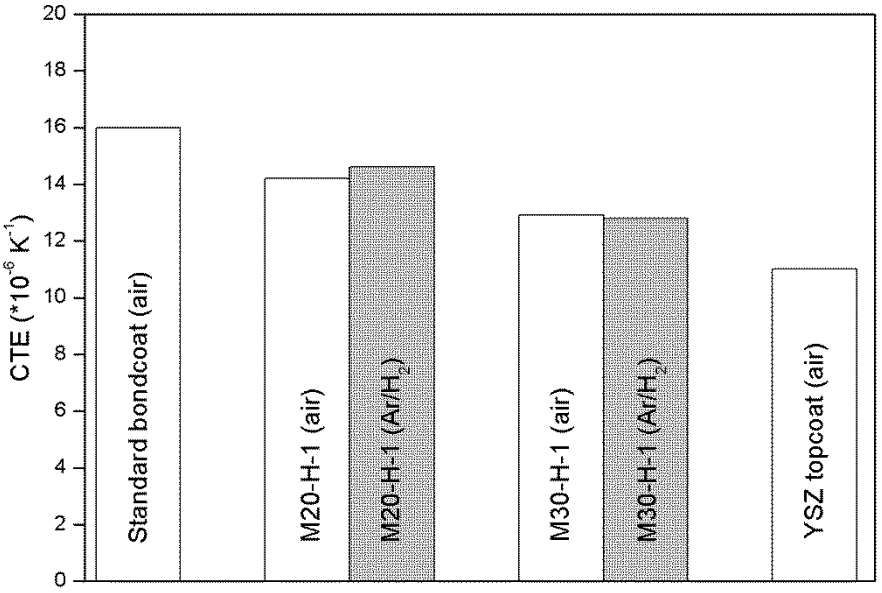

Figure 3.1.14 – CTE of ODS bondcoats containing 20 and 30 wt.% of alumina. These data are also available in table 3.1.5. The CTEs of a standard bondcoat and of a topcoat are plotted as well.

Coating deposited by APS

Coatings deposited by APS are thinner than HVOF coatings and have higher porosity (fig. 3.1.15, table 3.1.6). The deposition efficiency is lower than that of the HVOF process and the coatings are less dense. Moreover the SEM pictures reveal unmelted and non-flattened particles, which contribute to drastically increase the porosity and the defects within the coating. This may be related to the radial injection system employed in APS torches: while some particles are fully melted, others, depending on their size and injection velocity, can either fail to enter the plasma core, remaining in an unmelted condition, or escape the core, resulting in incomplete melting and/or in resolidification before impact.

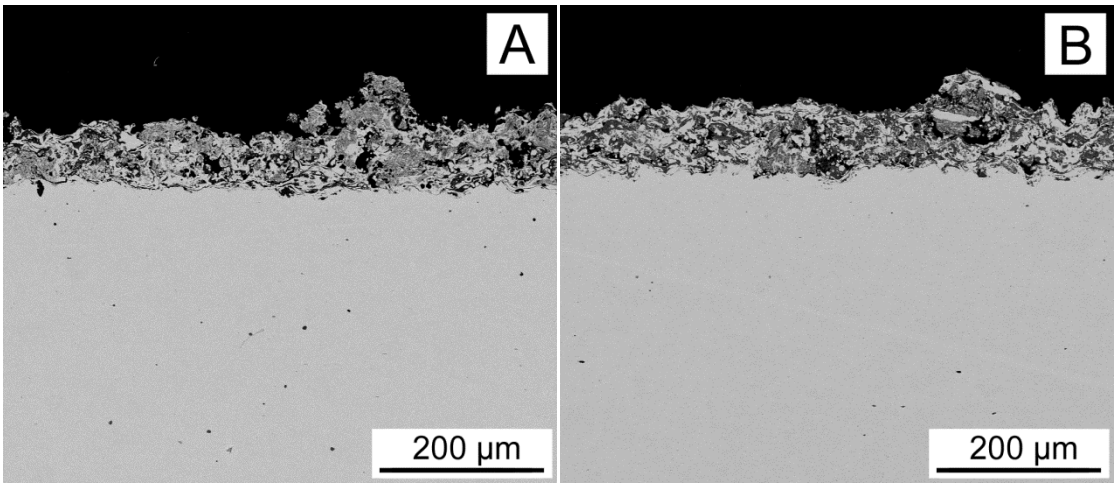

Figure 3.1.15 – SEM pictures of coatings M20-A-1 (a) and M30-A-1 (b).

Sample	Percent porosity
M20-A	6.4
M30-A	4.9

Table 3.1.6 – Percent porosity calculated by using an image analysis software.

The metal matrix, due to the higher temperatures reached by some of the particles using this technique, appears to be partially melted during the spraying process. SEM and EDS analysis performed on the cross section of the coatings revealed some oxidation phenomena that affected the metal matrix, leading to the formation of mixed oxides (fig. 3.1.16, labels 2 and 3).

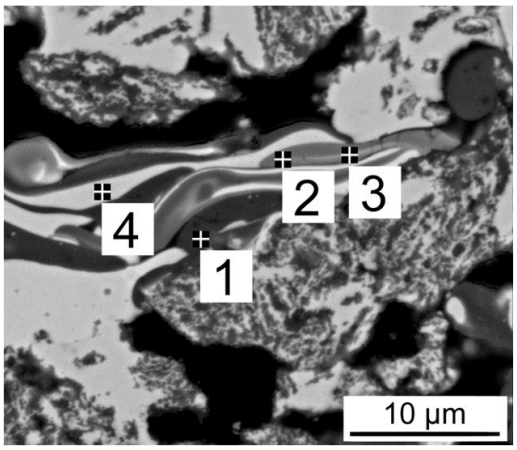

1		
Element	Wt.%	At.%
O K	42.27	57.77
Al K	46.94	38.03
Cr K	3.84	1.62
Co K	4.19	1.55
Ni K	2.75	1.02

2		
Element	Wt.%	At.%
O K	27.96	52.17
Al K	17.1	18.92
Cr K	15.68	9
Co K	22.67	11.48
Ni K	16.59	8.43

3		
Element	Wt.%	At.%
O K	24.12	47.58
Al K	17.1	20
Cr K	12.56	7.63
Co K	24.53	13.14
Ni K	21.69	11.66

4		
Element	Wt.%	At.%
O K	7.8	21.35
Al K	9.26	15.03
Cr K	19.06	16.06
Co K	35.04	26.04
Ni K	28.84	21.52

Figure 3.1.16 – SEM picture and EDS analysis of the coating M20A-1.

Compared to the samples deposited by HVOF, the roughness of the APS coatings is higher (table 3.1.7). This feature seems to be caused by the presence of undeformed particles on the surface of the coating which also contributed to the formation of a large number of pores, as discussed above.

	M20-H-3	M20-A	M20-H-tbc	M20-A-tbc	M30-H-3	M30-A	M30-H-tbc	M30-A-tbc
Ra (µm)	11.10	16.39	10.14	13.56	11.85	16.23	10.37	15.53

Table 3.1.7 – Percent porosity calculated by using an image analysis software.

Generally, relatively higher values of roughness are recommended for bondcoats, because the proper surface roughness could improve the adhesion of the topcoat and positively affect the thermal cycling behavior of TBCs.

However the above mentioned defects within the ODS layer (*e.g.* pores and oxidized zones) might lead to a decrease of the oxidation and high temperature resistance, because oxygen can easily diffuse inward and react with the underlying material, causing a detrimental effect on the whole system.

Thin ODS layers and TBCs

Fig. 3.1.17a,b reveals that the thin ODS-flash layers sprayed by HVOF (labeled M20-H-tbc and M30-H-tbc) were correctly deposited on top of the standard bondcoat.

Compared to the full ODS coatings containing the same amount of aluminum oxide, the porosity is higher because, since this layer has been applied with only two passes of the torch, the peening effect is lower.

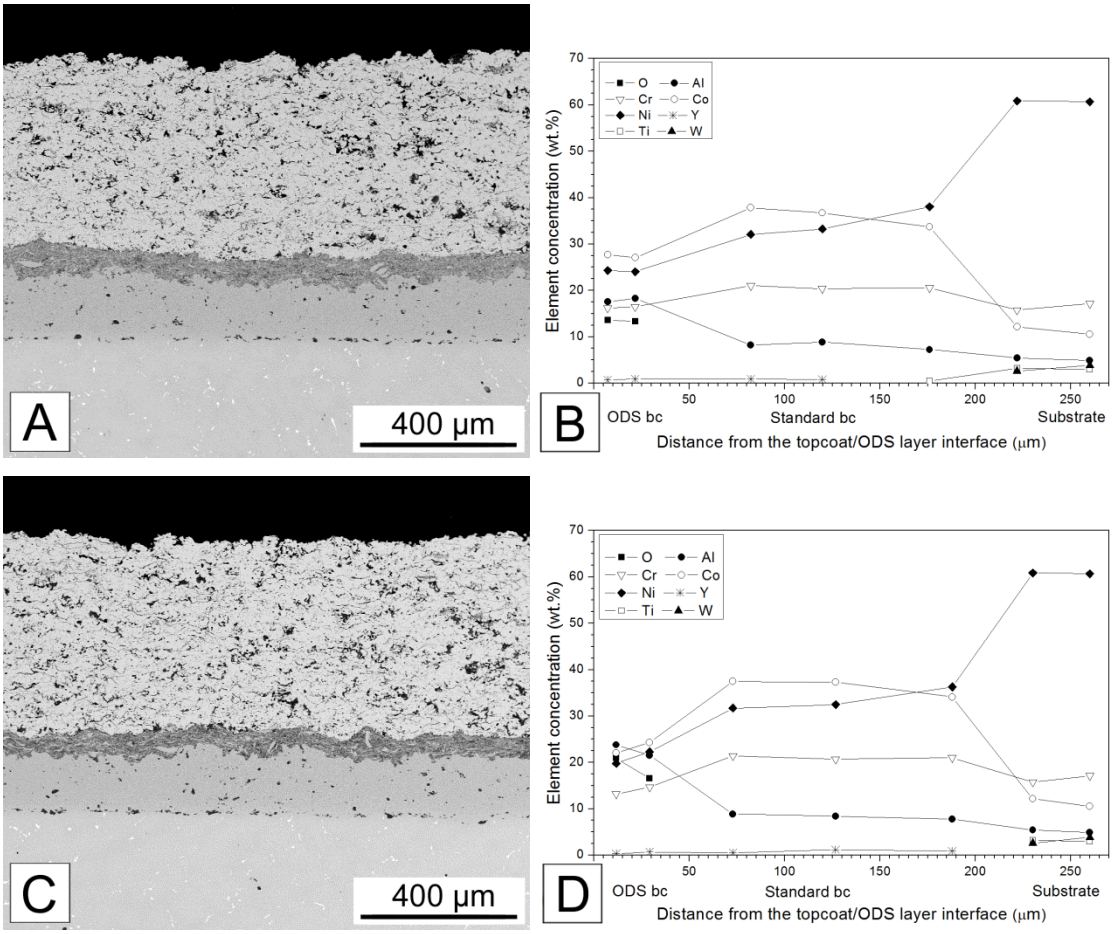

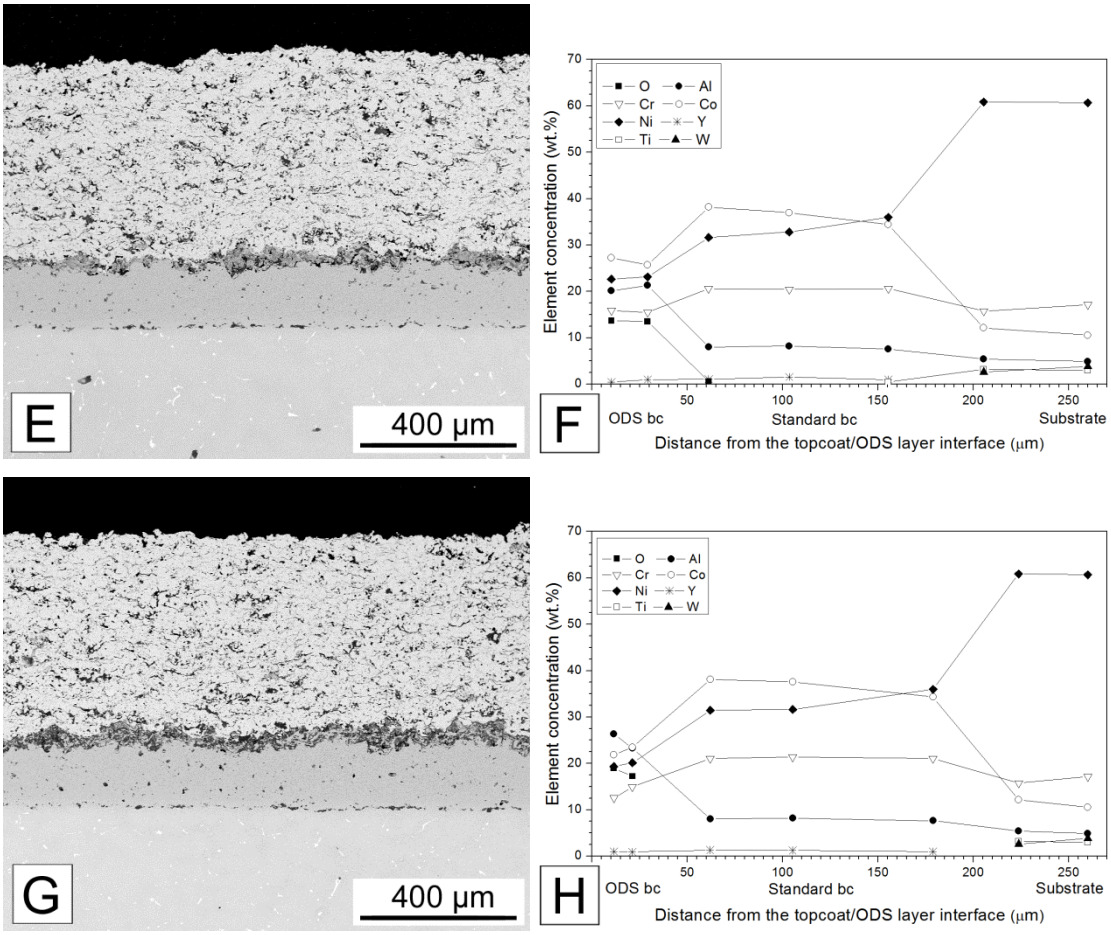

Figure 3.1.17 – SEM pictures and concentration profiles of TBC systems: M20-H-tbc (a,b) and M30-H-tbc (c,d) deposited by HVOF; M20-A-tbc (e,f) and M30-A-tbc (g,h) deposited by APS.

The microstructure the two samples M20-H-tbc and M30-H-tbc is very similar to that of the full ODS coatings previously analyzed.

The thin ODS layers deposited by APS (M20-A-tbc and M30-A-tbc) show higher porosity than the thin coatings deposited by HVOF. Furthermore the thickness of the two layers is not constant and in some region the outer surface of the underlying standard bondcoat is directly in contact with the topcoat (*i.e.* the ODS layers cannot completely cover the whole surface of the samples).

Oxidation test

The results of the oxidation and high-temperature resistance tests are listed in table 3.1.8. The samples based on the ODS-bondcoats deposited by APS (M20-A-tbc and M30-A-tbc) failed after a limited number of cycles (a single cycle consisted of 23 hours at 1100°C and 1 hour cooling). This probably occured because, since the APS ODS-coatings were not perfectly deposited, oxygen diffused inward and reacted with the ODS bondcoat itself.

Sample name	N° of cycles before the first sign of damage	N° of cycles before the complete failure
M20-H-tbc	19	24
M30-H-tbc	22	52
M20-A-tbc	4	15
M30-A-tbc	8	15

Table 3.1.8 – Results of the thermal cycling oxidation test performed on the hybrid TBCs based on a topcoat, a thin ODS layer, a standard bondcoat and an Inconel738 substrate.

The SEM pictures and the EDS analysis results show a severe oxidation within the APS ODS thin layers, which mainly led to the formation of mixed oxides (fig. 3.1.18e-h). The formation of the TGO took place at the interface between the ODS bondcoat and the standard bondcoat, revealing that i) the aluminum amount inside the thin composite coating was not enough to promote the formation of the TGO at the interface with the topcoat and ii) the metal matrix of this layer was not properly connected to allow the outward diffusion of the aluminum from the standard bondcoat to the outer surface of the ODS coating.

The diffusion of Al atoms from the inner region of the bondcoat is necessary to provide the formation of a pure alumina TGO on the surface of the coating, because the Al reacts with oxygen atoms to build up the α-Al_2O_3 scale (mechanism 1, fig. 3.1.19a). The decrease of the Al concentration resulting from the formation of the alumina TGO therefore causes an Al depletion and triggers the formation of a mixed oxide layer above or below the previously grown TGO.

In this specific case, since the APS ODS layer were not perfectly deposited and the initial amount of Al in these layers was not enough to provide the formation of a dense barrier against oxygen diffusion, the result was a severe oxidation of the whole ODS thin coating. Oxygen atoms could easily diffuse across the porous layer, oxidizing the metal matrix and promoting the formation of the TGO at the ODS layer/standard bondcoat interface, where the Al amount was enough to provide the growth of a α-Al_2O_3 scale (mechanism 2, fig. 3.1.19b).

The previous observations are confirmed by the comparison of the element concentration profiles within the TBC systems, before and after the oxidation test (fig. 3.1.17f,h and 3.1.18f,h). The results show a strong increase of the amount of oxygen inside the ODS layer and a relevant diffusion of elements (mainly Ni atoms) from the alloy to the standard bondcoat. The outward diffusion of those elements did not affect the ODS layer, confirming the hypothesis that the metal matrix of the oxide dispersed coating M20-A-tbc and M30-A-tbc

is not properly connected with the standard coating to allow diffusion phenomena and to provide a proper reservoir of scale formers (Al) in the outer layer.

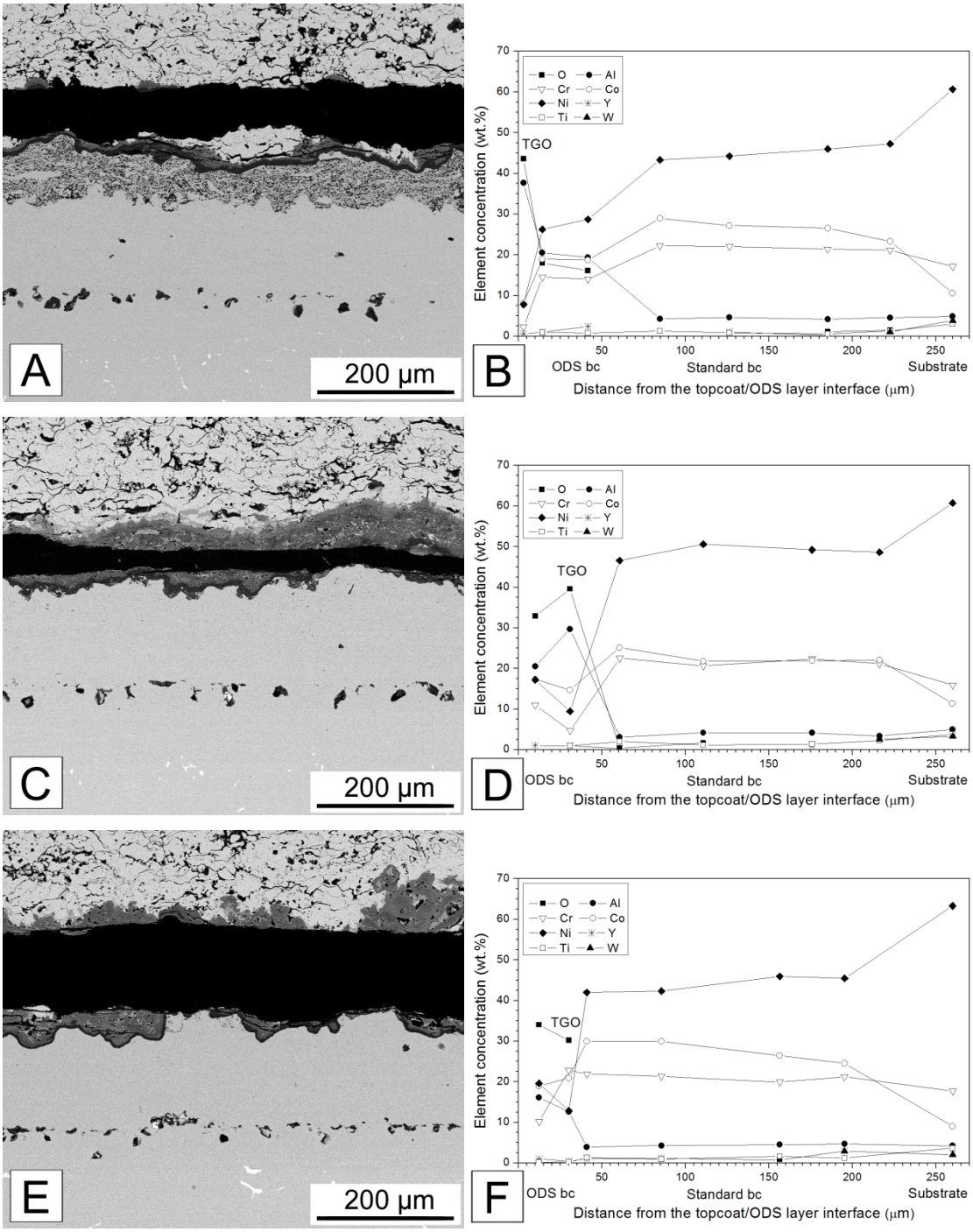

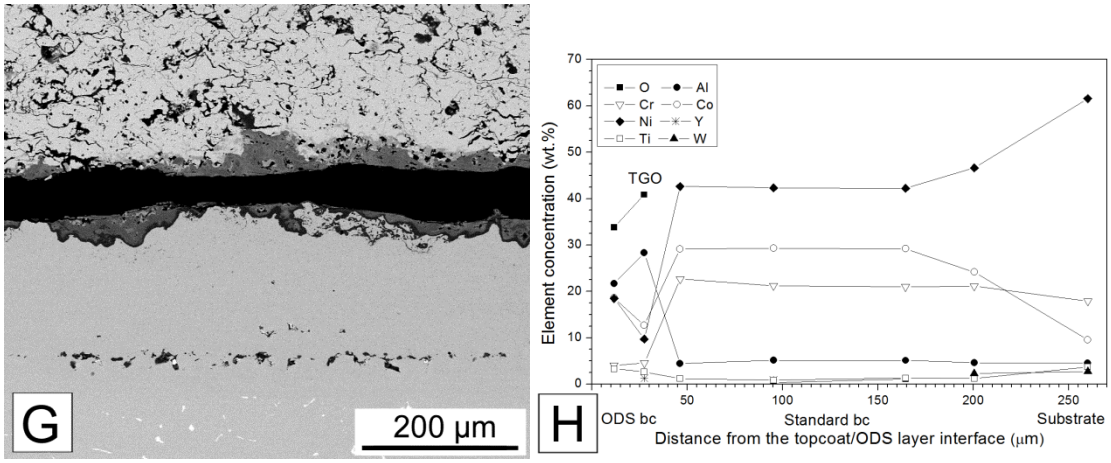

Figure 3.1.18 - SEM pictures and concentration profiles of TBC systems after the oxidation test: M20-H-tbc (a,b) and M30-H-tbc (c,d) deposited by HVOF; M20-A-tbc (e,f) and M30-A-tbc (g,h) deposited by APS.

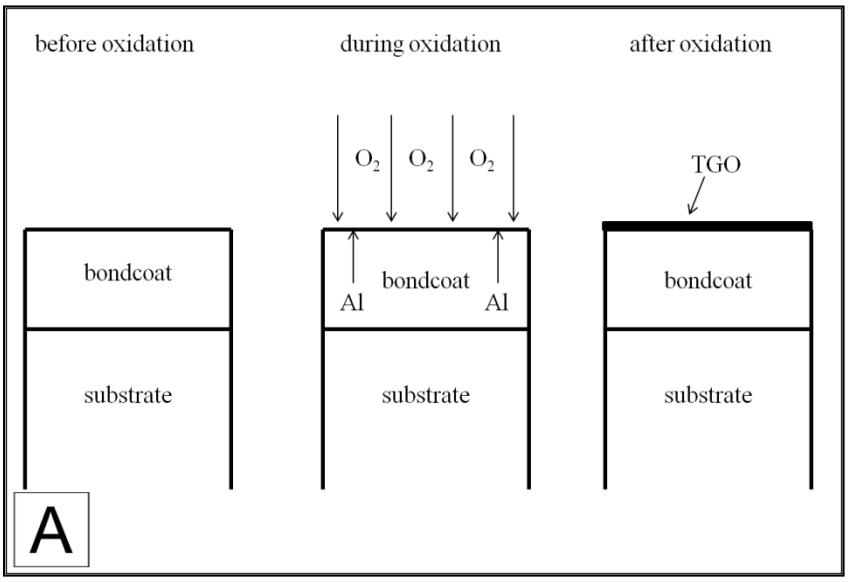

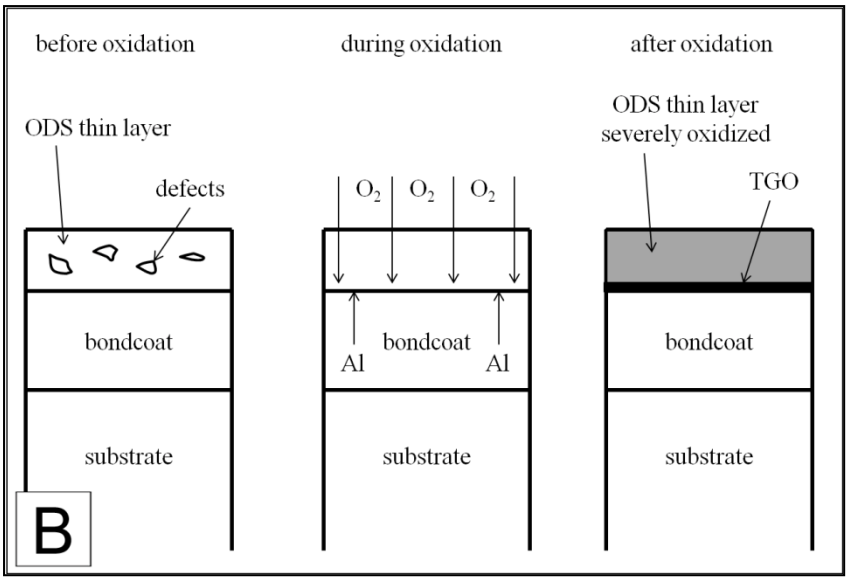

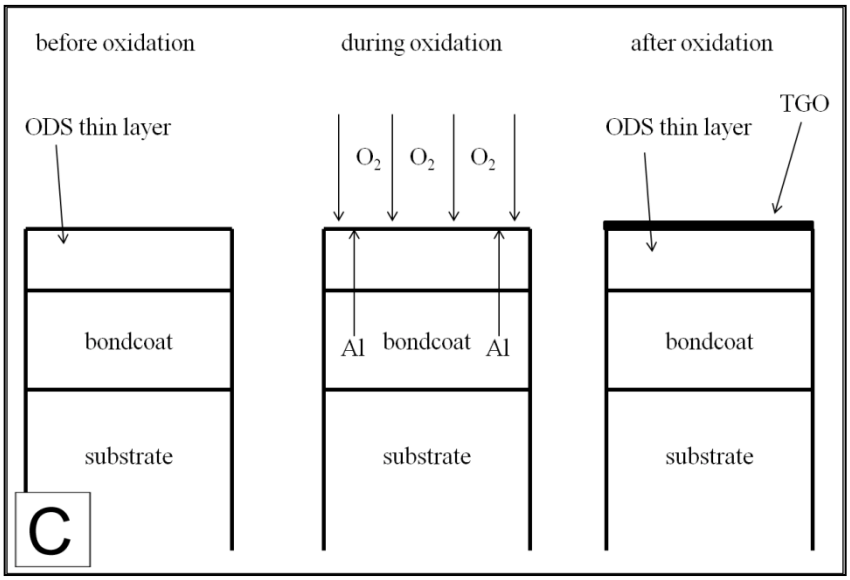

Figure 3.1.19 – Oxidation mechanisms of standard and ODS bondcoats: (a) standard bondcoat; (b) ODS coating featuring high porosity and defects; (c) ODS coatings with low porosity and dense microstructure.

The samples based on the ODS-coating deposited by HVOF (M20-H-tbc and M30-H-tbc) exhibited a better resistance, probably due to their higher thickness and improved microstructure.

The SEM pictures of the M20-H-tbc system shows that the ODS coating microstructure after the oxidation test is very similar to that of the as sprayed sample. Unlike the coatings deposited by APS, the TGO formation took place at the interface between the thin ODS layer and the YPSZ top coat, because the metal matrix was better connected, making the outward diffusion of aluminum from the standard bondcoat easier (mechanism 3, fig. 3.1.19c). Moreover the denser microstructure acted as a barrier against the inward diffusion of oxygen atoms. The concentration profile (fig. 3.1.18b) shows not only the diffusion of aluminum, but also the outward diffusion of nickel and other elements from the bondcoat to the ODS layer, confirming the hypothesis of a better connected structure. The TGO was not only based on α-Al_2O_3: XRD (fig. 3.1.20) and SEM analysis (fig. 3.1.21a) also show a thick layer of mixed oxides, formed due to the Al depletion in the bondcoat during the oxidation test [5,6].

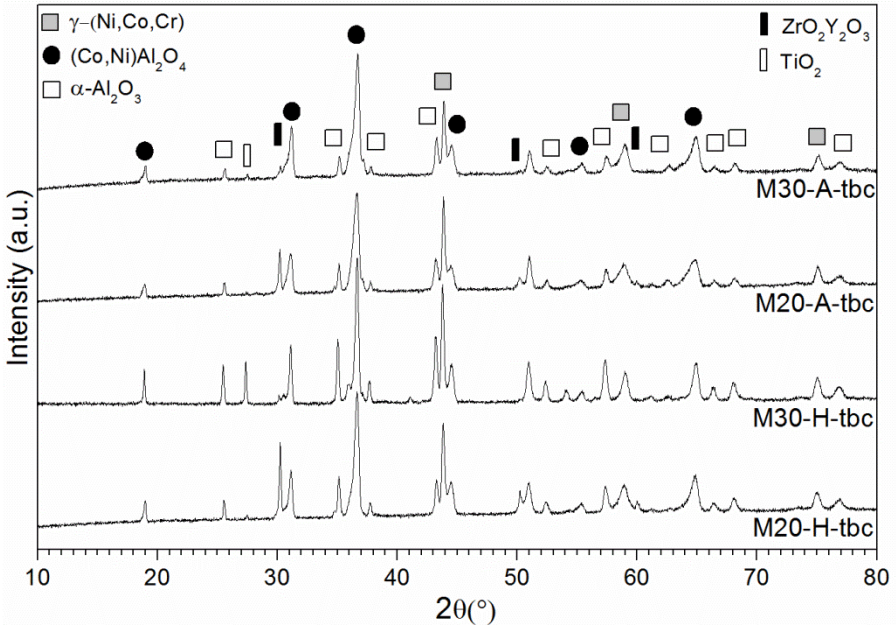

Figure 3.1.20 – XRD patterns of the TBC systems after the oxidation test.

The sample M30-H-tbc shows a different behavior. The SEM picture (fig. 3.1.18c) reveals that the TGO grew at the interface between the two bondcoat layers. Unlike the APS coatings, the metal matrix is still visible and it was not completely oxidized (fig. 3.1.21b). The EDS analysis also shows the complete Al depletion from the CoNiCrAlY matrix of the ODS bondcoat, which brought to the formation of the mixed oxide structure.

The severe oxidation of the ODS layer was caused by several concurring phenomena. First of all, pores and defects led to a relevant inward diffusion of oxygen atoms, which were able to react with the coating matrix. The lack of a stable TGO on the outer surface of the ODS layer, made the diffusion of oxygen even more critical.

The formation of the TGO did not take place at the outer interface because the availability of Al atoms in the ODS layer necessary to form the oxide scale was limited, due to the higher fraction of hard phase within the coating. Furthermore, the high amount of strengthening phase hinders the Al diffusion, which could not diffuse outward, to compensate the Al depletion occurred during the thermal cycling test.

Compared to the coating M20-H-tbc another important difference relies in the failure mechanism: in this case the majority of the ODS layer is still adherent to the YPSZ topcoat and the cracks originated by thermal shocks propagated at the ODS layer/standard bondcoat interface.

This different behavior could be related to the CTE: the sample containing the higher fraction of aluminum oxide (M30-H-tbc) has a CTE more similar to that of the ceramic topcoat.

The lower thermal expansion mismatch reduced the thermal shocks of the system during the cooling phase, increasing the high temperature resistance of the coated component.

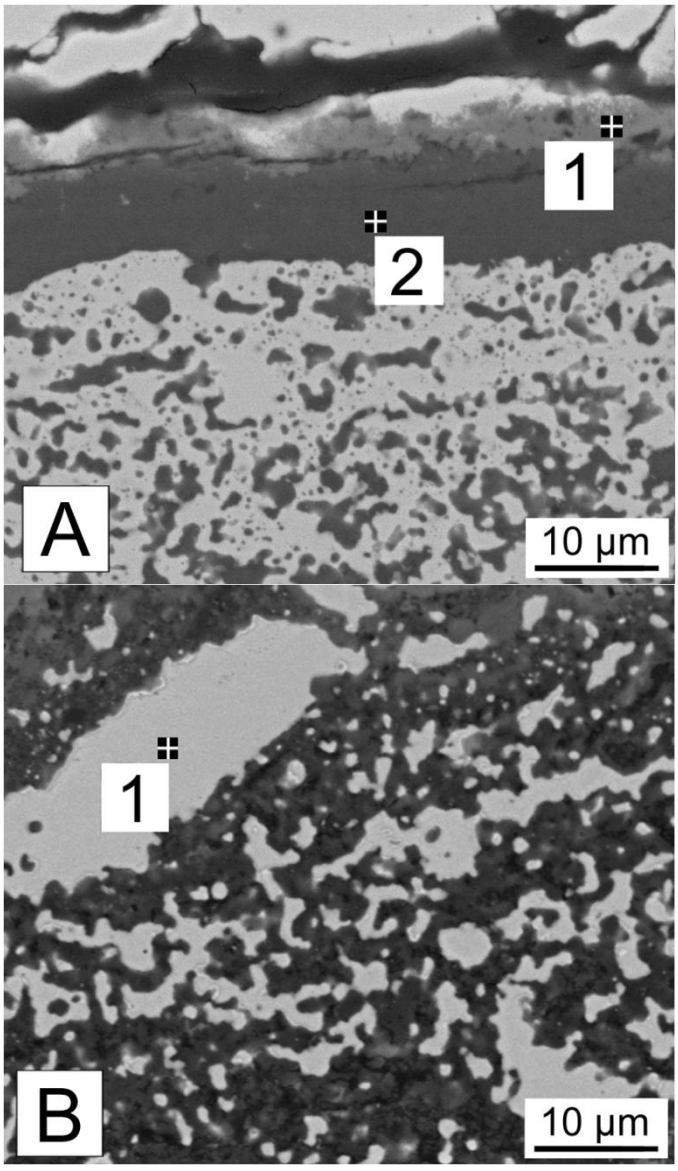

1		
Element	Wt.%	At.%
O	37.33	58.5
Al	29.09	27.04
Cr	2.78	1.34
Co	16.84	7.16
Ni	13.96	5.96

2		
Element	Wt.%	At.%
O	49.48	62.29
Al	50.52	37.71

1		
Element	Wt.%	At.%
Al	0.14	0.31
Cr	3.57	4.01
Co	52.55	51.86
Ni	43.72	43.58
Y	0.36	0.23

Figure 3.1.21 – SEM pictures and EDS analysis on the TGO of the sample M20-H-tbc (a) and on the oxidized layer of the sample M30-H-tbc (b).

Concluding remarks

ODS powders and bondcoats were successfully prepared and the process parameters were examined in details.

Increasing the milling speed and the milling time made the microstructure of the ODS powders more homogenous: the lamellar structure of the metal particles was gradually converted into a composite system based on oxide particles perfectly embedded in the

CoNiCrAlY matrix. The particle size distribution curves become narrower and powders are more suitable for thermal spraying processes.

The evolution of the particles during the milling process also affected the crystallographic structure and the Vickers hardness, due to the continuous refinement of the microstructure and to the plastic deformation occurred on the ODS powders. The particles gradually became more homogenous and the metal matrix experienced severe work hardening. As a consequence, the hardness of the particles increases as a function of the milling time.

A milling speed of 1600 rpm and a milling time of 4 hours, together with a ball-to-powder mass ratio of 10:1, were found to be the best process parameters for the powder blends employed in this investigation.

The coatings deposited using the HVOF spraying gun are denser and exhibit a more homogenous microstructure compared to the coatings deposited by APS. As far as the deposition parameters are concerned, the analysis performed on those ODS coatings showed that there is still some room for improvement.

The deposition process caused a partial recovery of the plastic deformations which affected the metal matrix of the ODS particles during the milling process. As a consequence, the XRD patterns have sharper peaks.

The recovery of the deformations occurred upon milling did not strongly influence the Vickers hardness of the ODS coatings, which is very similar to that of the corresponding ODS powder batches.

The results of the CTE measurements confirmed that the addition of a hard phase having a lower CTE compared to the CoNiCrAlY matrix can effectively reduce the overall CTE of the composite system, mitigating the thermal stresses which arise between the various constituents of a complete thermal barrier coating (comprising a YPSZ top coat as well) upon thermal cycling (especially during the cooling phase). The CTE values are affected by the amount of strengthening phase: higher fractions of alumina led to lower CTEs.

The preliminary high-temperature tests revealed that TBCs based on the ODS layers deposited by APS failed after a limited number of cycles. TBCs having the ODS coating deposited by HVOF exhibit a better high-temperature resistance. Coatings containing different amounts of Al_2O_3 showed different behaviors. The TGO of the bondcoat containing the 20 wt.% of alumina (deposited by HVOF) grew at the interface between the topcoat and the ODS layer.

The thin HVOF ODS coating retained its “as-sprayed” microstructure, probably because the metal matrix of the composite layer was sufficiently interconnected, allowing the outward diffusion of Al and other elements from the standard bondcoat to the ODS layer/topcoat interface. Furthermore the low porosity and the dense microstructure acted as a barrier against the inward diffusion of oxygen atoms.

The TGO of the coating containing the higher fraction of aluminum oxide (deposited by HVOF) grew between the ODS layer and the standard bondcoat, probably because of the higher porosity of the composite coating and of its oxide-rich microstructure, which made the outward diffusion of Al more difficult. The failure mechanism took place mainly at the interface between the TGO and the ODS layer, probably due to the lower mismatch between the CTE of the oxide-rich bondcoat and the ceramic topcoat.

The thermal shock resistance is affected by the CTE: a reduced thermal expansion mismatch results in more durable TBCs. However, the microstructure of the coatings and their capability to provide Al atoms also play an important role in the high-temperature oxidation resistance. Therefore both factors should be taken into account during the design of ODS TBCs.

3.1.2 Coating analysis: Section two

This section concerns the analysis of coatings sprayed using the modified powder batches N10, N20 and N30. The microstructural investigations were performed on the as-sprayed and on the heat treated coatings.

The full ODS bondcoats and the hybrid systems, based on a thin ODS layer deposited above a standard bondcoat, were tested to evaluate their oxidation resistance.

The isothermal oxidation test was carried out at 1100 °C and the selected samples were examined after 10, 100 and 1000 h. The investigation aimed to understand the oxidation mechanisms that occurred on the composite microstructure of those systems.

As sprayed and heat treated coatings

Sample name	Al_2O_3 amount (wt.%)	Information
N10-f	10	Full ODS bondcoat, as sprayed
N10-f-ht	10	Full ODS bondcoat, heat treated
N10-t-ht	10	Thin ODS layer + std bc, heat treated

Table 3.1.9 – Samples containing 10 wt.% of Al_2O_3.

The microstructure of the as-sprayed coating N10-f appears homogenous, even if some regions consisting of pure metal lamellae are still present (fig. 3.1.22a,c). As already stated in the previous section, the heterogeneous regions directly derive from the milled powders.

Despite these few heterogeneous zones, the majority of the coating consists of small oxide particles perfectly surrounded by the metal matrix. No oxidized zones are visible on both the as-sprayed and the heat treated samples.

After the vacuum heat treatment (normally performed on standard bondcoats to promote the formation of the β-phase and to improve the adhesion with the substrate) the coating appears denser: the interdiffusion mechanisms that took place during the heat treatment reduced the porosity of the ODS layer, leaving the microstructure of the coating unaltered (fig. 3.1.22b,d).

The EDS analysis performed on the cross sections of the samples reveals that the Al amount in the heat treated ODS layer is higher than in the as-sprayed sample, probably because this element diffused outward (from the interface towards the centre of the coating) as Ni started to diffuse upwards from the substrate during the vacuum treatment (fig. 3.1.23 and table 3.1.10).

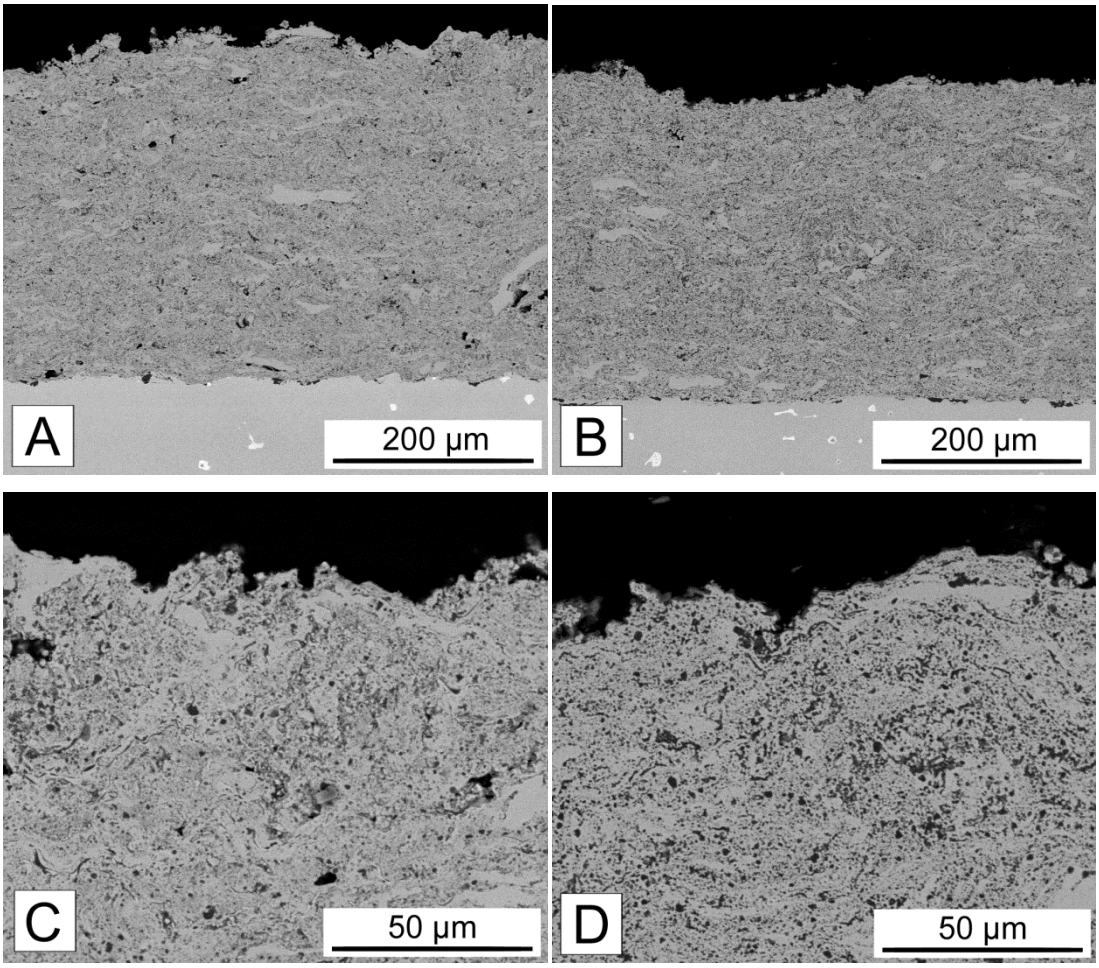

Figure 3.1.22 – SEM pictures of the as-sprayed (a), (c) and heat treated (b), (d) coatings, labeled as N10-f and N10-f-ht respectively.

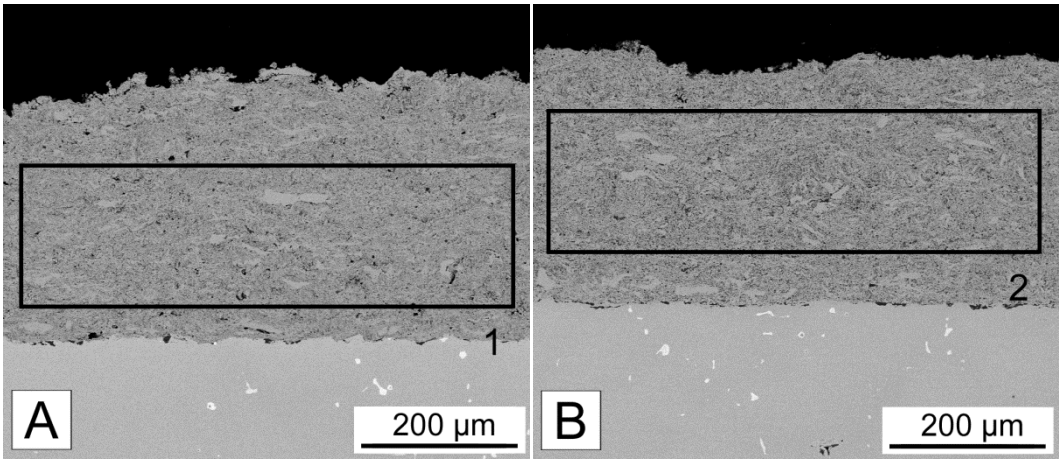

Figure 3.1.23 – SEM micrographs of the coatings N10-f (a) and N10-f-ht (b). The results of the EDS analysis performed on the two regions labeled 1 and 2 are shown in table 3.1.10.

N10-f (1)			N10-f-ht (2)		
Element	**Wt.%**	**At.%**	**Element**	**Wt.%**	**At.%**
O	12.87	31.04	**O**	11.76	28.56
Al	13.85	19.8	**Al**	14.94	21.51
Cr	16.61	12.32	**Cr**	18.34	13.71
Co	30.14	19.74	**Co**	29.23	19.27
Ni	25	16.43	**Ni**	25.35	16.78
Y	1.53	0.66	**Y**	0.39	0.17

Table 3.1.10 – Chemical composition of the full ODS coating: as sprayed (N10-f) and after the vacuum heat treatment (N10-f-ht).

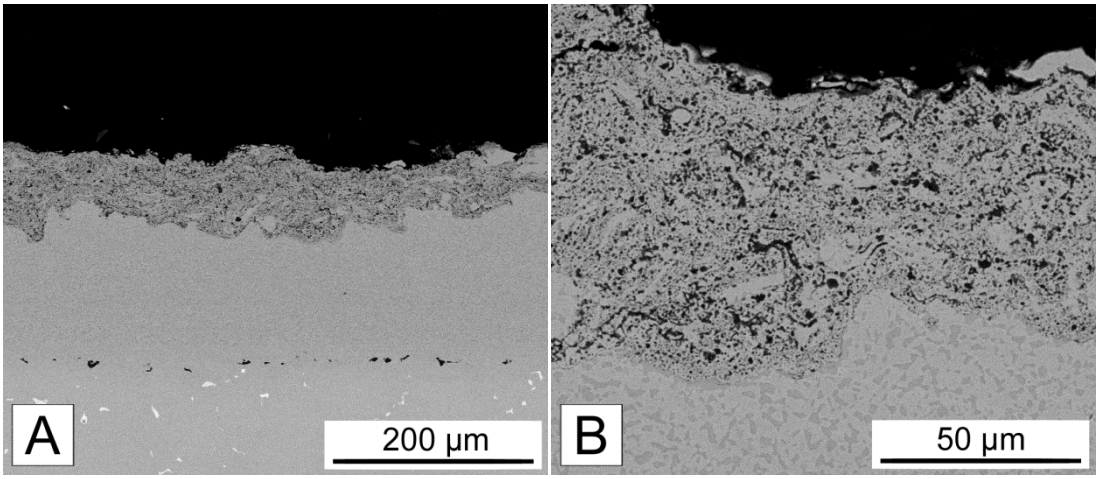

Figure 3.1.24 – SEM pictures of the coating N10-t-ht.

The thin ODS layer was successfully deposited on the whole surface of the standard CoNiCrAlY bondcoat (fig. 3.1.24). Despite this thin layer was sprayed with only few passes of the torch, the microstructure appears dense and very similar to that of the full ODS bondcoat N10-f-ht. Fig. 3.1.25a and b reveal the presence of the β-phase on the standard bondcoat and on the metal matrix of the ODS layer, correctly formed after the diffusion treatment.

The formation of the β-phase is crucial for the lifetime of TBCs, because it acts as a reservoir of aluminum, necessary for the formation of a dense alumina scale. Despite the strengthening media, the metal matrix of the bondcoat still has a sufficient amount of Al to form the β-phase.

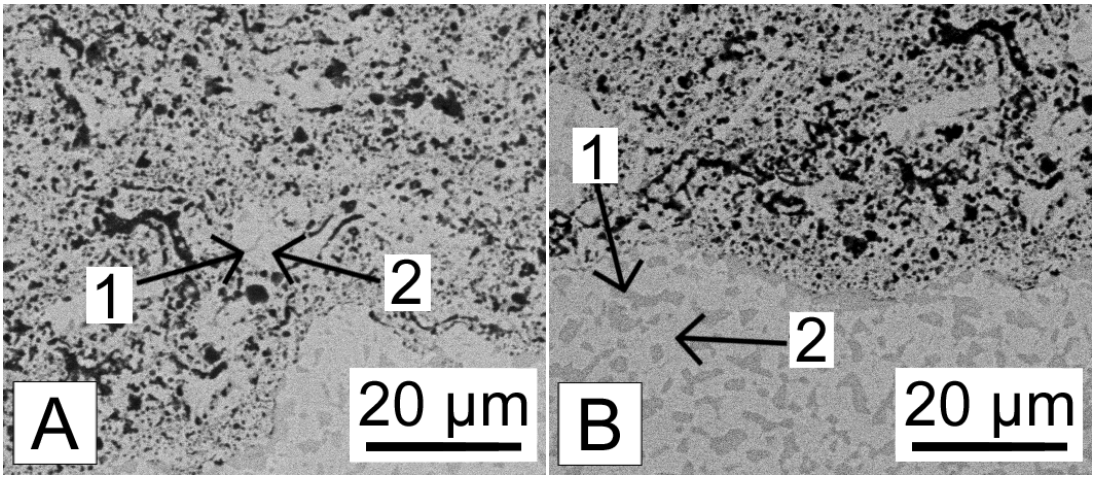

Figure 3.1.25 - β-phase regions (arrow 1) surrounded by the γ-phase matrix (arrow 2) on both the ODS layer (a) and the standard bondcoat (b) (sample N20-t-ht).

Sample name	Al_2O_3 amount (wt.%)	Information
N20-f	20	Full ODS bondcoat, as sprayed
N20-f-ht	20	Full ODS bondcoat, heat treated
N20-t-ht	20	Thin ODS layer + std bc, heat treated

Table 3.1.11 – Samples containing 20 wt.% of Al_2O_3

Compared to the coating N10-f, the sample N20-f features a more homogeneous microstructure, with lower amounts of purely metallic lamellae and of porosity (fig. 3.1.26a,c), probably because the feedstock powder N20 had less defects and pores than the powder N10. After the vacuum heat treatment the coating became even denser (fig. 3.1.26b,d).

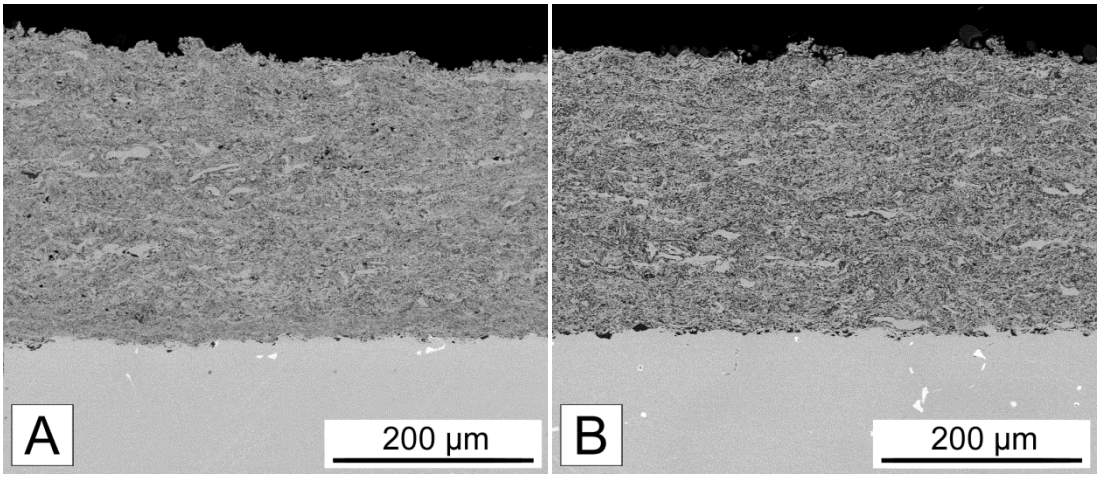

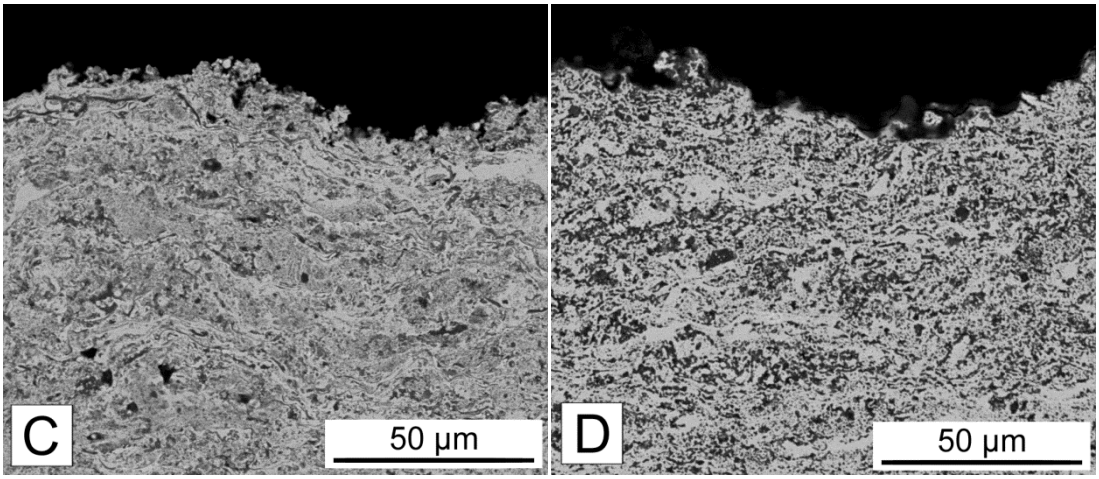

Figure 3.1.26 – SEM pictures of the as-sprayed (a), (c) and heat treated (b), (d) coatings, labeled as N20-f and N20-f-ht respectively.

Series 1	Percent porosity	Series 2	Percent porosity
/	/	N10-f	0.3
M20-H-1	1.1	N20-f	0.1
M30-H-1	2.2	N30-f	0.3

Table 3.1.12 – Percent porosity of the ODS coatings M20-H-1, M30-H-1, N10-f, N20-f, N30-f.

The comparison between the samples M20-H-1 (fig. 3.1.10a) and N20-f (fig. 3.1.26a) clearly shows that the coating belonging to the second series features an improved microstructure and a lower porosity (table 3.1.12).

The different milling conditions permitted to obtain more homogenous feedstock powders and, as a consequence, the porosity of the resulting coating is reduced and the pure metal lamellae inside the ODS layer are barely visible.

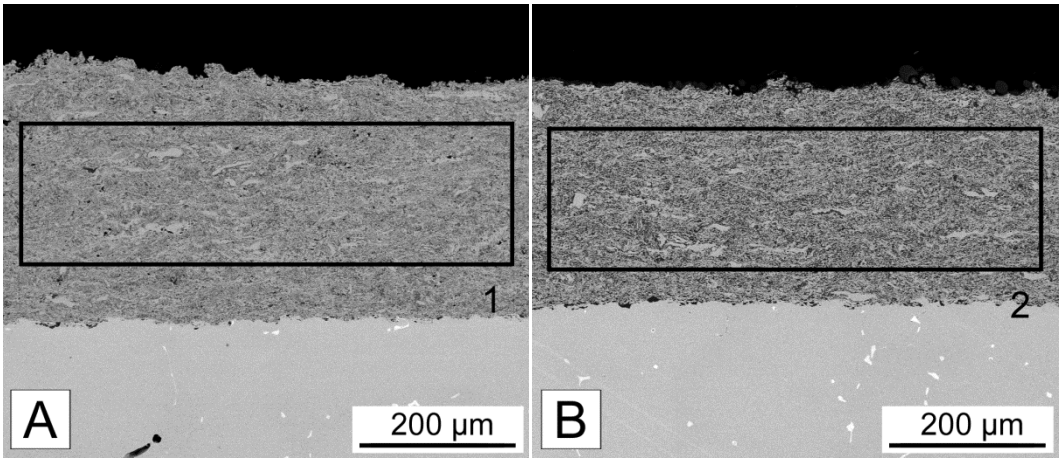

Figure 3.1.27 – SEM micrographs of the coatings N20-f (a) and N20-f-ht (b). The results of the EDS analysis performed on the two regions labeled 1 and 2 are shown in table 3.1.13.

N20-f (1)			N20-f-ht (2)		
Element	**Wt.%**	**At.%**	**Element**	**Wt.%**	**At.%**
O	16.97	37.42	**O**	15.84	34.94
Al	16.32	21.35	**Al**	18.98	24.83
Cr	16.02	10.87	**Cr**	14.77	10.02
Co	27.11	16.23	**Co**	26.83	16.07
Ni	23.37	14.05	**Ni**	23.37	14.05
Y	0.2	0.08	**Y**	0.22	0.09

Table 3.1.13 – Chemical composition of the full ODS coating: as sprayed (N20-f) and after the vacuum heat treatment (N20-f-ht).

As previously noticed, the aluminum amount on the heat treated coating is higher than the concentration of this element in the as sprayed sample, probably due to interdiffusion phenomena which affected the coating during the treatment (table 3.1.13 and fig. 3.1.27).

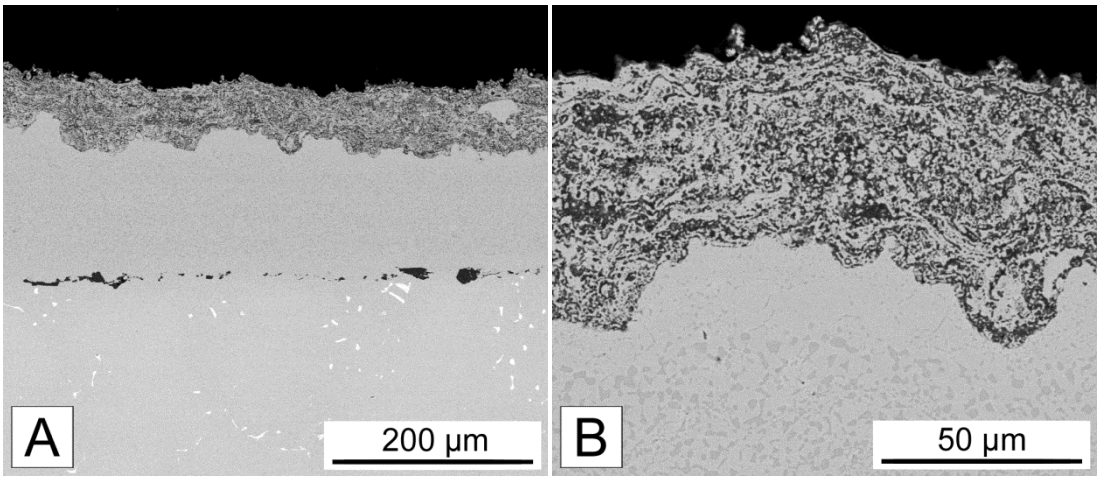

Figure 3.1.28 – SEM pictures of the coating N20-t-ht.

The thin ODS layer was correctly deposited on the whole surface of the standard bondcoat and appears dense (fig. 3.1.28). The vacuum treatment brought to an Al depletion that partially affected the outer region of the standard CoNiCrAlY coating (fig. 3.1.29), probably because, due to the higher amount of strengthening media, Al interdiffusion between different metallic regions inside the metal matrix of the ODS layer was more difficult than diffusion of Al from the underlying pure MCrAlY bond coat directly into neighboring metallic areas of the ODS layer. Therefore, Al atoms diffused from the standard bondcoat towards the thin layer.

The Al depleted zones demonstrate that the metal matrix of the composite layer is sufficiently connected to create a path across the metal phase, which allows the diffusion of different atom species (*e.g.* Al) from the inner region to the outer layer.

The previous investigation concerning the thermal cycling resistance of the hybrid TBCs (reported in *section one*) demonstrated that a dense and connected microstructure is necessary to promote the formation of a protective TGO on the surface of the ODS layer.

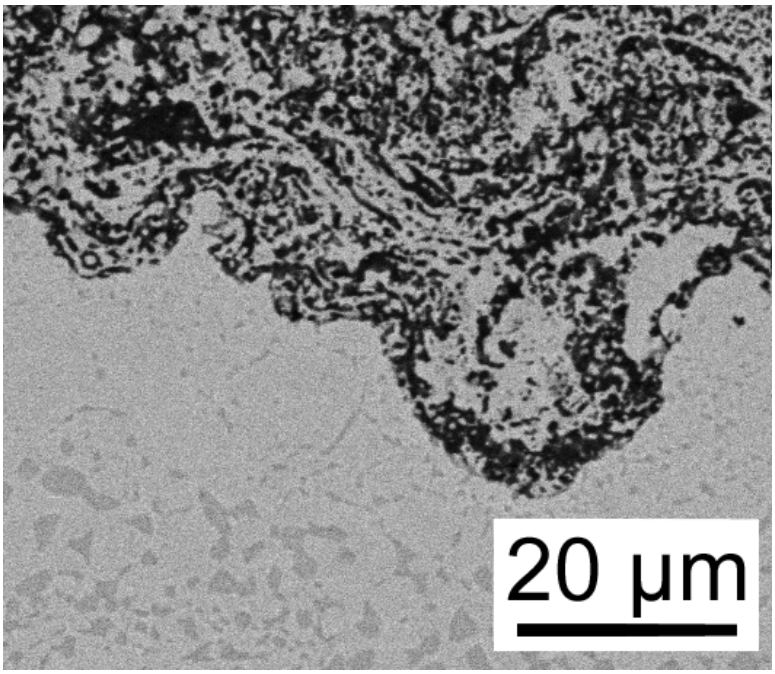

Figure 3.1.29 - β-phase depletion on the external region of the standard bondcoat, at the interface with the ODS layer (sample N20-t-ht).

The β-phase zones in the ODS layer are barely visible (fig. 3.1.29), probably because of the refined microstructure of the metal matrix, which did not allow the formation of large β-phase regions during the vacuum treatment.

Sample name	**Al_2O_3 amount (wt.%)**	**Information**
N30-f	30	Full ODS bondcoat, as sprayed
N30-f-ht	30	Full ODS bondcoat, heat treated
N30-t-ht	30	Thin ODS layer + std bc, heat treated

Table 3.1.14 – Samples containing 30 wt.% of Al_2O_3

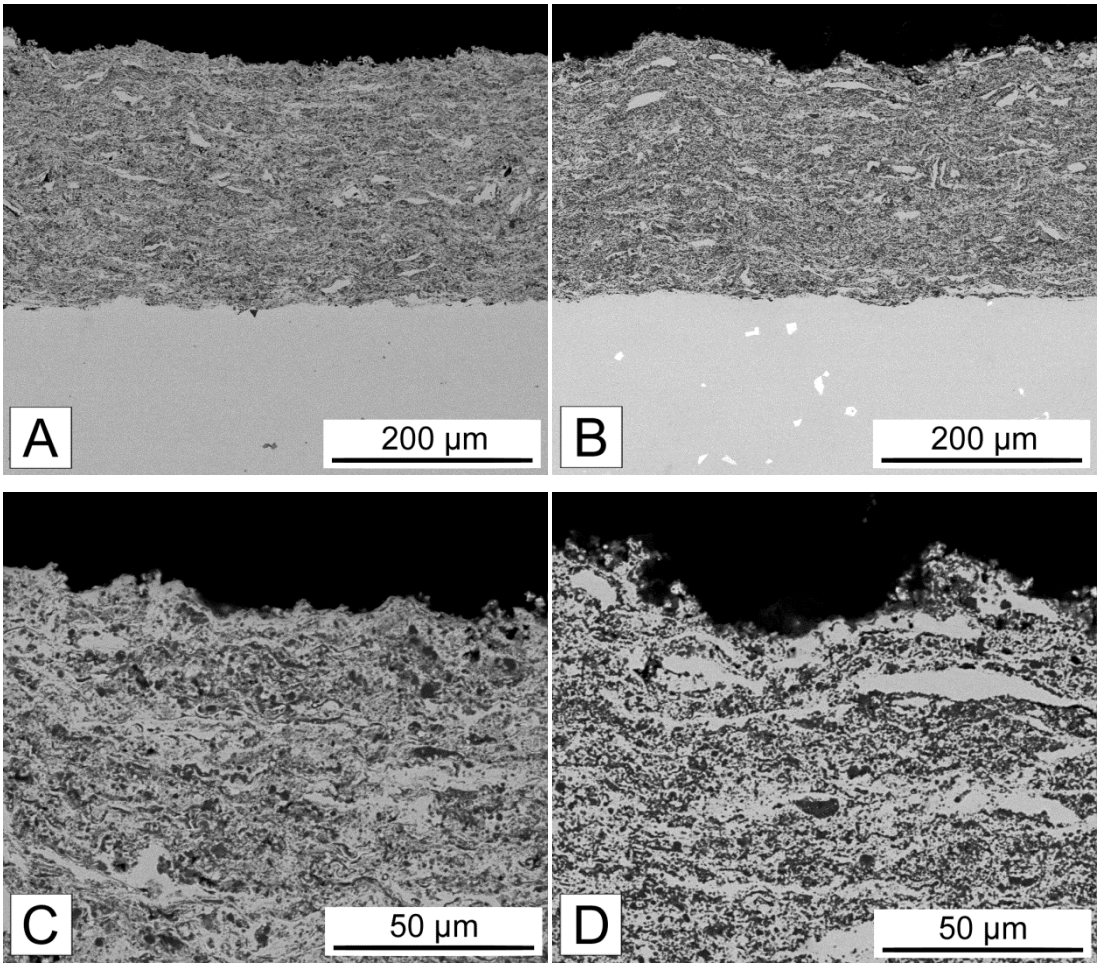

Figure 3.1.30 – SEM pictures of the as-sprayed (a), (c) and heat treated (b), (d) coatings, labeled as N30-f and N30-f-ht respectively.

The feedstock powder N30 permitted to obtain a more homogenous ODS coating than the coating M30-H-1 (*section one*, fig. 3.1.10d). The upgrade of the milling process led to a decrease of the pure metal lamellae within the ODS particles, improving the overall quality of the bondcoat (fig. 3.1.30a,c).

Furthermore the coating N30-f is denser and thicker. As previously stated, after the diffusion heat treatment, the porosity is even reduced (fig. 3.1.30b,d) and the Al amount inside the layer returns similar to that originally found in the milled powders (table 3.1.15).

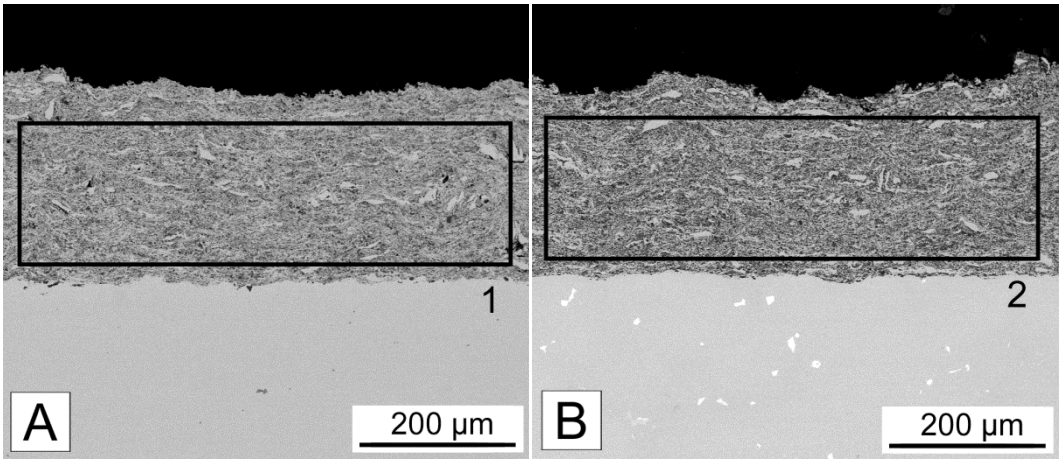

Figure 3.1.31 – SEM micrographs of the coatings N30-f and N30-f-ht. The results of the EDS analysis performed on the two regions labeled 1 and 2 are shown in table 3.1.15.

N30-f			N30-f-ht		
Element	**Wt.%**	**At.%**	**Element**	**Wt.%**	**At.%**
O	21.37	43.19	**O**	19.94	40.23
Al	19.39	23.23	**Al**	23.1	27.63
Cr	14.15	8.8	**Cr**	13.72	8.52
Co	24.17	13.26	**Co**	23.59	12.92
Ni	20.91	11.51	**Ni**	19.13	10.51
Y			**Y**	0.52	0.19

Table 3.1.15 – Chemical composition of the full ODS coating: as sprayed (N30-f) and after the vacuum heat treatment (N30-f-ht)

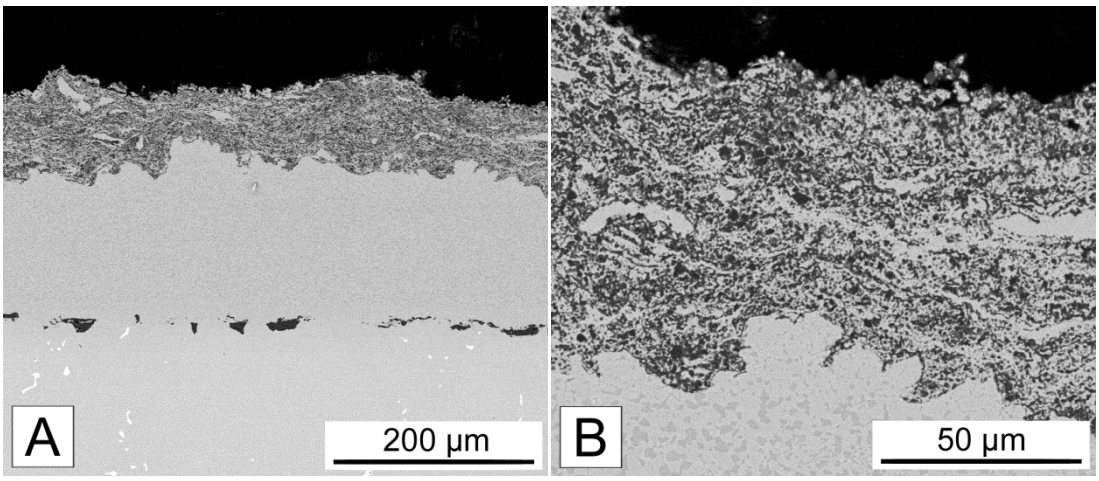

Figure 3.1.32 – SEM pictures of the coating N30-t-ht.

The comments made for the coating N20-t-ht can also be applied to the thin ODS layer containing a higher fraction of Al_2O_3 (labeled N30-t-ht, fig. 3.1.32). The thin Al depleted zone on top of the underlying MCrAlY layer is still present, confirming that higher fractions of strengthening media result in a decrease of the Al content within the ODS layer (fig. 3.1.33).

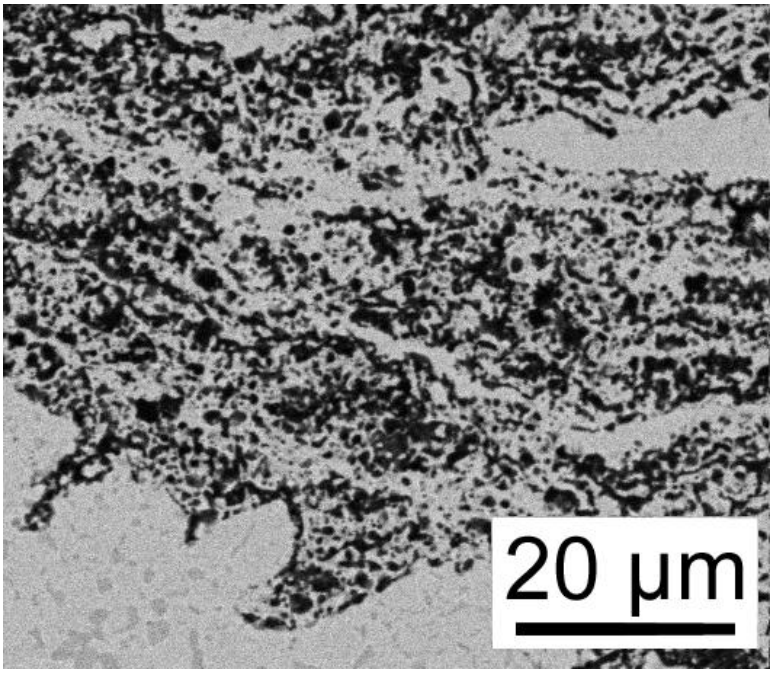

Figure 3.1.33 – High magnification SEM picture of the coating N30-t-ht.

XRD analysis

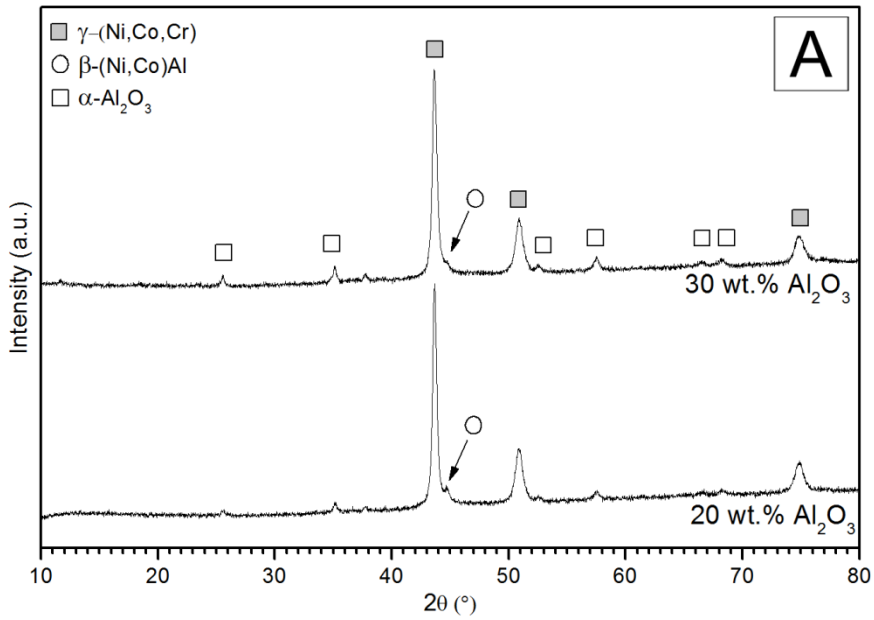

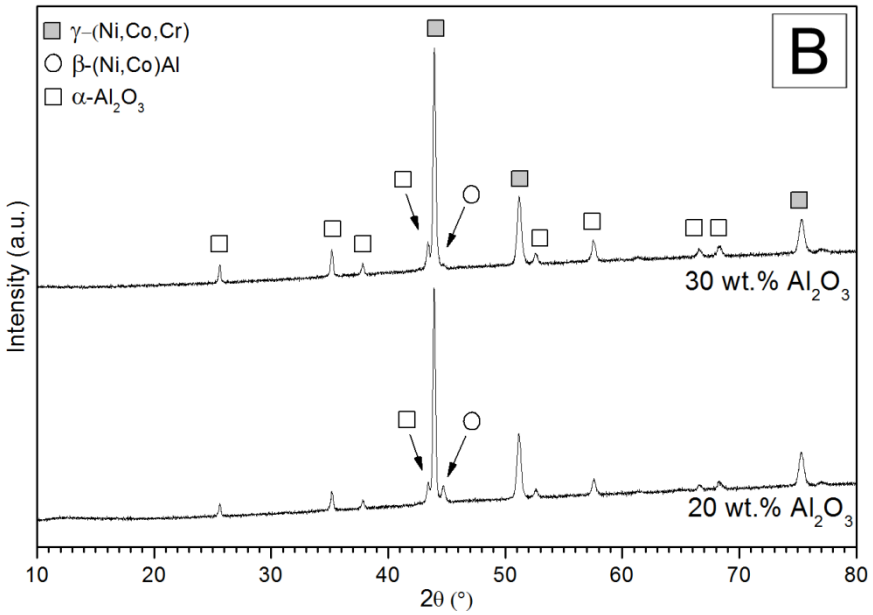

Figure 3.1.34 – XRD patterns of the as sprayed (a) and heat treated ODS coatings (b).

The XRD analysis performed on the as sprayed and on the heat treated coatings containing 20 and 30 wt.% of aluminum oxide (fig. 3.1.34a,b) revealed differences in the XRD patters before and after the vacuum treatment.

The width of the diffraction peaks after the heat treatment appears narrower, indicating larger and/or less defective crystalline grains. The vacuum thermal treatment caused an important recovery of the plastic deformation and induced a recrystallization of the coating structure. Peaks therefore became sharper and some less intense peaks are now visible.

The main difference between the XRD patterns of coatings containing 20 and 30 wt.% of alumina relies in the intensity of the β-phase peak (located at 2θ=44.7-44.8°), which is more visible in the sample having the lower amount of hard phase.

The lower intensity of the β-phase peak in coatings containing higher concentrations of oxides is probably caused by the reduced fraction of CoNiCrAlY metal matrix. As a consequence, the overall amount of β-phase formed in the coating during the vacuum treatment is lower and the resulting peaks in the XRD patterns are less visible.

Roughness

The roughness and the 3D pictures of the ODS coatings were acquired by the Cyberscan optical profilometer. The values were compared to that of the standard bondcoat used as a term of comparison during the oxidation test and as a substrate for the thin ODS layer as well.

The 3D pictures were acquired scanning a surface of 1x1mm and 10x10mm. Hereafter only the picture concerning the 1x1 mm area are reported.

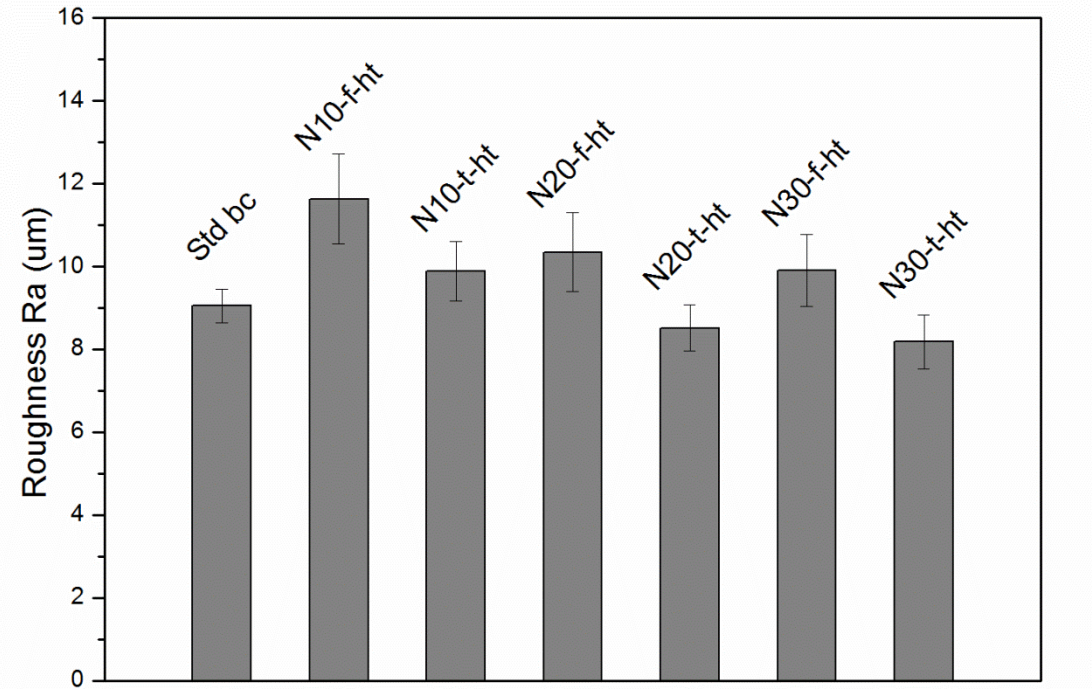

Figure 3.1.35 – Roughness values (Ra) of the ODS and standard bondcoats.

The plot in figure 3.1.35, containing the roughness of the ODS bondcoats, shows a strong correlation between the amount of Al_2O_3 within the coating and the values of Ra. The concentration of strengthening media, as demonstrated in *section one*, affected the size of the ODS particles at the end of the milling process: powders containing 10 wt.% of alumina are coarser than powders containing higher fractions of oxides. As a consequence, the deposition of finer particles resulted in a smoother coating surface.

Furthermore, the roughness of the full ODS bondcoats is higher than the roughness of the standard bondcoat used as a competitor.

The Ra values of the thin ODS layers are affected by the Al_2O_3 amount within the coating as well, but all the values are lower than that of their respective full ODS counterpart.

Except for the sample N10-t-ht, the other two thin ODS layers have lower surface roughness than the standard bondcoat used as a substrate, probably because the particles deposited during the first passes of the torch mainly cover the valley of the pure CoNiCrAlY surface, flattening the texture.

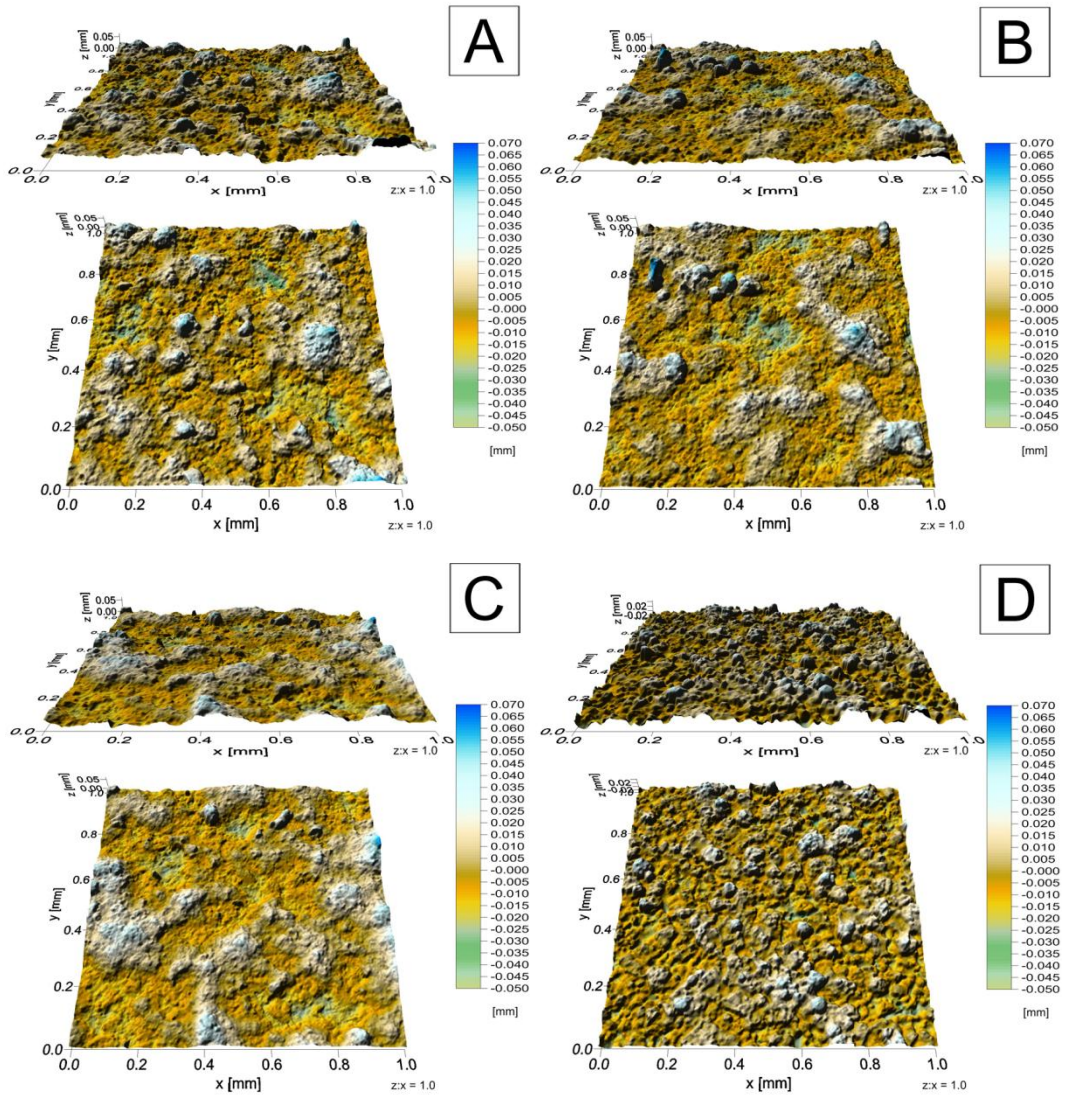

Figure 3.1.36 – 3D images showing the surface morphology: (a) N10-f-ht, (b) N20-f-ht, (c) N30-f-ht, (d) Std-bc.

The 3D pictures of the surfaces (fig. 3.1.36) and the plots containing the Ra values as a function of the cut-off wavelength λc (μm) (plots in fig. 3.1.37) give more information concerning the surface textures of the ODS systems.

Even if the Ra values of the ODS layers calculated at λc=2500 μm are higher than the value of the standard bondcoat, the 3D images show that the texture of the latter is more regular, whereas the ODS layers have higher peaks surrounded by smoother regions. These assumptions are confirmed by the Ra values plotted as a function of λc, which give information about the micro-roughness. Under a certain value of λc (λc~300 c/μm), the roughness of the ODS layers drops consistently: as the cut-off wavelength becomes comparable to the lateral size of the large peaks, indeed the latter are filtered away from the roughness profile.

Roughness and surface texture might affect the adhesion of the topcoat to the bondcoat surface and might influence the lifetime of TBCs, therefore more tests will be necessary to completely evaluate their effect on the high-temperature resistance of those ODS layers.

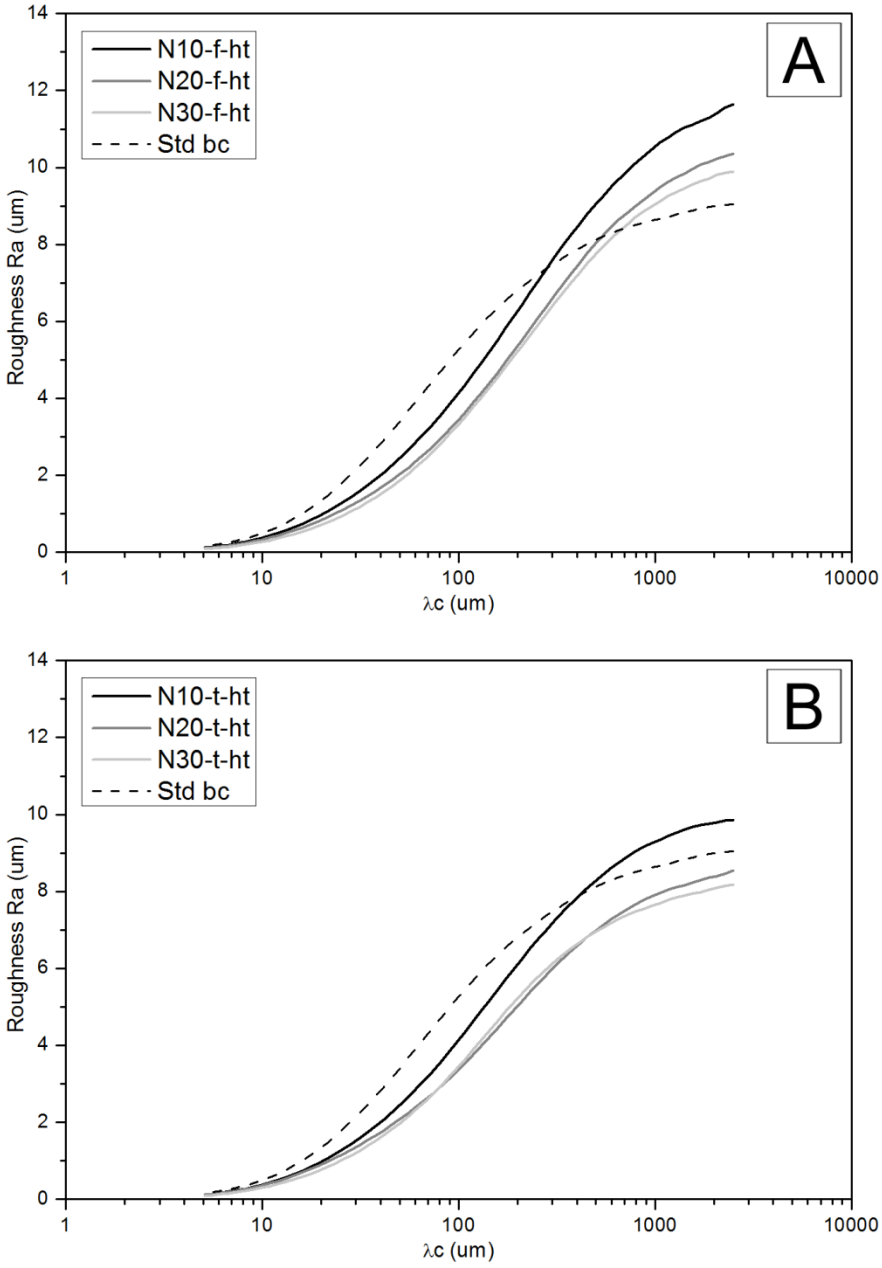

Figure 3.1.37 – Roughness values as a function of λc: (a) full ODS coatings, (b) thin ODS layers. The standard bondcoat was used as a competitor.

Hardness

The hardness values are influenced by the amount of strengthening phase. Figure 3.1.38 shows that coatings having higher contents of Al_2O_3 feature higher values of Vickers

hardness. The standard deviation is consistent because the nano-indentations were influenced by the composition of the coatings. Therefore, for each composition, the result is an average of indentations performed on the metal regions and indentations performed on zones with a higher amount of oxide phase.

Hardness is also influenced by the vacuum thermal treatment, due to the recovery of the work-hardening that affected the metal matrix during the milling process. As previously stated in *chapter 1* and consistent with [1,2], the ball-powder collisions that took place during the alloying process resulted in a severe work-hardening of the metal matrix which was not completely removed during the deposition of the ODS coatings.

The heat treatment, performed at temperatures above 1000 °C, induced recovery of the plastic deformation, recrystallization and strain relaxation, as confirmed by the XRD analysis results as well.

As a consequence the Vickers hardness of the heat treated coatings is lower than that of the as-sprayed layers containing the same amount of oxide particles.

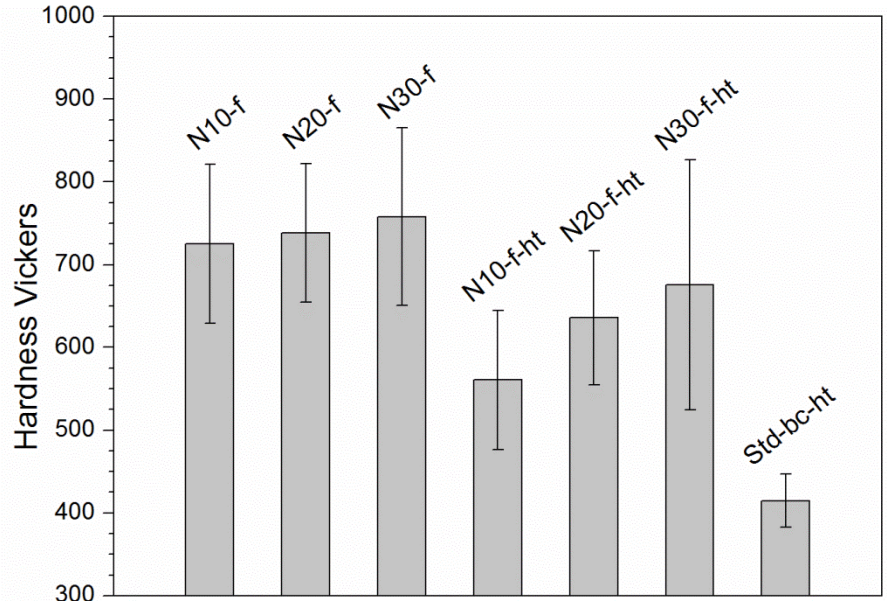

Figure 3.1.38 – Hardness values measured on the cross sections of the coatings.

The comparison between the coatings produced using the powder batches M20, M30 (fig. 3.1.13) and the coatings containing the powder batches N20 and N30 (fig. 3.1.38) shows that the improved microstructure and the higher density of the second series of samples (*i.e.* N20-f and N30-f) led to an increase of the hardness values.

Isothermal oxidation test

Before showing the results of the oxidation test performed on the ODS bondcoats, the isothermal oxidation behavior of a standard CoNiCrAlY bondcoat is explained to point out to the transformation occurring in the microstructure of a standard coating. The information is then used to better evaluate the mechanisms involved in the oxidation of full and thin ODS layers.

Sample name	Al_2O_3 amount (wt.%)	Information
Std-bc-ht	no Al_2O_3	Standard bondcoat, heat treated
Std-bc-10h	no Al_2O_3	Standard bondcoat, after 10 h at 1100 °C
Std-bc-100h	no Al_2O_3	Standard bondcoat, after 100 h at 1100 °C

Table 3.1.16 – Samples based on the standard CoNiCrAlY composition.

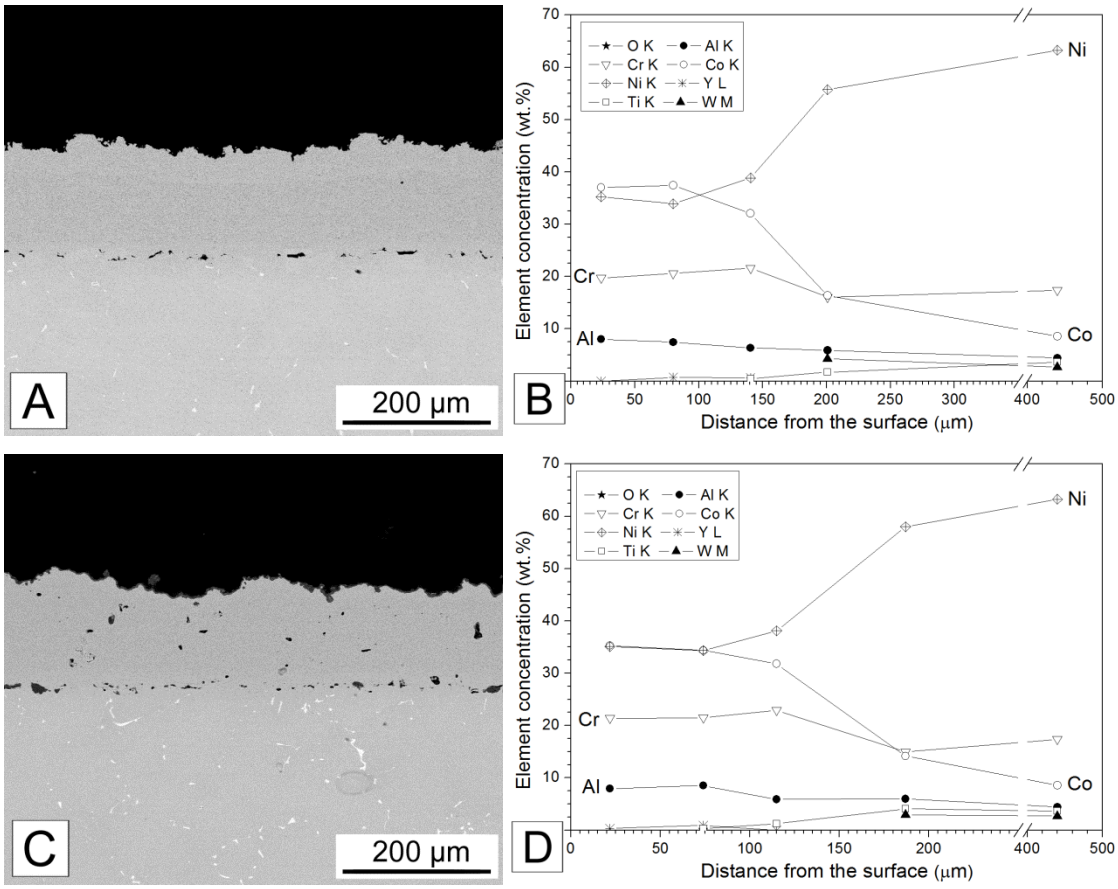

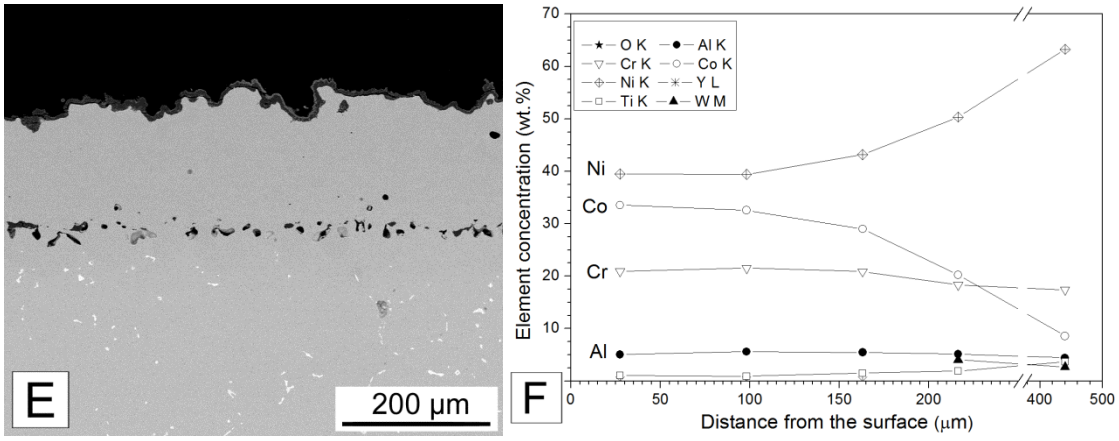

Figure 3.1.39 – SEM picture and chemical composition of the standard bondcoat after the vacuum heat treatment (a), 10 hours at 1100 °C (b), 100 h at 1100 °C (c).

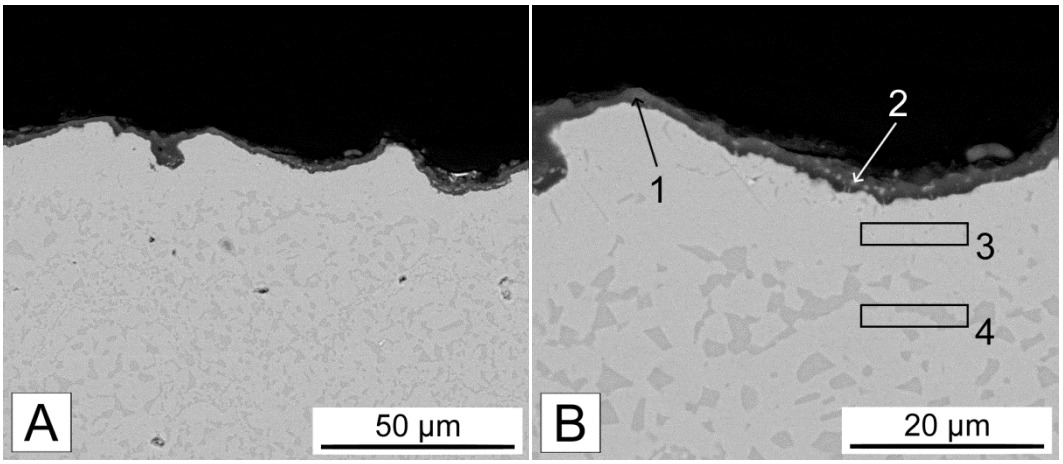

Figure 3.1.40 – SEM pictures of the standard bondcoat after 10 hours at 1100 °C. The EDS analysis results are given in table 3.1.17.

	1			2	
Element	**Weight%**	**Atomic%**	**Element**	**Weight%**	**Atomic%**
O	62.43	73.92	**O**	51.19	70.63
Al	36.71	25.77	**Al**	29.22	23.9
Cr	0.86	0.31	**Cr**	1.51	0.64
Co			**Co**	1.02	0.38
Ni			**Ni**	1.63	0.61
Y			**Y**	15.43	3.83
	3			**4**	
Element	**Weight%**	**Atomic%**	**Element**	**Weight%**	**Atomic%**
Al	5.42	10.85	**Al**	7.08	13.87
Cr	22.97	23.87	**Cr**	21.67	22.03
Co	39.26	36	**Co**	37.93	34.02
Ni	30.4	27.98	**Ni**	32.9	29.62
Y	1.74	1.06	**Y**		
Ti	0.2	0.23	**Ti**	0.41	0.46

Table 3.1.17 – EDS results of fig. 3.1.40.

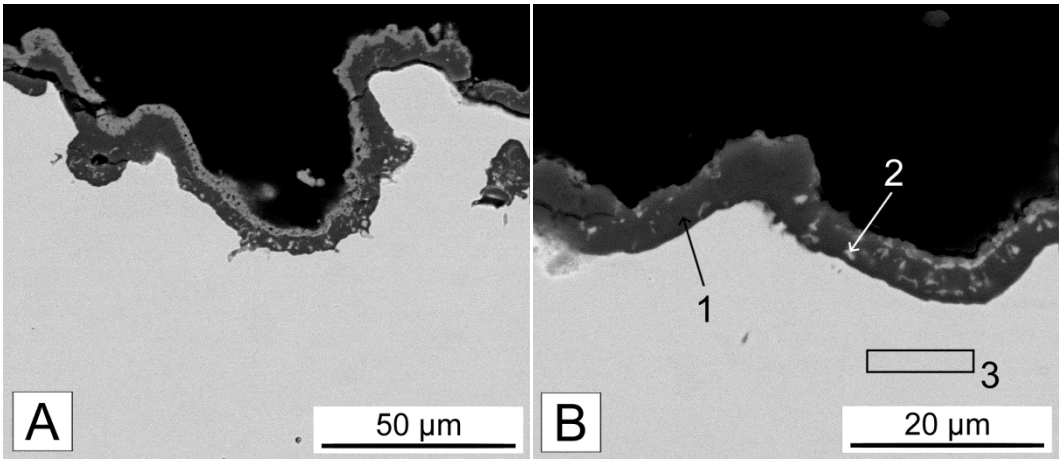

Figure 3.1.41 – SEM pictures of the standard bondcoat after 100 hours at 1100°C. The EDS analysis results are given in table 3.1.18.

1			2			3		
Element	**Weight%**	**Atomic%**	**Element**	**Weight%**	**Atomic%**	**Element**	**Weight%**	**Atomic%**
O	54.35	67.72	**O**	46.08	69.52	**O**		
Al	42.85	31.66	**Al**	25.42	22.74	**Al**	3.91	7.94
Cr	2.8	0.63	**Cr**	28.49	7.74	**Cr**	22.97	24.19
Co			**Co**			**Co**	33.45	31.07
Ni			**Ni**			**Ni**	39.05	36.42
Y			**Y**			**Y**	0.62	0.38

Table 3.1.18 – EDS results of fig. 3.1.41.

After the oxidation test the microstructure of the CoNiCrAlY bondcoat became more porous and a TGO layer grew on the external surface of the sample (fig. 3.1.39). The thermally grown oxide layer mainly consists of alumina (fig. 3.1.40 and table 3.1.17).

After 100 h the thickness of the TGO increased and some mixed oxide spots grew above the alumina scale (fig. 3.1.41 and table 3.1.18). Previous investigations [5,6] reported that the formation of spinels and mixed oxides is caused by the Al depletion within the bondcoat. When exposed to high temperatures, the bondcoat acts as a reservoir of Al, which gradually diffuses outward to provide the formation of a dense alumina scale: as a consequence, the Al amount inside the coating decreases. When the Al concentration is not enough to form a pure alumina layer, a new mixed oxide film grows, as a result of the reactions among oxygen and the other main constituents of the coating (*e.g.* Co, Ni, Cr).

Accordingly, an Al depletion layer (Fig. 3.1.40, spectrum 3), deprived of the β-phase, is formed beneath the TGO after 10 h of oxidation, and it grows thicker after 100 hours (Fig. .3.1.41, spectrum 3). The concentration profiles of the elements plotted as a function of the

coating thickness clearly reveal the decrease of the Al amount within the boncoat, caused by the formation of the TGO.

The plots also show a relevant outward diffusion of Ni from the substrate into the bondcoat and simultaneous downward diffusion of cobalt into the substrate, enhanced by the high temperature of the oxidation test. The significant amount of Ni diffusing outwards from the substrate into the top coat, which is also witnessed by the formation of visible Kirkendall porosity along the interface (Fig. 3.1.39C,E), can also account for the overall decrease in the amount of Al and for the progressive disappearance of the β phase.

Sample name	Al_2O_3 amount (wt.%)	Information
N10-f-ht	10	Full ODS bondcoat, heat treated
N10-f-10h	10	Full ODS bondcoat, after 10h at 1100°C
N10-f-100h	10	Full ODS bondcoat, after 100h at 1100°C

Table 3.1.19 – Samples based on the full ODS bondcoat containing 10 wt.% of alumina

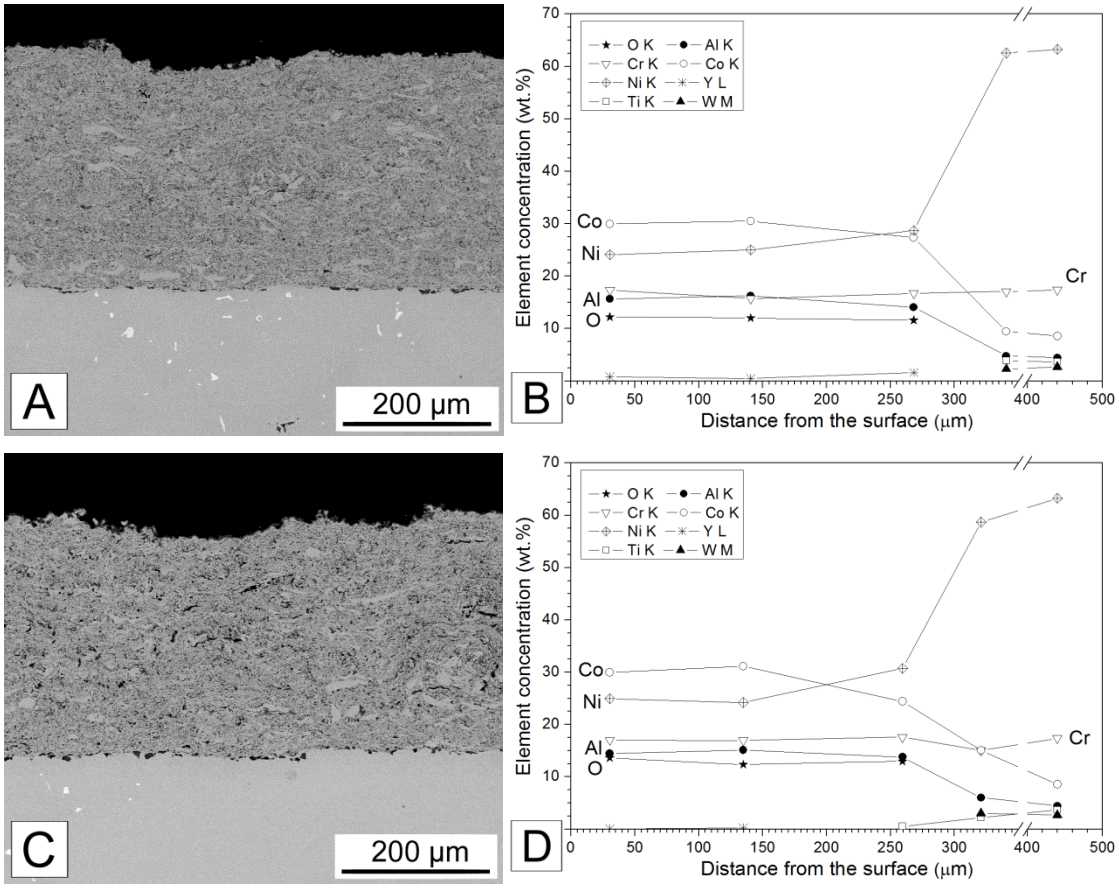

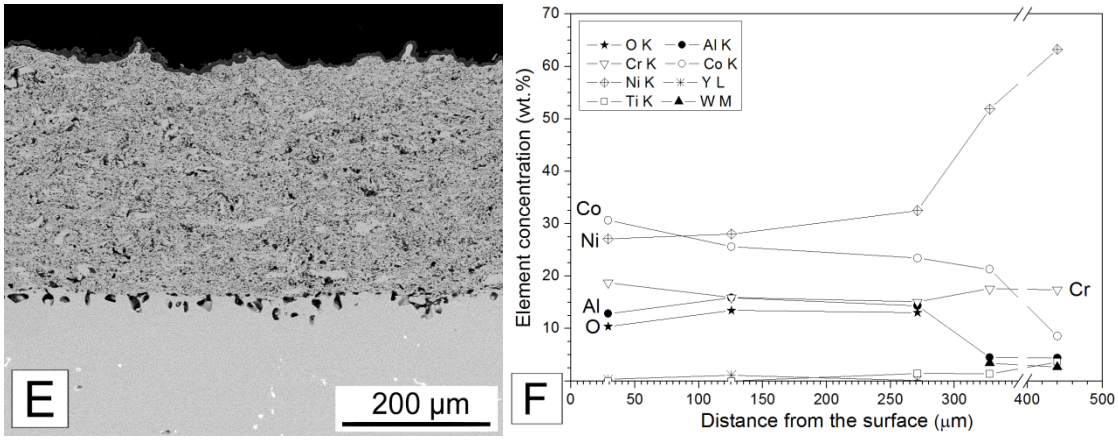

Figure 3.1.42 – SEM picture and chemical composition of the full ODS coating N10-f-ht after the vacuum heat treatment (a), 10 hours at 1100°C (b) and 100h at 1100°C (c).

Fig. 3.1.42 shows the evolution of the full ODS bondcoat microstructure during the isothermal oxidation test; the plots give more information about the diffusion movements which affected the elements within the coatings.

After 10 hours at 1100 °C the microstructure of the coating N10-f-10h appears almost unaltered. The SEM pictures 3.1.42a and 3.1.43 reveal an increase of the porosity and the formation of a thin TGO on the external surface of the sample, mainly based on Al_2O_3. The formation of the oxide scale demonstrates that (*i*) the composite coatings effectively acted as a barrier against oxygen inward diffusion during the 10 h oxidation test and (*ii*) it indicates that the amount of Al within the coating (which is globally lower compared to a standard bondcoat, due to the presence of the hard phase) was enough to promote the formation of the Al_2O_3 layer.

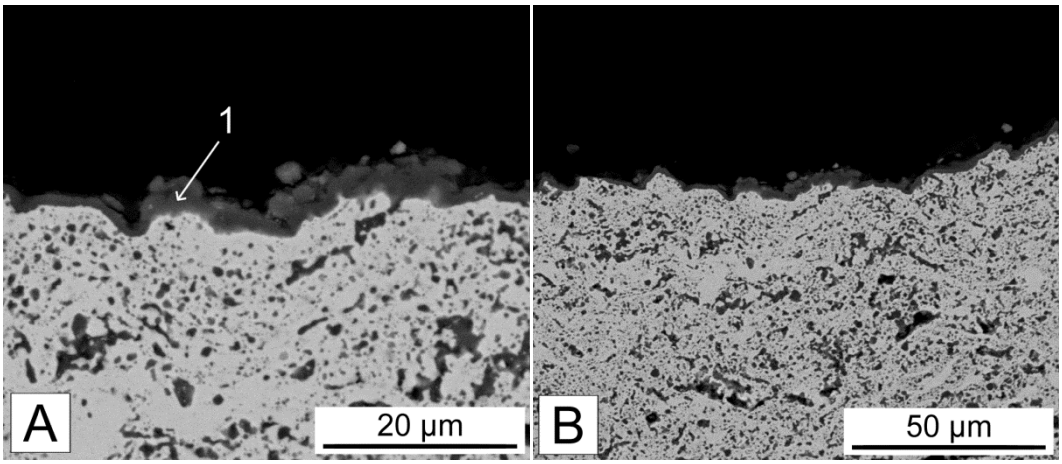

Figure 3.1.43 – SEM pictures of the ODS coating N10-f-10h after 10 hours at 1100°C. The EDS analysis results are given in table 3.1.20.

	1	
Element	**Weight%**	**Atomic%**
O	37.68	55.62
Al	40.28	35.25
Cr	5.49	2.49
Co	9.84	3.94
Ni	6.61	2.66
Y	0.1	0.03

Table 3.1.20 – EDS results of fig. 3.1.43.

After 100 hours at 1100 °C, the microstructure of the coating N10-f-100h remained still unaltered. SEM pictures 3.1.42e and 3.1.44 only show a moderate increase of the porosity and the growth of the TGO. The SEM + EDS analysis (table 3.1.21) reveals that even after 100 hours the concentration of Al within the ODS layer was enough to provide the formation of an Al_2O_3 TGO, the most performing oxide scale against high-temperature oxidation.

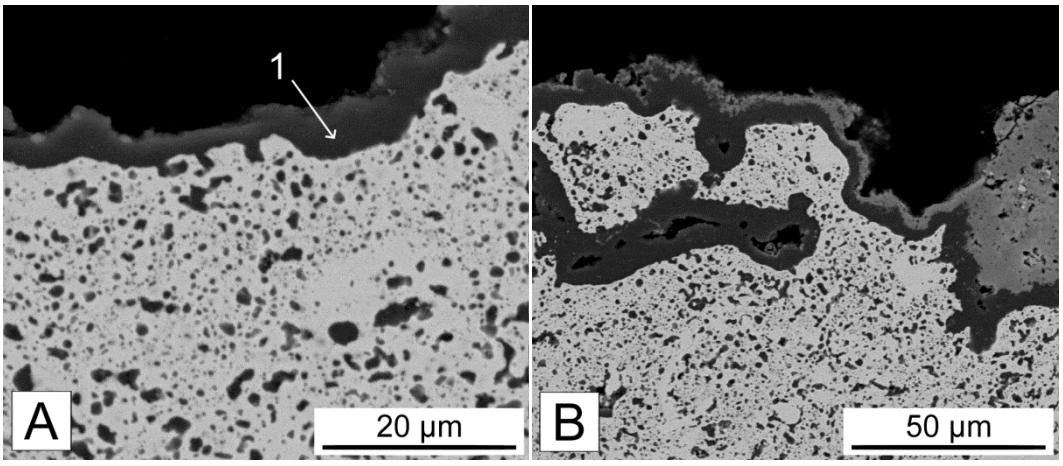

Figure 3.1.44 – SEM pictures of the ODS coating N10-f-100h after 100 hours at 1100°C. The EDS analysis results are given in table 3.1.21.

	1	
Element	**Weight%**	**Atomic%**
O	52.36	64.96
Al	47.64	35.04

Table 3.1.21 – EDS results of fig. 3.1.44.

A closer look at the external region of the coating revealed the presence of mixed oxide spots (fig. 3.1.44b). The formation of these zones is caused by defects within the coating, which accelerated inward oxygen diffusion. First an alumina layer grows and surrounds the porous

zone, then the complete oxidation of the inner region takes place, leading to the formation of a mixed oxide structure.

The plots concerning the concentration profiles of the elements (fig. 3.1.42) reveal outward diffusion of Ni and a moderate downward diffusion of Co and Cr. The amount of Ni able to diffuse outward was anyway lower compared to the traditional bondcoat (compare fig. 3.1.39), because the diffusion rates of the chemical species within the ODS layer were slightly reduced by the presence of the strengthening phase. The amount of Al within the ODS layer remained almost constant, even if its content on the outer region decreased after 100 hours at 1100 °C, probably due to the formation of the TGO.

Sample name	Al_2O_3 amount (wt.%)	Information
N10-t-ht	10	Thin ODS layer + std bc, heat treated
N10-t-10h	10	Thin ODS layer + std bc, after 10h at 1100°C
N10-t-100h	10	Thin ODS layer + std bc, after 100h at 1100°C

Table 3.1.22 – Samples based on the thin ODS layer containing 10 wt.% of alumina

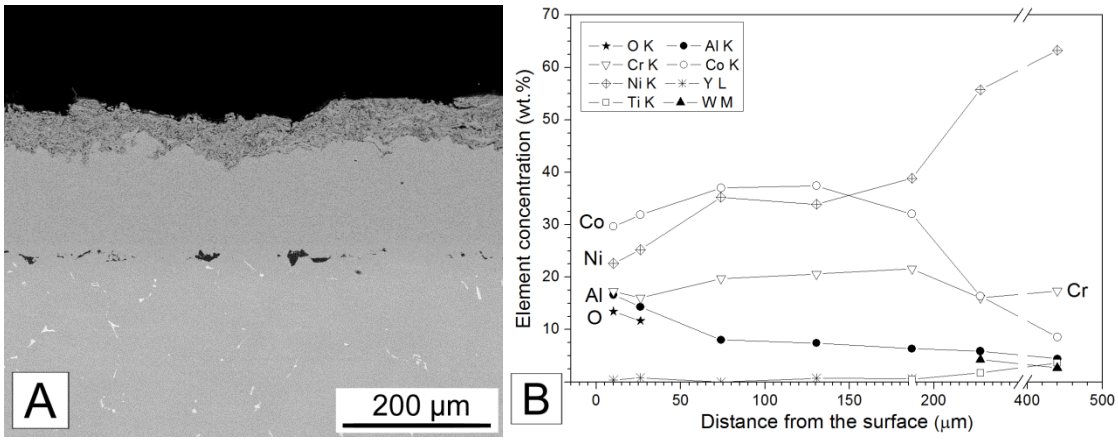

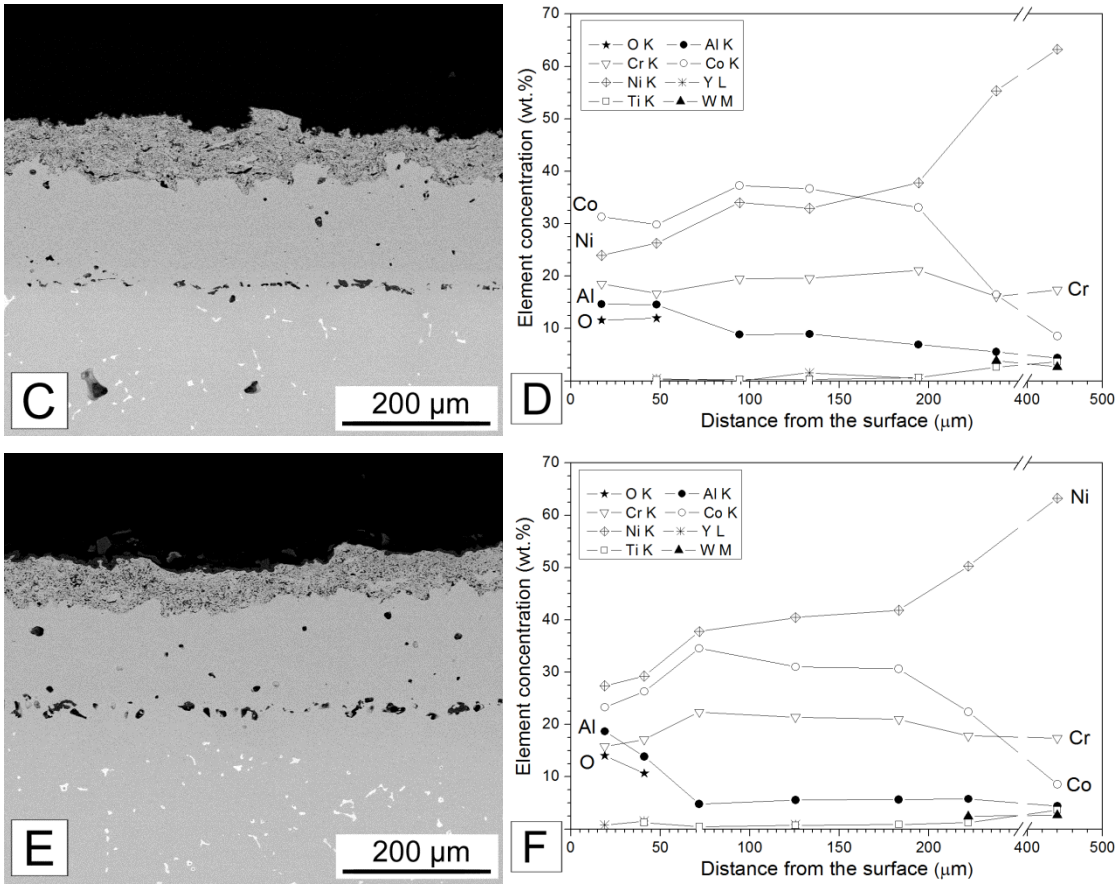

Figure 3.1.45 – SEM picture and chemical composition of the sample N10-t-ht after the vacuum heat treatment (a) and after 10 hours at 1100°C (b) and 100h at 1100°C (c).

The evolution of the microstructure of the thin ODS layer containing 10 wt.% of Al_2O_3 during the isothermal oxidation test is very similar to that of the full ODS bondcoat containing the same amount of hard phase (fig. 3.1.45).

After 10 hours at 1100 °C the microstructure is still unaltered and the outer surface features a thin and dense Al_2O_3 layer (fig. 3.1.46a,b).

Also in this case, the presence of the strengthening phase did not hinder excessively the outward diffusion of the scale former, which was able to provide the growth of the protective scale.

No Al depleted zones were detected in the standard bondcoat (fig. 3.1.46c): the thin ODS coating still effectively acts as a reservoir of aluminum for the formation of the TGO.

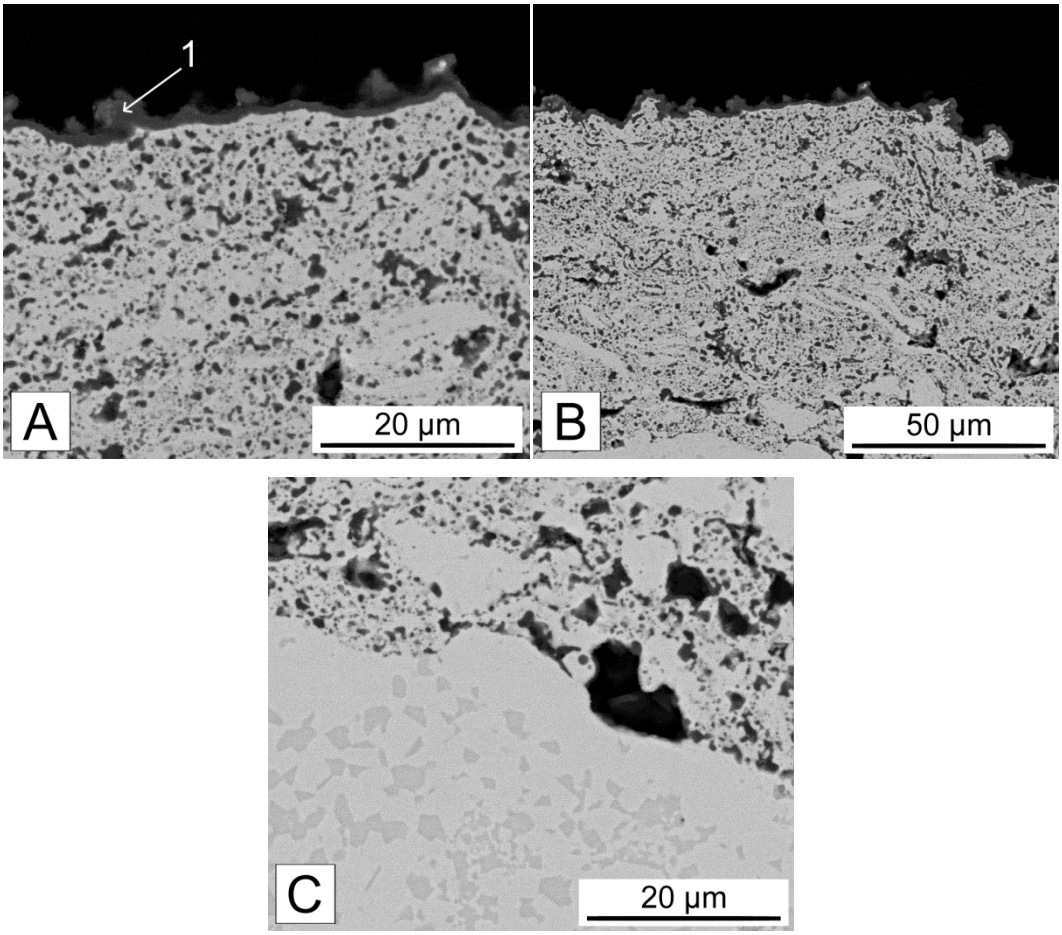

Figure 3.1.46 – SEM pictures of the sample N10-t-10h showing the pure alumina TGO and the β-phase regions within the standard bondcoat. The EDS analysis results are given in table 3.1.23.

	1	
Element	**Weight%**	**Atomic%**
O	41.34	57.44
Al	45.28	37.3
Cr	4.28	1.83
Co	4.81	1.81
Ni	4.29	1.62

Table 3.1.23 – EDS results of fig. 3.1.46.

After 100 hours at 1100 °C the oxidation phenomena led to a increase of the TGO thickness and of the porosity (fig. 3.1.45e).

The oxide scale is mainly based on Al_2O_3 (fig. 3.1.47a and table 3.1.24), even though some mixed oxide zones were detected. The formation of these spots, located above the alumina scale, was caused by the lack of Al within the coating, as demonstrated by the SEM analysis,

which shows a severe aluminum depletion across both the ODS layer and the standard bondcoat.

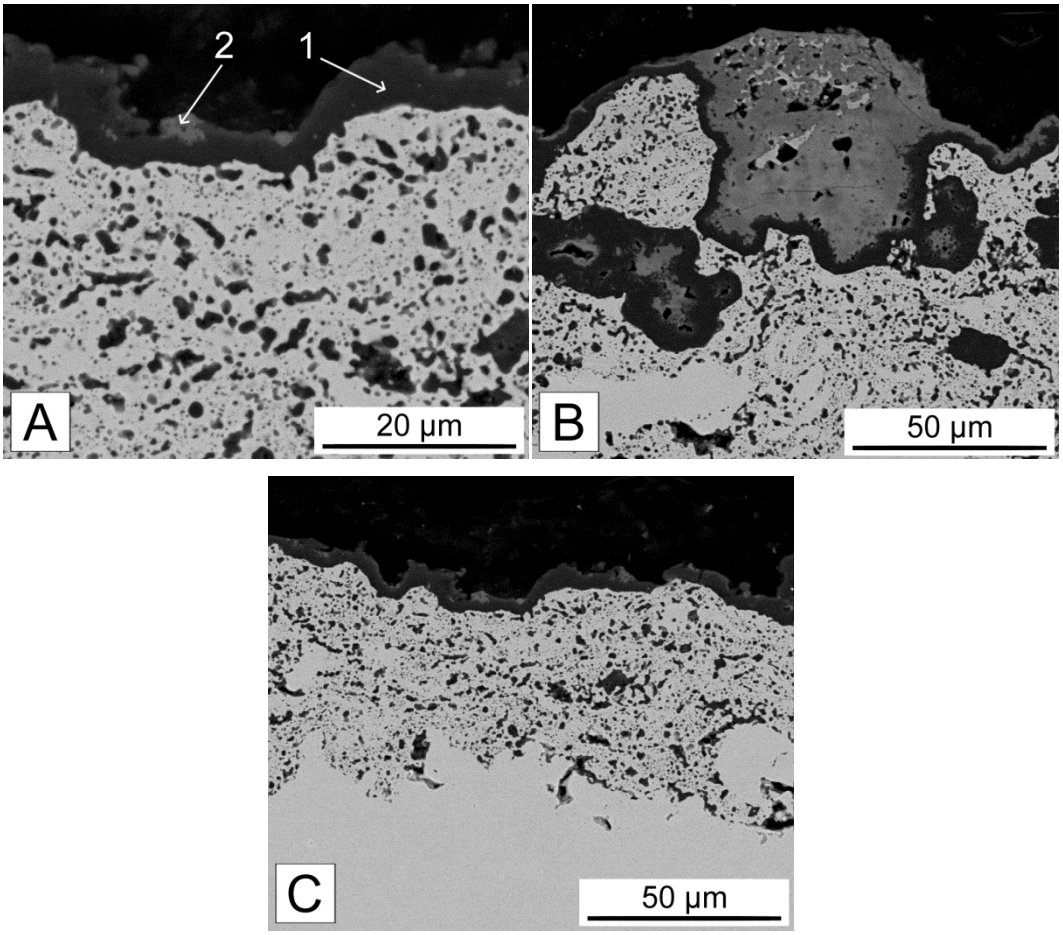

Figure 3.1.47 – SEM pictures of the sample N10-t-100h showing the pure alumina TGO, some mixed oxides regions and the β-phase depletion of the standard bondcoat. The EDS analysis results are given in table 3.1.24.

1			2		
Element	**Weight%**	**Atomic%**	**Element**	**Weight%**	**Atomic%**
O	49.52	62.33	**O**	38.67	58.95
Al	50.48	37.67	**Al**	31.47	28.45
Cr			**Cr**	4.14	1.94
Co			**Co**	14.19	5.87
Ni			**Ni**	11.53	4.79

Table 3.1.24 – EDS results of fig. 3.1.47.

The Al-depleted zone within the standard bondcoat (fig. 3.1.47c) demonstrates that the microstructure of the thin ODS layer is connected with the underlying layer and allowed the

diffusion movements of Al atoms from the CoNiCrAlY layer to the outer surface of the composite coating.

The diffusion of aluminum is the driving force that allows the growth of a dense and stable TGO. Previous investigation [7] noticed that if the metal matrix of the composite layer is not properly connected, the outward diffusion of chemical species from the inner regions to the surface is inhibited. As a consequence, the oxygen atoms react with other elements, leading to the formation of mixed oxides, detrimental to the oxidation resistance.

Concentration profiles in Fig. 3.1.45 also confirm upward diffusion of Ni from the substrate into the bond coat layer (causing the appearance of Kirkendall porosity along the interface) and downward diffusion of Co and Cr from the two-layer coating system into the substrate.

Sample name	Al_2O_3 amount (wt.%)	Information
N20-f-ht	20	Full ODS bondcoat
N20-f-10h	20	Full ODS bondcoat, after 10h at 1100°C
N20-f-100h	20	Full ODS bondcoat, after 100h at 1100°C

Table 3.1.25 – Samples based on the full ODS bondcoat containing 20 wt.% of alumina

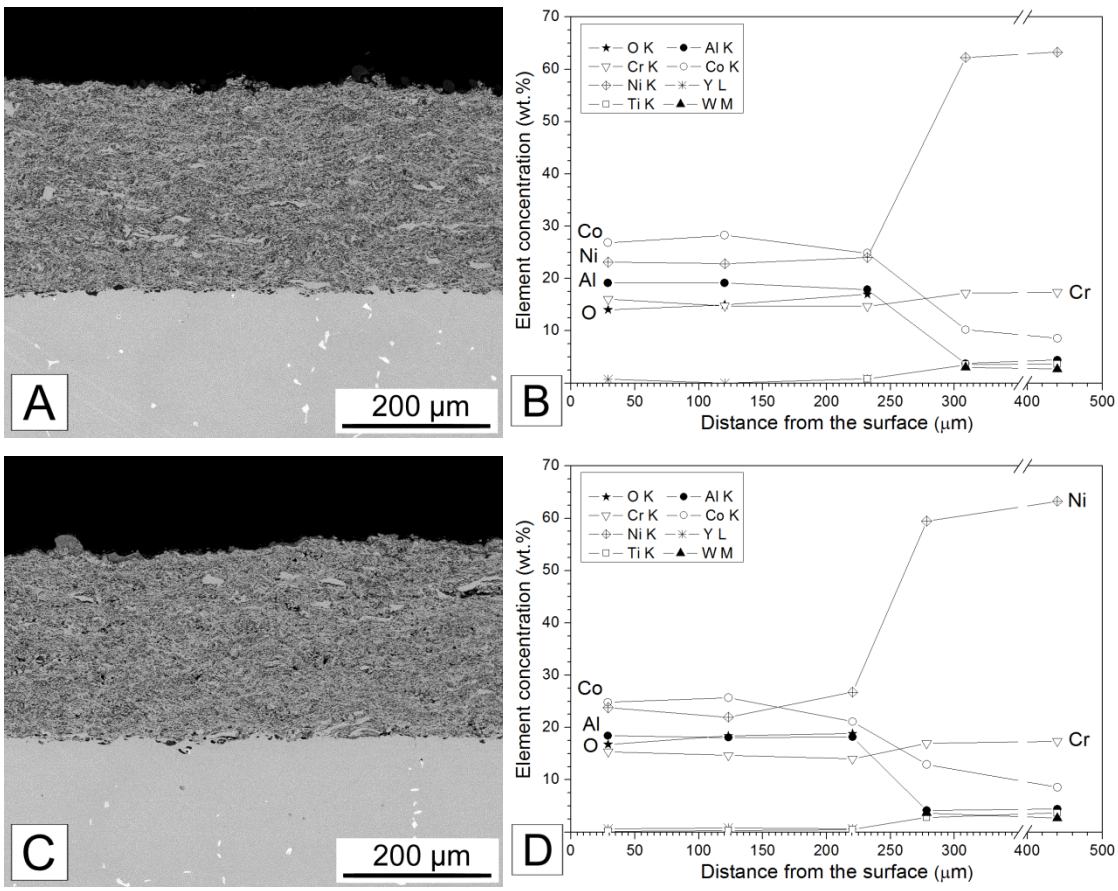

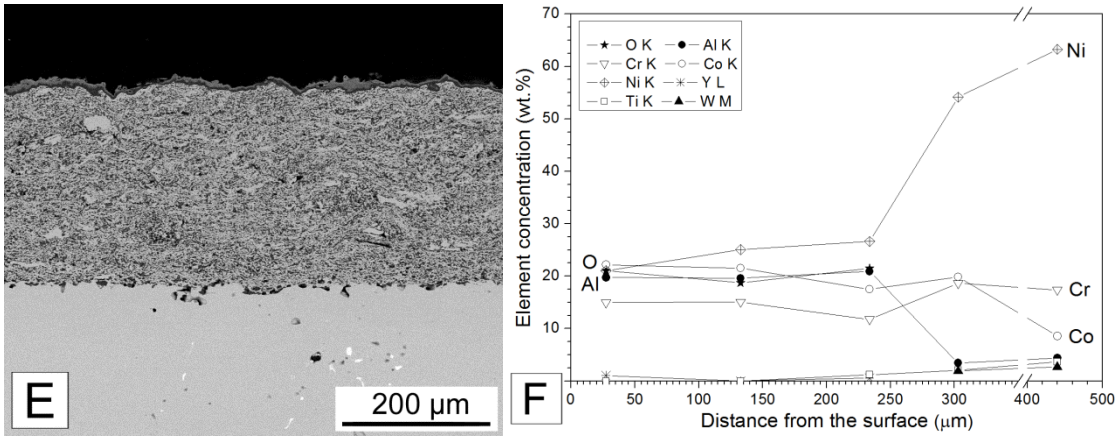

Figure 3.1.48 – SEM picture and chemical composition of the ODS bondcoat N20-f-ht after the vacuum heat treatment (a) and after 10 hours at 1100°C (b) and 100h at 1100°C (c).

Also the microstructure of the full ODS coating containing 20 wt.% of alumina was not strongly affected by the isothermal oxidation test. As expected, the high temperatures caused a moderate increase of the coating porosity and the growth of the TGO layer on the outer surface of the samples (fig. 3.1.48).

After only 10 h at 1100 °C mixed oxides were detected by SEM analysis (fig. 3.1.49a and table 3.1.26).

The formation of mixed oxide spots was caused by the lack of aluminum in the ODS coating. The concentration of metallic Al in the coating N20-f-ht was lower compared to the coatings N10-f-ht and Std-bc-ht, due to the lower overall amount of matrix phase, and its diffusion was more difficult, due to the higher amount of hard phase (20 wt.% instead of 10 wt.%). As a consequence, during the oxidation test, the ODS coating was not able to completely provide a sufficient amount of Al, necessary to form a pure alumina layer.

For the same reason, upward diffusion of Ni from the substrate into the coating seems less relevant, which is witnessed by the retention of a quite sharp concentration gradient across the interface (see concentration profiles in Fig. 3.1.48D) and by the absence of Kirkendall porosity face (Fig. 3.1.48C)

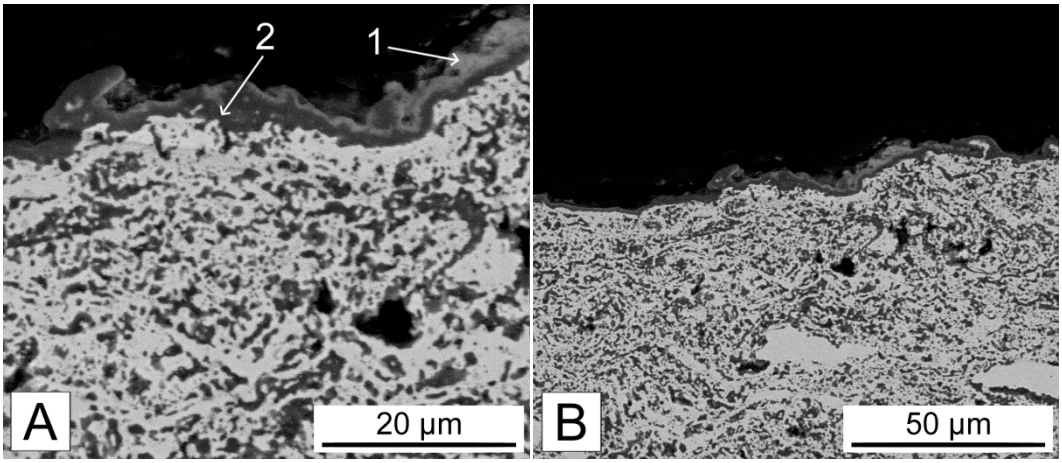

Figure 3.1.49 – SEM pictures of the sample N20-f-10h after 10 hours at 1100 °C. The EDS analysis results are given in table 3.1.26.

1			2		
Element	**Weight%**	**Atomic%**	**Element**	**Weight%**	**Atomic%**
O	25.08	49.13	**O**	44.03	60.08
Al	14.17	16.46	**Al**	43.18	34.94
Cr	29.26	17.64	**Cr**	6.43	2.7
Co	18.25	9.71	**Co**	3.17	1.18
Ni	13.24	7.07	**Ni**	2.55	0.95
Y			**Y**	0.64	0.16

Table 3.1.26 – EDS results of fig. 3.1.49.

The formation of mixed oxides in the TGO became more evident after exposing the sample for 100 hours at 1100 °C: the TGO appears thicker and the mixed oxide spots grew and formed a new layer above the alumina film (fig. 3.1.50). It should be clarified that even the standard bondcoat, used as a competitor, exhibited regions based on mixed oxides after 100 hours at 1100 °C; therefore, the addition of 20 wt.% of alumina particles was not totally detrimental to the oxidation resistance.

Anyway, this behavior should be carefully taken into account during the evaluation of the lifetime of these new TBCs, because the improved thermal shock resistance of such systems could be mitigated by the higher growth rate of the TGO, which could increase the thermal stresses between the ceramic and the metallic layers upon cooling.

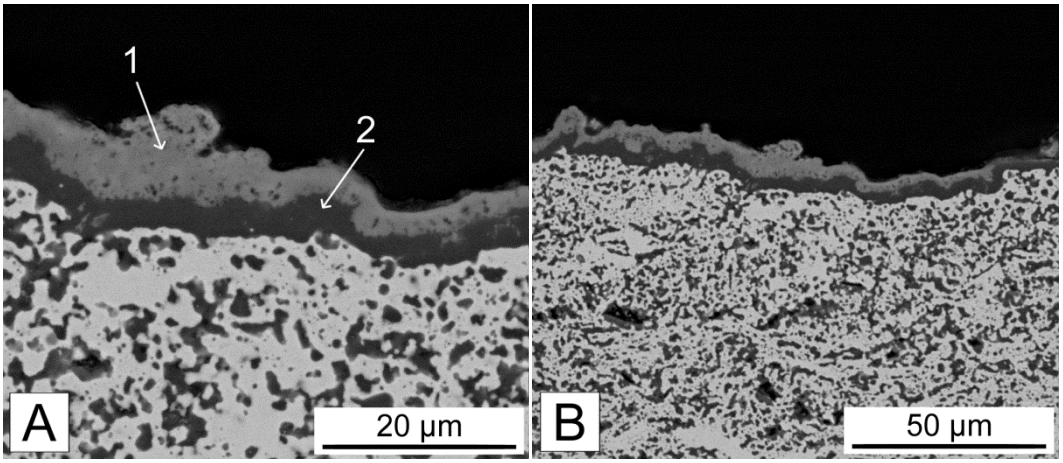

Figure 3.1.50 – SEM pictures of the sample N20-f-100h after 100 hours at 1100 °C: the double layered TGO based on alumina and mixed oxides is clearly visible. The EDS analysis results are given in table 3.1.27.

1			2		
Element	**Weight%**	**Atomic%**	**Element**	**Weight%**	**Atomic%**
O	40.75	64.49	**O**	52.48	65.06
Al	17.87	16.77	**Al**	47.52	34.94
Cr	16.53	8.05			
Co	14.38	6.18			
Ni	10.48	4.52			

Table 3.1.27 – EDS results of fig. 3.1.50.

Sample name	Al_2O_3 amount (wt.%)	Information
N20-t-ht	20	Thin ODS layer + std bc, heat treated
N20-t-10h	20	Thin ODS layer + std bc, after 10h at 1100°C
N20-t-100h	20	Thin ODS layer + std bc, after 100h at 1100°C

Table 3.1.28 – Samples based on the thin ODS layer containing 20 wt.% of alumina

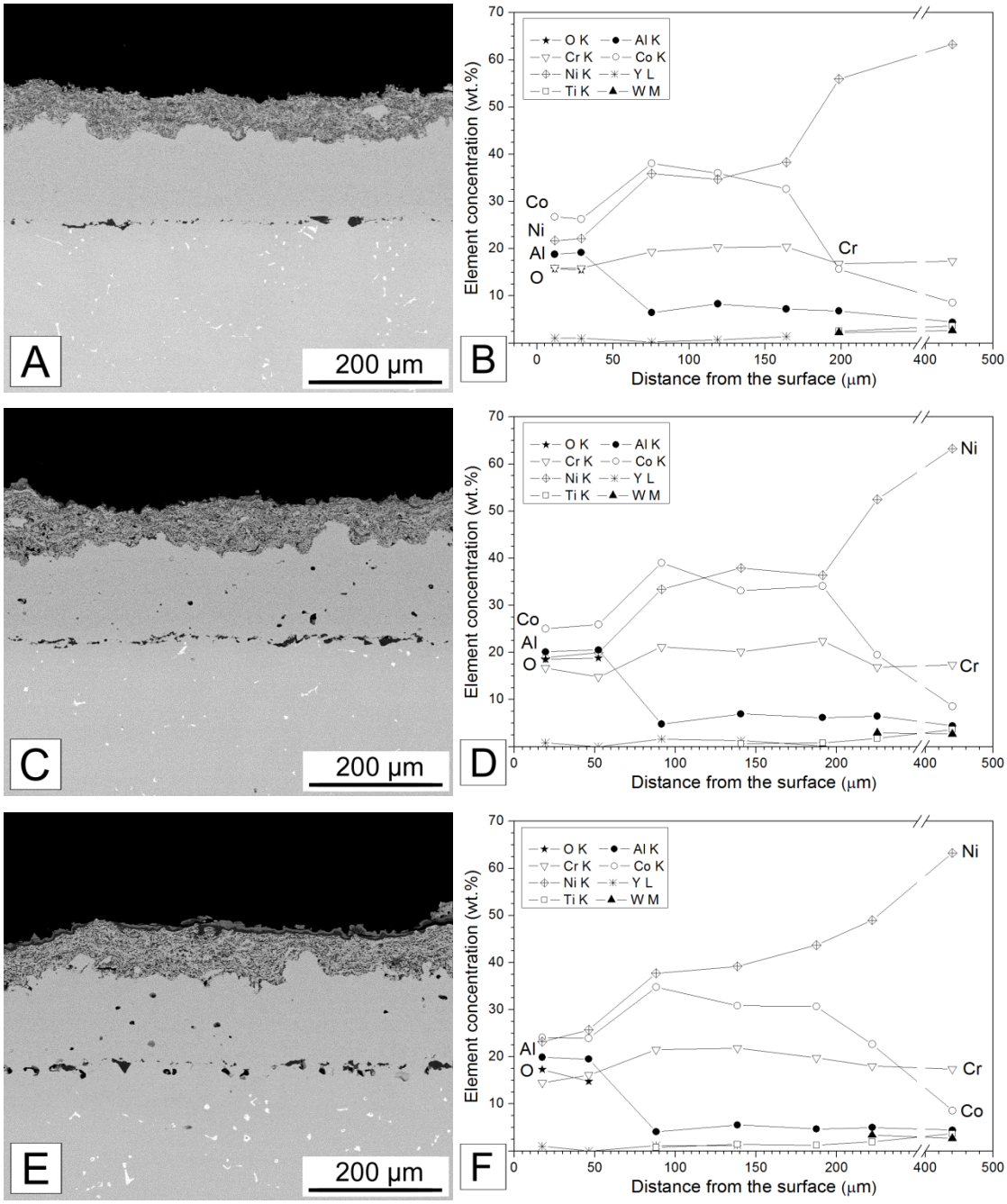

Figure 3.1.51 – SEM picture and chemical composition of the sample N20-t-ht after the vacuum heat treatment (a) and after 10 hours at 1100°C (b) and 100h at 1100°C (c).

After 10 and 100 h at 1100 °C no important changes in the microstructure of the ODS layer were detected (fig. 3.1.51).

The formation of the TGO on the outer surface of the sample confirmed that also this thin ODS layer was able to provide aluminum atoms from the metal matrix (fig. 3.1.52a). Unlike the coating N10-t-10h, the sample N20-t-10h, containing a higher fraction of Al_2O_3, features a

thin Al-depleted region located at the outer surface of the standard bondcoat even after only 10 h (fig. 3.1.52b).

This region, as previously discussed, is formed due to the lack of aluminum within the bondcoat, caused by its outward diffusion to form the TGO. Since the ODS layer of the sample N20-t-ht contains a lower fraction of metal matrix, the overall amount of Al inside the composite coating is lower. As a consequence, the need for further Al atoms is compensated by diffusion from the underlying pure CoNiCrAlY coating.

At the end of the 100 h oxidation test, the Al-depleted region affected the entire coating. Unlike the coating N10-t-100h, the TGO consists of a mixed oxide layers, grown above the alumina scale (fig. 3.1.53 and table 3.1.30).

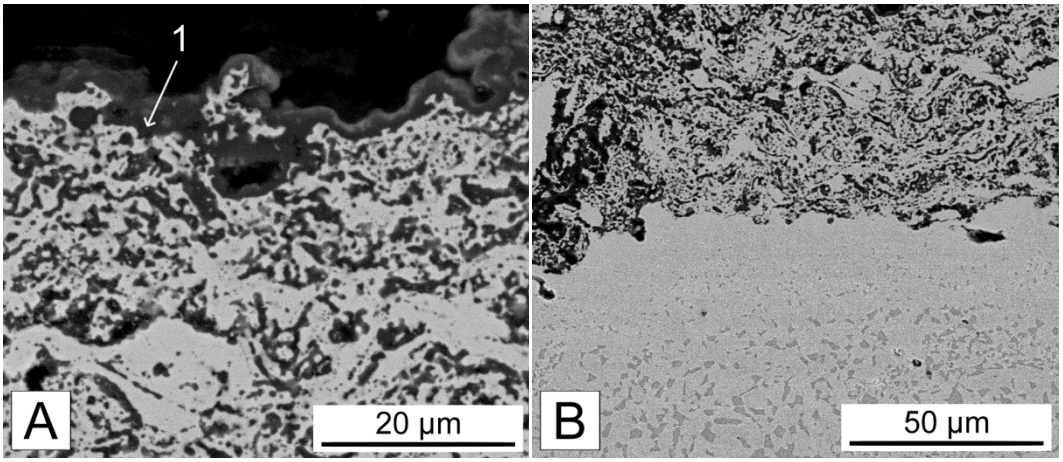

Figure 3.1.52 – SEM pictures of the sample N20-t-10h showing the pure alumina TGO (a) and the β-phase depletion layer within the standard bondcoat (b).
The EDS analysis results are given in table 3.1.29.

	1	
Element	**Weight%**	**Atomic%**
O	32.72	51.33
Al	38.71	36.01
Cr	8.39	4.05
Co	11.64	4.96
Ni	8.54	3.65
Y	0.01	0

Table 3.1.29 – EDS results of fig. 3.1.52.

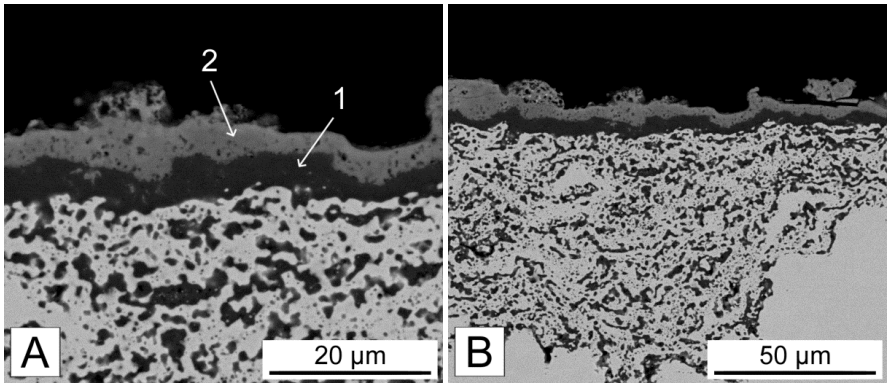

Figure 3.1.53 – SEM pictures of the sample N20-t-100h showing the double layered TGO (a) and the large Al depleted region (b). The EDS analysis results are given in table 3.1.30.

1			2		
Element	**Weight%**	**Atomic%**	**Element**	**Weight%**	**Atomic%**
O	53.09	65.62	**O**	43.72	65.69
Al	46.91	34.38	**Al**	22.7	20.22
			Cr	7.01	3.24
			Co	15.8	6.45
			Ni	10.76	4.41

Table 3.1.30 – EDS results of fig. 3.1.53.

Sample name	Al_2O_3 amount (wt.%)	Information
N30-f-ht	30	Full ODS bondcoat
N30-f-10h	30	Full ODS bondcoat, after 10h at 1100°C
N30-f-100h	30	Full ODS bondcoat, after 100h at 1100°C
N30-f-1000h	30	Full ODS bondcoat, after 1000h at 1100°C

Table 3.1.31 – Samples based on the full ODS bondcoat containing 30 wt.% of alumina.

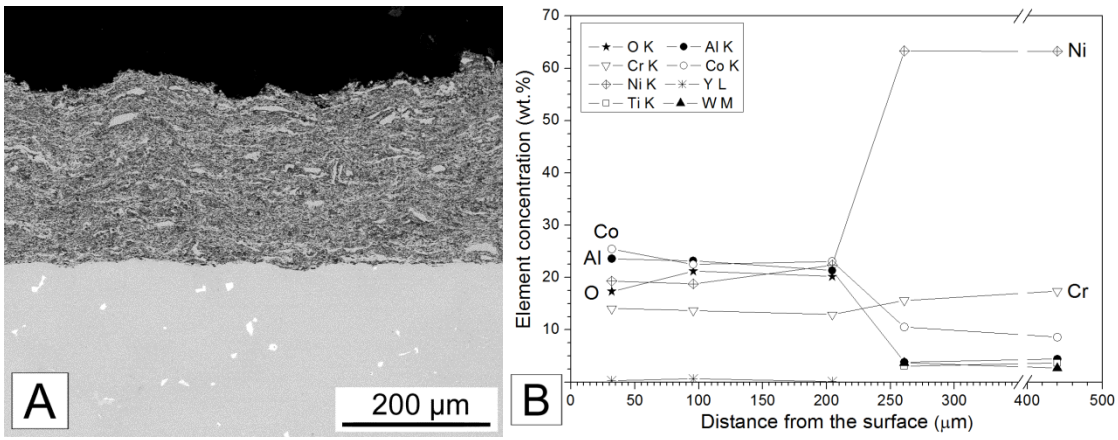

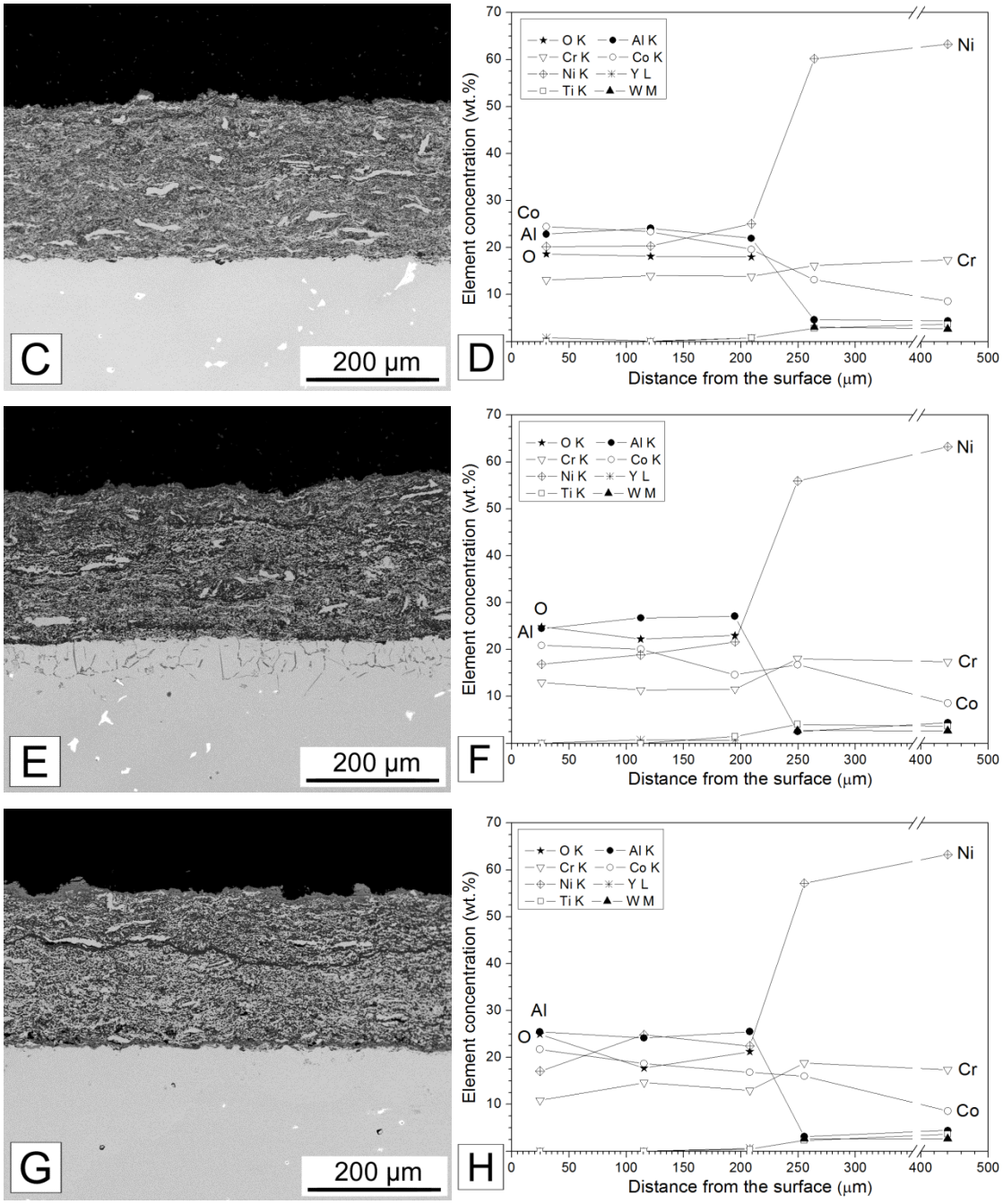

Figure 3.1.54 – SEM picture and chemical composition of the sample N30-f-ht after the vacuum heat treatment (a) and after 10 h (b), 100 h (c) and 1000 h at 1100 °C (d).

The microstructure of the coating N30-f-ht, containing the highest amount of hard phase, is gradually affected by the high-temperature oxidation test (fig. 3.1.54).

The changes in the coating structure are caused by the low amount of metal matrix, and the consequent low amount of Al which is needed for the formation of the protective scale, and by the slower diffusion processes occurring in this system.

The lack of aluminum and the defects in the coating microstructure (*i.e.* non homogenous zones and pores) inhibited the formation of a dense TGO on the external surface of the sample: SEM analysis shows that in some regions (probably having more defects) the TGO grew inside the composite matrix.

Furthermore, even after only 10 h at 1100 °C the TGO was already based on mixed oxides (fig 3.1.55 and table 3.1.32).

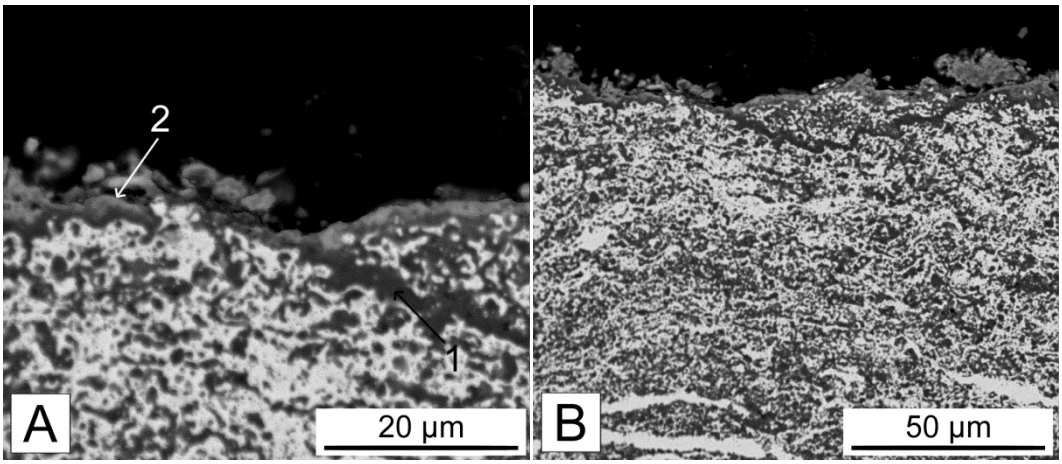

Figure 3.1.55 – SEM pictures of the sample N30-f-10h showing the mixed oxides layer formed on the external surface of the coating and the alumina scale grew inside the coating. The EDS analysis results are given in table 3.1.32.

	1			2	
Element	**Weight%**	**Atomic%**	**Element**	**Weight%**	**Atomic%**
O	43.69	58.65	**O**	30.89	53.53
Al	48.15	38.32	**Al**	22.96	23.6
Cr	3.14	1.3	**Cr**	18.22	9.72
Co	2.33	0.85	**Co**	16.43	7.73
Ni	1.88	0.69	**Ni**	11.49	5.43
Y	0.81	0.2	**Y**		

Table 3.1.32 – EDS results of fig. 3.1.55.

After 100 hours the oxidation phenomena became more severe: the alumina scale continued to grow internally; the outer TGO is based on mixed oxides (fig. 3.1.56 and table 3.1.33). Moreover, the oxidation phenomena seem also to affect the composite microstructure.

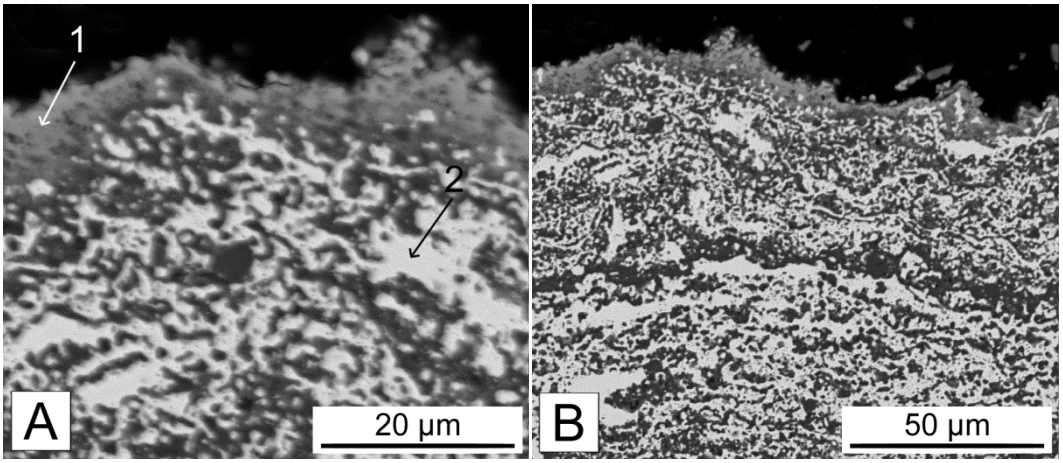

Figure 3.1.56 – SEM pictures of the sample N30-f-100h showing the mixed oxides formed on the surface of the coating (a) and the alumina scale inside the ODS layer (b). The EDS analysis results are given in table 3.1.33.

1			2		
Element	**Weight%**	**Atomic%**	**Element**	**Weight%**	**Atomic%**
O	39.37	63.4	**O**		
Al	17.17	16.4	**Al**	0.24	0.5
Cr	20.43	10.12	**Cr**	18.68	20.57
Co	12.06	5.27	**Co**	45.4	44.11
Ni	10.96	4.81	**Ni**	35.69	34.81

Table 3.1.33 – EDS results of fig. 3.1.56.

At the end of the test, the full ODS bondcoat N30-f-1000h consists of two different regions, separated by a TGO grown inside the coating. The outer region appears to be more oxidized than the inner layer, because the TGO formed within the matrix acted as a barrier, protecting the underlying materials from oxidation (fig. 3.1.54g, 3.1.57 and table 3.1.34).

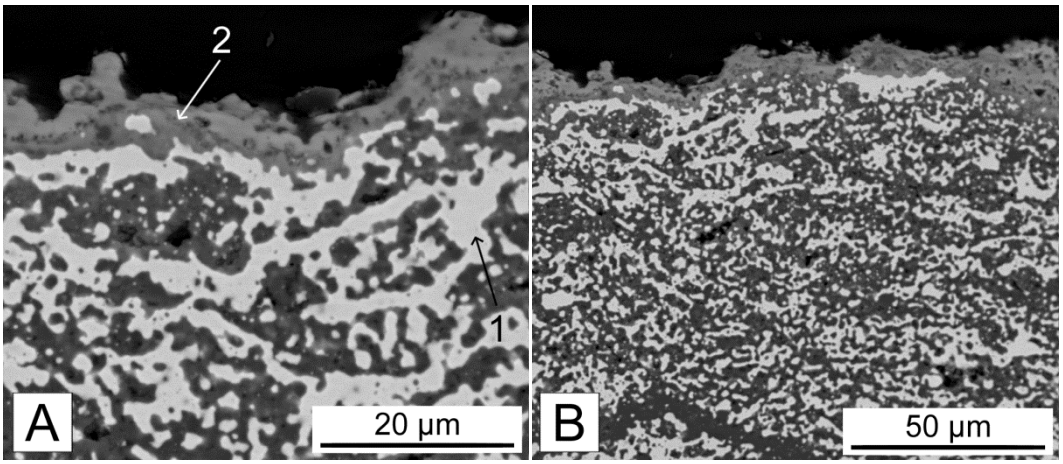

Figure 3.1.57 – SEM pictures of the sample N30-f-1000h showing the mixed oxides formed on the surface of the coating (a) and the alumina scale inside the ODS layer (b). The EDS analysis results are given in table 3.1.34.

	1			2	
Element	**Weight%**	**Atomic%**	**Element**	**Weight%**	**Atomic%**
O	48.95	71.76	**O**		
Al	13.69	11.9	**Al**	0.51	1.08
Cr	27.42	12.37	**Cr**	13.95	15.41
Co	5.21	2.07	**Co**	47.13	45.93
Ni	4.73	1.89	**Ni**	38.42	37.59

Table 3.1.34 – EDS results of fig. 3.1.57.

Sample name	**Al_2O_3 amount (wt.%)**	**Information**
N30-t-ht	30	Thin ODS layer + std bc, heat treated
N30-t-10h	30	Thin ODS layer + std bc, after 10h at 1100°C
N30-t-100h	30	Thin ODS layer + std bc, after 100h at 1100°C
N30-t-1000h	30	Thin ODS layer + std bc, after 1000h at 1100°C

Table 3.1.35 – Samples based on the thin ODS layer containing 30 wt.% of alumina

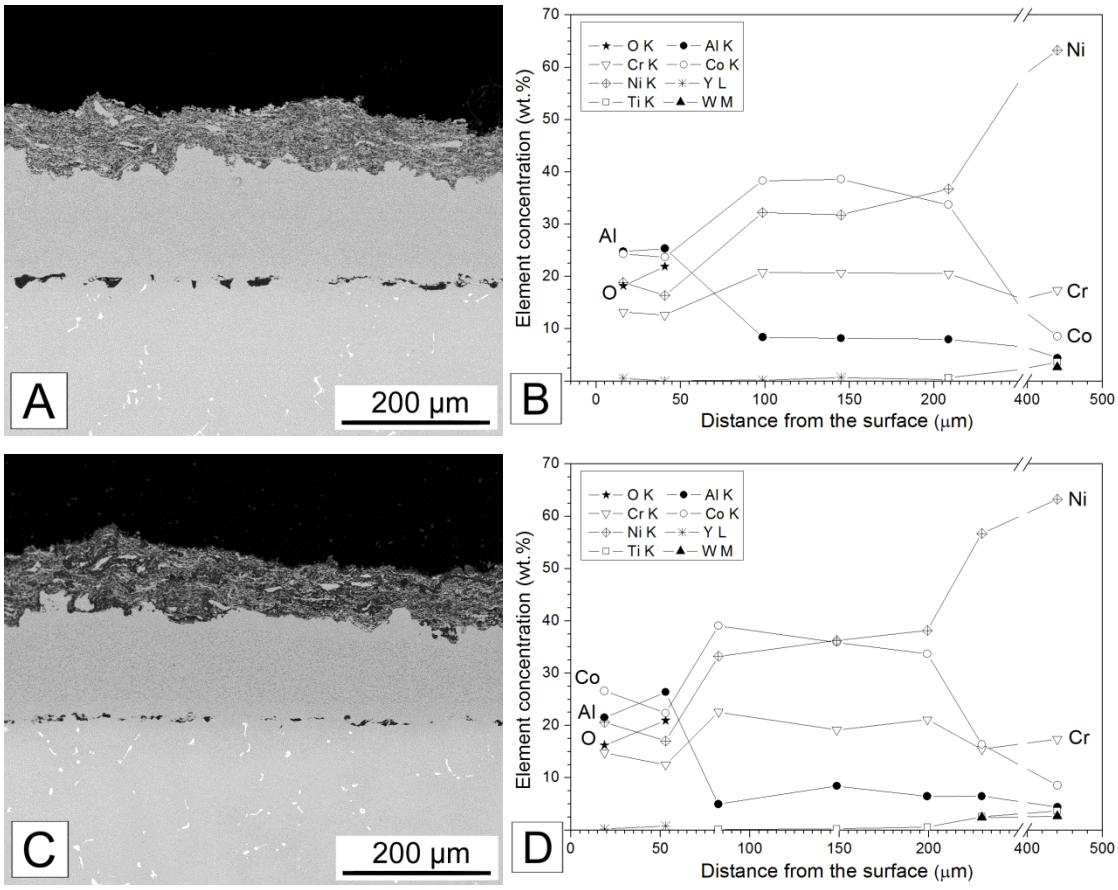

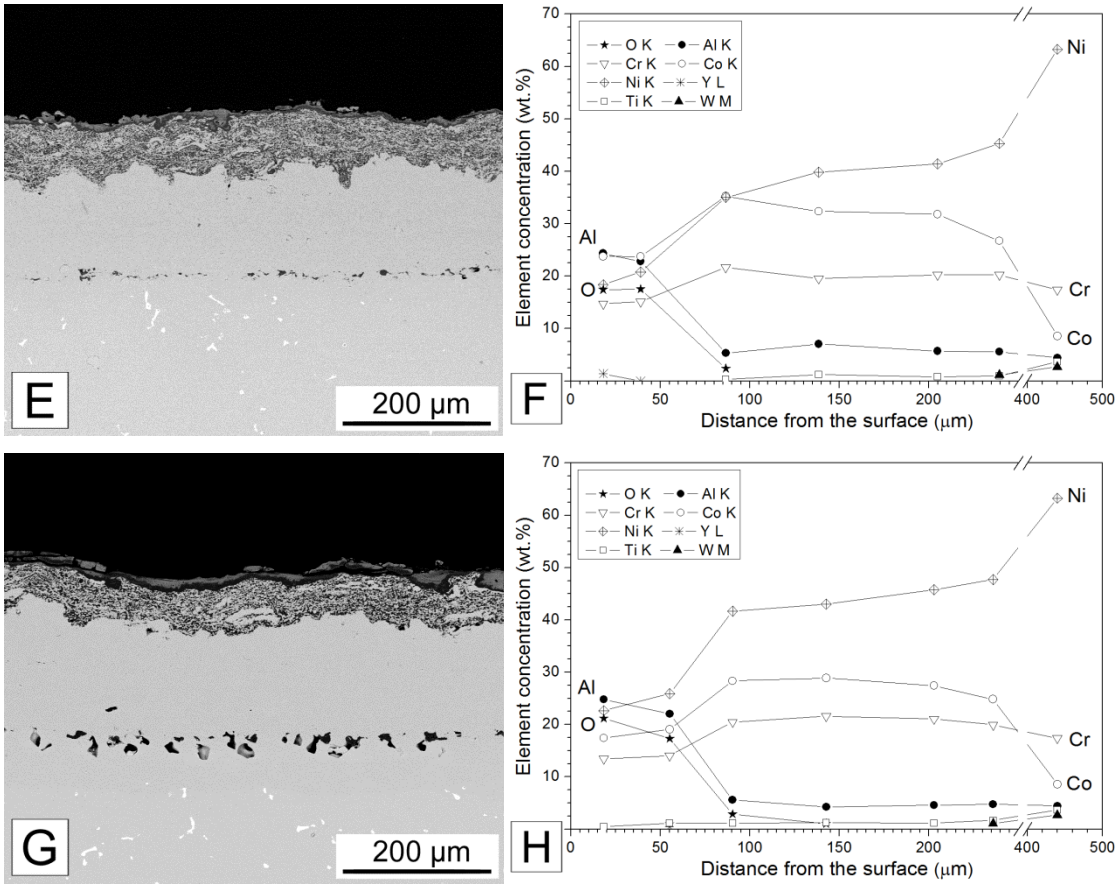

Figure 3.1.58 – SEM picture and chemical composition of the sample N30-t-ht after the vacuum heat treatment (a) and after 10 hours (b), 100 h (c) and 1000 h at 1100 °C (d).

Compared to the full ODS bondcoat N30-f-ht, the sample based on the hybrid system consisting of a thin ODS layer applied above a standard bondcoat (N30-t-ht) preserved its microstructure during the oxidation test (fig. 3.1.58). The TGO grew on the external surface and no severe oxidation involved the underlying material, even after 1000 hours at 1100 °C. This behavior can be explained considering that, during the test, the standard bondcoat acted as an Al reservoir more effectively than the full ODS coating, because the aluminum amount within the pure CoNiCrAlY layer was higher. As a consequence, Al could easily diffuse outward, providing the formation of a TGO on the external surface of the sample (fig. 3.1.59 and table 3.1.36).

As previously observed on the other sample N20-t-ht, the alumina TGO was gradually converted into a double layered structure, consisting of a mixed oxide layer formed above the Al_2O_3 scale.

The Al depleted zone in the standard bondcoat of the sample N30-t-10h (fig. 3.1.59b) confirms that even after only 10 hours a relevant amount of Al diffused outward, to compensate the lack of scale former in the thin ODS layer.

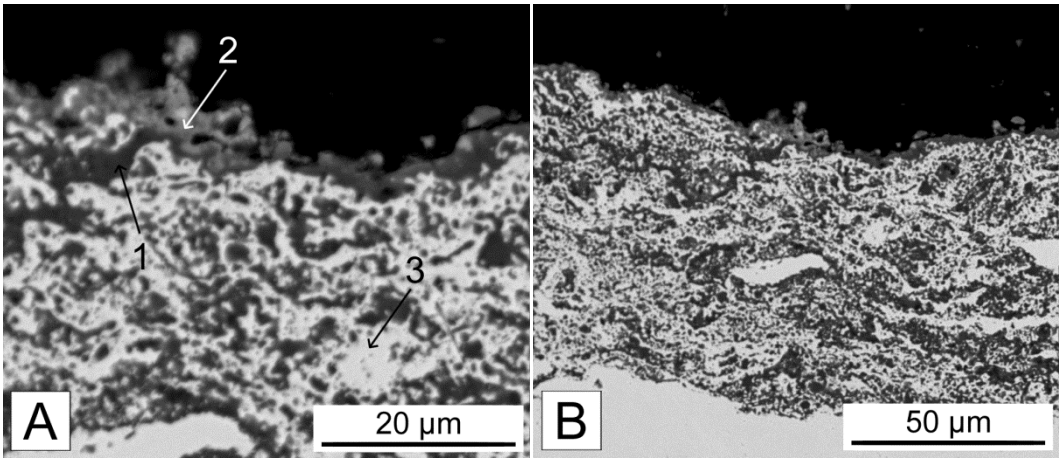

Figure 3.1.59 – SEM pictures of the sample N30-t-10h after 10 hours at 1100°C. The EDS analysis results are given in table 3.1.36.

1			2			3		
Element	**Weight%**	**Atomic%**	**Element**	**Weight%**	**Atomic%**	**Element**	**Weight%**	**Atomic%**
O	44.32	58.76	**O**	30.14	53.31	**O**		
Al	49.23	38.71	**Al**	20.3	21.29	**Al**	2.65	5.45
Cr	4.16	1.7	**Cr**	27.41	14.92	**Cr**	23.59	25.19
Co	1.28	0.46	**Co**	14.07	6.75	**Co**	41.78	39.35
Ni	1.01	0.36	**Ni**	7.09	3.42	**Ni**	31.29	29.58
Y			**Y**	1	0.32	**Y**	0.7	0.43

Table 3.1.36 – EDS results of fig. 3.1.59.

After 100 hours the Al depleted region (containing no β phase) within the standard bondcoat almost extended to the whole section (also because nickel diffused upwards from the substrate into the pure bondcoat layer, leaving Kirkendall porosities along the interface, as noted previously) and the mixed oxide layer, formed above the alumina scale, became clearly visible (fig. 3.1.60 and table 3.1.37).

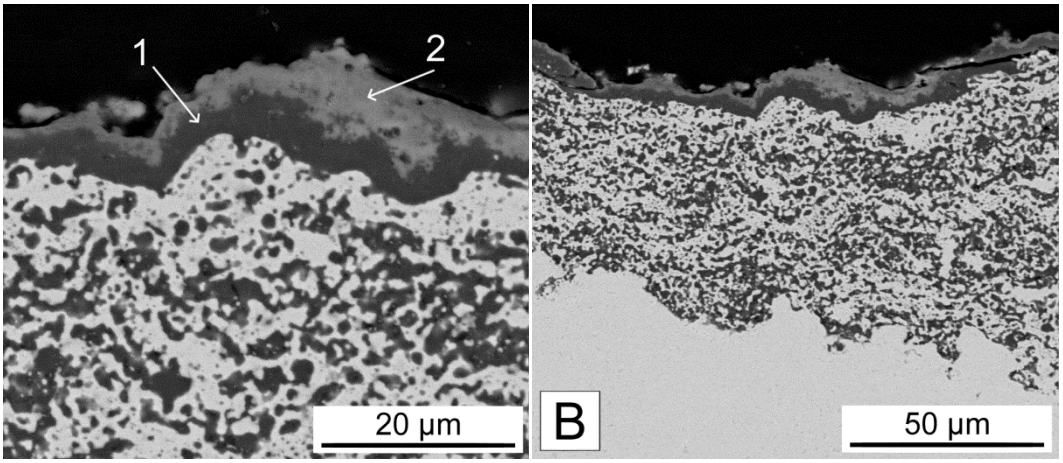

Figure 3.1.60 – SEM pictures of the sample N30-t-100h showing the double layered TGO (a) and the β-phase depletion layer within the standard bondcoat (b). The EDS analysis results are given in table 3.1.37.

	1			2	
Element	**Weight%**	**Atomic%**	**Element**	**Weight%**	**Atomic%**
O	46.06	59.02	**O**	18.03	38.54
Al	53.94	40.98	**Al**	17.5	22.18
Cr			**Cr**	23.59	15.52
Co			**Co**	23.18	13.45
Ni			**Ni**	17.7	10.31

Table 3.1.37 – EDS results of fig. 3.1.60.

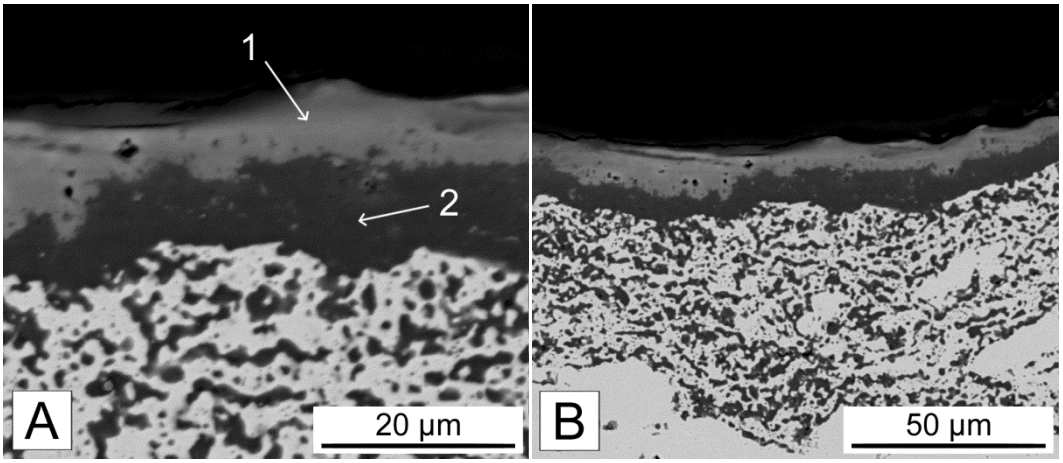

Figure 3.1.61 – SEM pictures of the sample N30-t-1000h showing the double layer TGO at different magnifications. The EDS analysis results are given in table 3.1.38.

1			2		
Element	**Weight%**	**Atomic%**	**Element**	**Weight%**	**Atomic%**
O	39.79	63.19	**O**	49.27	62.4
Al	20.08	18.9	**Al**	49.43	37.12
Cr	12.08	5.9	**Cr**	0.62	0.24
Co	19.79	8.53	**Co**	0.42	0.14
Ni	7.58	3.28	**Ni**	0.26	0.09
Y	0.69	0.2	**Y**		

Table 3.1.38 – EDS results of fig. 3.1.61.

The comparison between the sample N30-t-1000h and the sample M30-tbc at the end of the oxidation test shows important differences in the high temperature behavior of such coatings.
Despite the same amount of the hard phase dispersed inside these samples, the improved microstructure of the coating deposited using the new powder batch N30 acted more effectively as a barrier against the oxygen inward diffusion. As a consequence the TGO grew on the external surface of the sample, not at the interface between the thin ODS layer and the standard bondcoat (fig. 3.1.61 and table 3.1.38).

Concluding remarks

The optimization of the milling process, achieved by using more suitable starting materials and a different ball-to powder mass ratio, led to the deposition of more homogenous and denser ODS coatings. The microstructure of the ODS layers is strongly influenced by the microstructure of the ODS feedstock powders. As a consequence, improving the milling process permitted to obtain more performing coatings.
Full ODS bondcoats and hybrid systems based on thin ODS layers applied above a standard bondcoat were successfully deposited.
Regardless of the amount of hard phase within the coating (10, 20 and 30 wt.%), the microstructure of all the samples is very similar: coatings consist of small oxide inclusions surrounded by the metal matrix, forming a composite system.
The vacuum heat treatment allowed interdiffusion phenomena, promoting the migration of elements within the coating and between the coating and the substrate. As a consequence, the amount of Al in the outer regions slightly increased after the treatment.
Furthermore, the thermal treatment also led to a complete recovery of the plastic deformation occurred during the milling process, which affected the metal matrix of the ODS powders.

The XRD patterns of the samples after the diffusion treatment show a more ordered crystalline structure, with sharper peaks.

The recovery of the work hardening also caused the decrease of the Vickers hardness of the ODS coatings. Despite this the overall hardness values are still higher than those of the standard bondcoat, because the inclusions of aluminum oxide enhanced the hardness of these systems.

The roughness of the ODS coatings is influenced by the Al_2O_3 amount, because the concentration of the hard phase affected the particle size of the powder batches during the milling process. The use of coarser particles (*i.e.* powders containing 10 wt.% of Al_2O_3) led to the deposition of coatings having higher roughness, whereas finer particles resulted in coatings having a lower roughness.

The 3D images acquired using an optical profilometer show that the texture of the standard bondcoat is more regular, whereas the ODS layers have higher peaks surrounded by smoother regions.

Roughness and surface texture may affect the adhesion of the topcoat and could influence the lifetime of TBCs, therefore more tests will be necessary to completely evaluate their effect on the high-temperature resistance of these ODS layers.

The isothermal oxidation resistance is controlled and influenced by the possibility of the tested coatings to form an alumina layer on the external surface, necessary to provide the protection of the underlying material from further oxidation.

As a consequence, the growth of an alumina-based oxide scale on the outer surface of such systems may take place only if a proper amount of aluminum could be provided by the inner regions. The reservoir of scale former is granted only if the metal matrix of the ODS layer is connected, in order to create a path for the outward diffusion of such element.

As far as the full ODS coatings are concerned, oxidation tests demonstrated that the system containing the lowest fraction of oxide inclusions was able to effectively act as Al reservoir. Therefore, during the oxidation test, it allowed the formation of a dense TGO mainly based on Al_2O_3. This was possible because i) the microstructure was properly connected and ii) the Al amount within the CoNiCrAlY metal matrix was enough to compensate the Al depletion during the tests.

The TGO formed on ODS coatings containing higher fractions of hard phase (*i.e.* 20 and 30 wt.%) usually consists of mixed oxides. Typically, the oxide scale is based on an alumina inner layer followed by a mixed oxides zone.
The formation of the double layered TGO is caused by the severe Al depletion which affected the ODS coatings during the isothermal oxidation test.
The Al depletion is made more critical by the overall lower availability of aluminum atoms (because of the lower fraction of metal matrix) and the decreased outward diffusion rate of this element, due to the presence of a relevant amount of oxide inclusions, which hinder diffusion movements.
The full ODS bondcoat containing 20 wt.% of alumina was still able to provide the formation of a TGO on the external surface of the sample, even if this layer was based on mixed oxides, as previously stated.
The full ODS bondcoat with the highest fraction of Al_2O_3 experienced a severe oxidation, because the TGO grew inside the composite coatings and it did not act as a barrier against further oxygen inward diffusion.

The hybrid systems based on a thin ODS layer deposited above a standard bondcoat generally exhibited a better isothermal oxidation resistance. This behavior could be explained considering that the underlying standard bondcoat layer acted as Al reservoir during the test, providing the proper amount of scale former, necessary to form a stable TGO.
It should be also noticed that the outward diffusion of Al was made possible because the metal matrix of the ODS layers was properly connected with the underling coating, creating a path for the migration of Al atoms.
The sample with the ODS coating containing 10 wt.% of Al_2O_3 showed the best isothermal oxidation resistance. Even after 100 hours the TGO was mainly based on alumina and the microstructure of the ODS coatings remained unaltered.
Samples having ODS layers containing higher fractions of Al_2O_3 led to the formation of a double layered TGO, based on an alumina layer and a mixed oxide region.
As previously discussed, the formation of the mixed oxide layer was caused by the severe Al depletion within both the ODS layer and the underlying standard bondcoat.
The sample containing the highest amount of alumina, tested up to 1000 hours, revealed that even at the end of the test the ODS layer retained its original microstructure and no severe oxidation of the coating was observed, confirming the hypothesis that a dense and properly

connected microstructure could effectively promote the formation of a TGO and could act as a barrier against the oxygen inward diffusion.

3.1.3 Coating analysis: Section three

As sprayed coatings

Section three concerns the investigation of coatings deposited by HVOF using methane as gas fuel instead of hydrogen. The 3 powder batches N10, N20 and N30 were employed as a feedstock materials.

Samples were labeled Z10-f, Z20-f and Z30-f respectively. A description of these coatings is given in table 3.1.39.

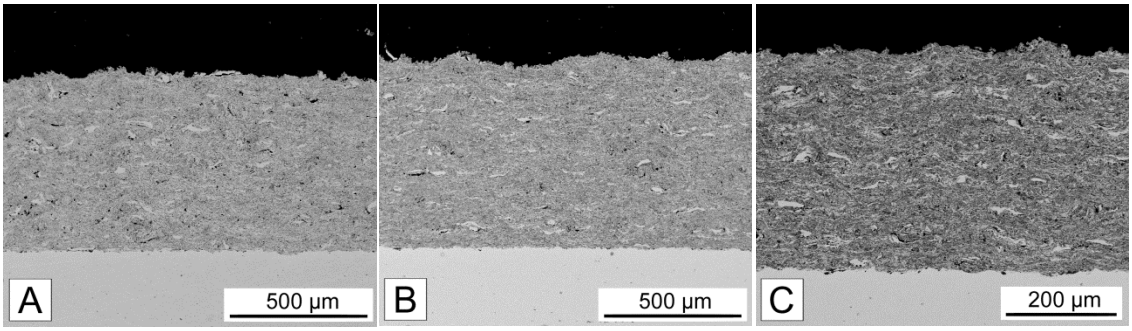

Figure 3.1.62 – SEM pictures of the coatings Z10-f (a), Z20-f (b) and Z30-f (c), deposited by HVOF using methane as a fuel gas instead of hydrogen.

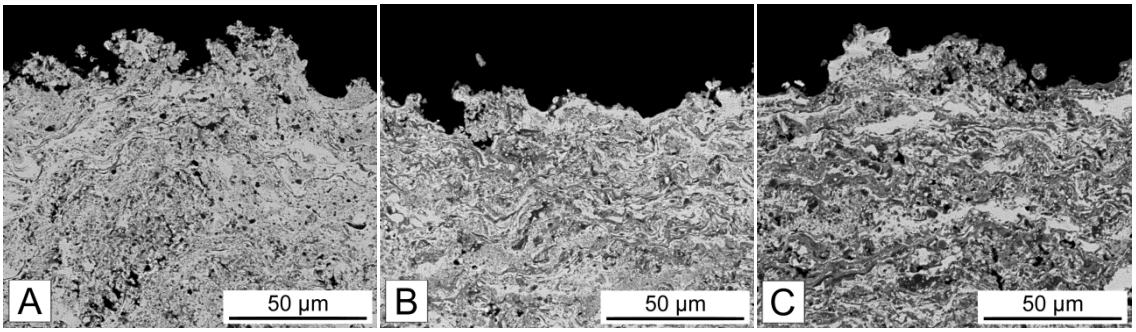

Figure 3.1.63 – High magnification SEM pictures of the coatings Z10-f (a), Z20-f (b) and Z30-f (c), deposited by HVOF using methane as a fuel gas instead of hydrogen.

Samples	Al_2O_3 amount (wt.%)	Percent porosity
Z10-f	10	1.1
Z20-f	20	0.7
Z30-f	30	3.1

Table 3.1.39 – Description of the samples deposited using methane as fuel gas and their percent porosity.

Previous investigations demonstrated that using methane instead hydrogen permitted to obtain dense coating as well. The spraying parameters were optimized by M. Okada *et al.* [7], in order to improve the density of the final full ODS coatings.

The SEM micrographs reveal that these coatings are homogenous and their microstructure is very similar to that of the samples analyzed previously. The porosity is slightly higher compared to coatings deposited using hydrogen.

Future perspectives

Since the ODS coatings developed in this investigation are dense and have a homogenous microstructure they could also be used for anti-wear applications.

The addition of oxide particles could effectively improve the high temperature wear resistance of those systems.

The wear resistance at high-temperature of composite systems could be affected by the presence of hard inclusions and by the development of a protective oxide scale on the external surface. therefore, the mechanisms of wear and the behavior of such coatings need to be carefully investigated, by using a ball on disc tribometer.

Ware tests will be performed at different temperatures and the results (*i.e.* volume of the wear tracks, friction coefficient, wear debris analysis) will be compared to that obtained after testing a standard bondcoat.

References

[1] J.S. Benjamin, T.E. Volin, The Mechanism of Mechanical Alloying, Metall. Trans. 5 (1974) 1929-1934.

[2] C. Suryanarayana, Mechanical Alloying and Milling, Prog. Mater. Sci. 46(1-2) (2001) 1-184.

[3] M. Tahari, M. Shamanian, M. Salehi, Microstructural and morphological evolution of MCrAlY/YSZ composite produced by mechanical alloying method, J. Alloys Compd. 525(5) (2012) 44-52.

[4] S. Todde, R. Licheri, R. Orrù, G. Cao, Spark Plasma Sintering of Cryomilled CoNiCrAlY Powders, Chemical Engineering Transactions 24 (2011) 1501-1506.

[5] E.A.G. Shillington, D.R. Clarke, Spalling Failure of a Thermal Barrier Coating Associated with Aluminum Depletion in the Bond-coat, Acta Mater. 47(4) (1999) 1297-1305.

[6] A. Rabiei, A.G. Evans, Failure Mechanisms Associated with the Thermally Grown Oxide in Plasma-Sprayed Thermal Barrier Coating, Acta Mater. 48 (2000) 3963-3976.

[7] M. Okada, R. Vaβen, M. Karger, D. Sebolt, D.E. Mack, M.O. Jarligo and F. Bozza, Deposition and Oxidation of Oxide-dispersed CoNiCrAlY Bondcoats, J. Therm. Spray Technol. 23(1-2) (2014) 147-153.

3.2 Development of Cr-rich diffusion coatings

This section concerns the investigation of the mechanisms of formation of Cr-rich diffusion coatings, obtained by using the pack-chromizing process.

Samples were prepared by varying the pack-mix composition and the duration of the pack-cementation process.

A list of the coatings and their descriptions is given in table 3.2.1.

Sample name	Cr (wt.%)	NH_4Cl (wt.%)	Al_2O_3 (wt.%)	Isothermal stage (h)
C10A1t12	10	1	Bal.	12
C10A2t0	10	2	Bal.	0*
C10A2t12	10	2	Bal.	12
C10A1t24	10	1	Bal.	24
C10A2t24	10	2	Bal.	24
C25A2t12	25	2	Bal.	12
C25A2t24	25	2	Bal.	24
C25A5t12	25	5	Bal.	12
C25A5t24	25	5	Bal.	24

Table 3.2.1 – Pack-mix compositions and pack-chromizing parameters.

* the 0 hours isothermal stage was performed by heating the samples up to the process temperature (1100°C) and immediately cooling them down to room temperature, by switching of the furnace (fig. 3.2.1).

This thermal treatment was performed in order to investigate the chemical reactions and the diffusion mechanisms that may occur during the transient stages.

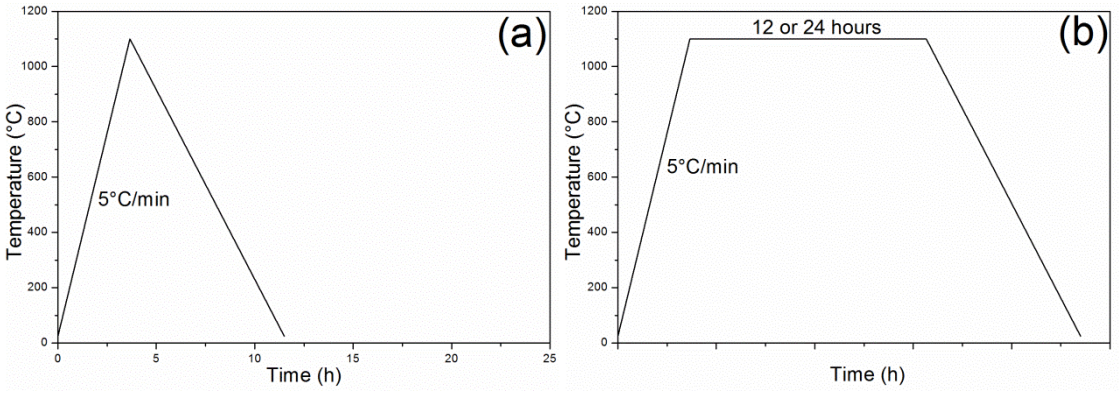

Fig. 3.2.1 – Schematic representation of the thermal cycle for the pack-chromizing process: (a) only heating and cooling steps; (b) 12 or 24 hours thermal treatment.

3.2.1 Analysis of pack-mix components

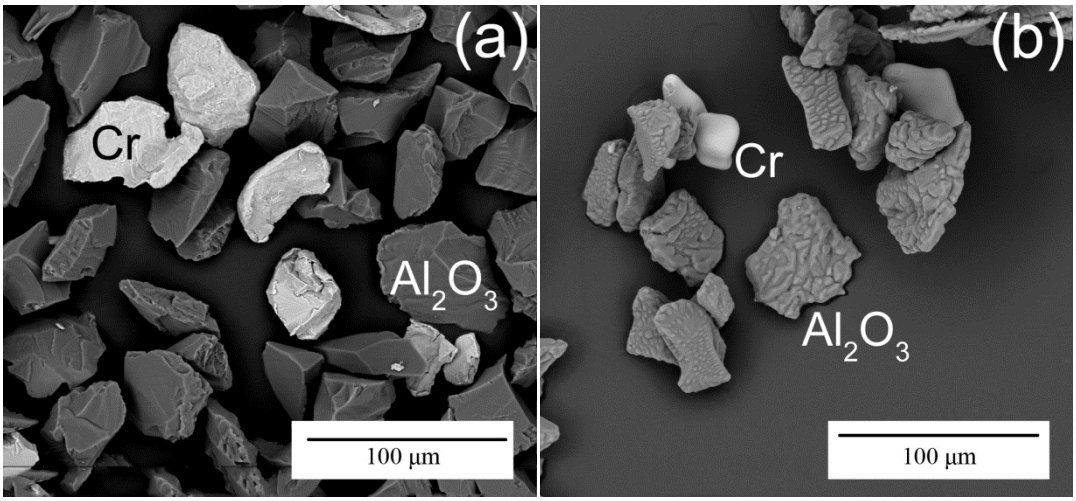

Fig. 3.2.2 – SEM micrographs of new (a) and used (b) pack-mix powders. Pack-mix composition: Cr-NH_4Cl-Al_2O_3 10-2-Bal (wt.%).

The comparison between new and used powders clearly shows the transformations occurring to the pack-mix components during the thermal treatment.

The reaction between the activator and the metal source made the chromium particles smoother (compare fig. 3.2.2b to fig. 3.2.2a) and caused inward diffusion of nitrogen (fig. 3.2.3c and corresponding EDX spectra in fig. 3.2.3d: spectrum 1 and 2). The Cr particles also exhibit an external region slightly enriched in iron after the chromizing treatment (fig. 3.2.3c and corresponding EDX spectra in fig. 3.2.3d: spectrum 1). This element came from the stainless steel retort: during the thermal treatment, it was able to form a vapor phase and diffuse inward on the surface of the Cr particles.

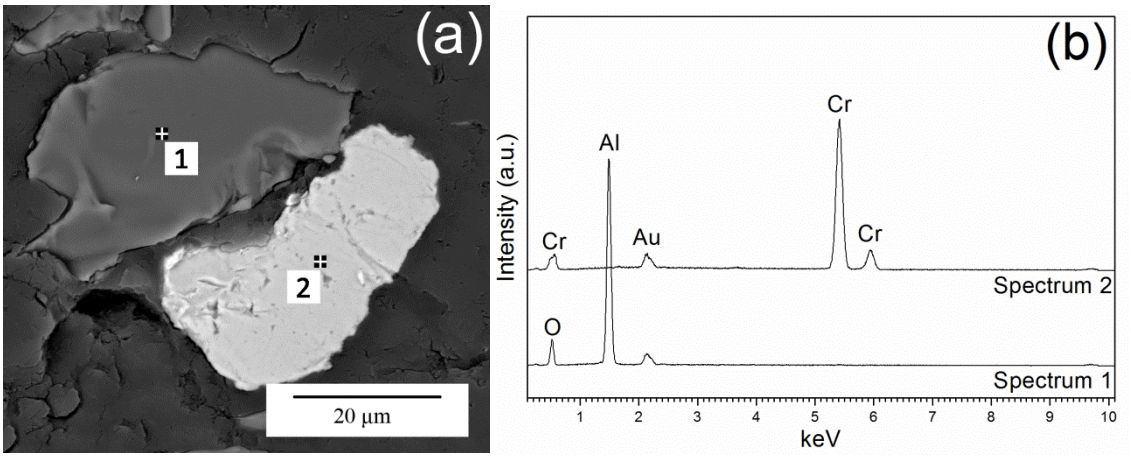

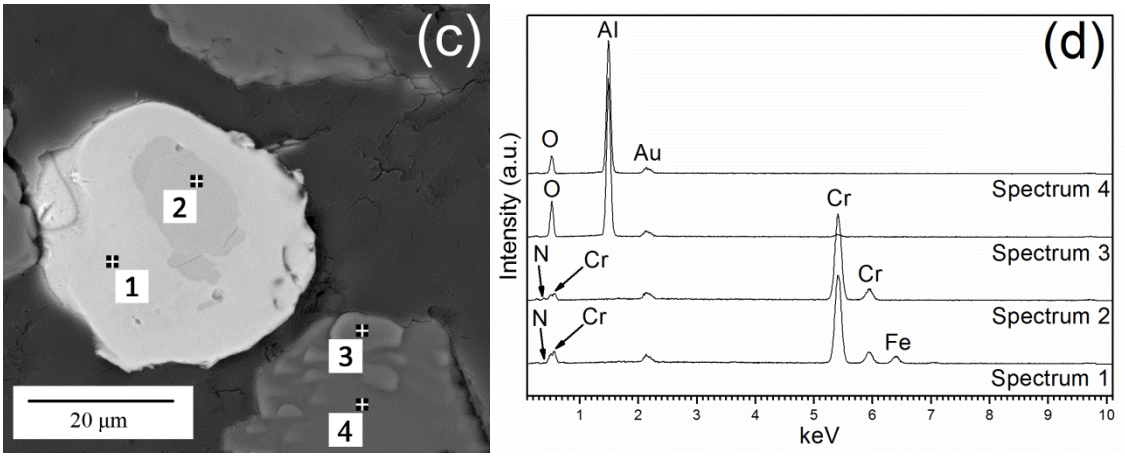

Fig. 3.2.3 – SEM micrographs (cross sections) and EDS spectra of new (a),(b) and used (c),(d) pack-mix powders. Pack-mix composition: Cr-NH_4Cl-Al_2O_3 10-2-Bal (wt.%).

The reactions occurring during the pack-chromizing cycle also affected the inert filler: the interaction between the activator and the aluminum oxide [1,2] probably led to deposition and inward diffusion of chromium atoms inside the alumina particles (fig. 3.2.3c and corresponding EDX spectrum in fig 3.2.3d: spectrum 3), increasing their roughness as well (compare fig. 3.2.2b to fig. 3.2.2a).

3.2.2 Coating analysis

The SEM and EDS analysis performed on the sample C10A2t0 (*i.e.* subjected to a chromizing treatment without isothermal stage) allowed to evaluate the transformations that occurred during the heating and the cooling stages only.

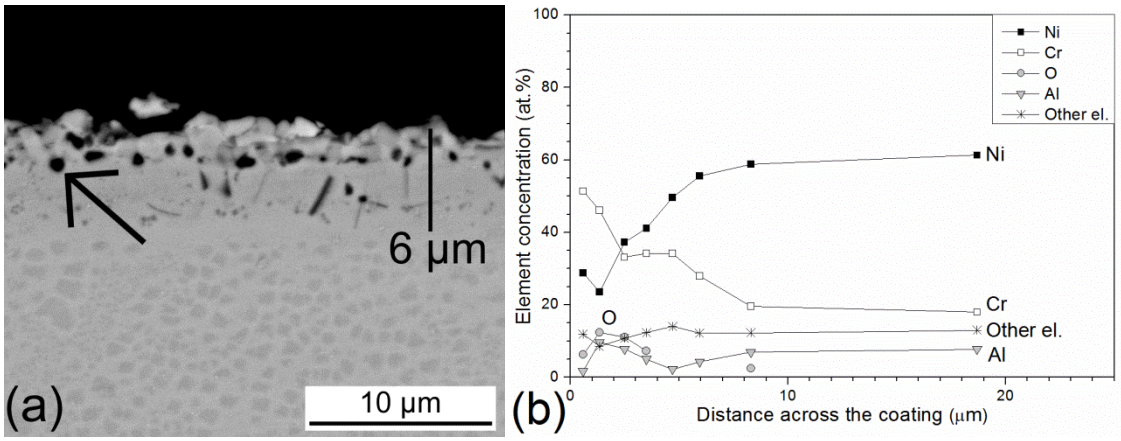

Fig. 3.2.4 – SEM micrograph of sample C10A2t0 (a) and concentration profiles of the elements as a function of the distance from the coating surface (b). The arrow indicates the alumina-rich particles formed due to secondary reactions that occurred in the pack-mix during the heating and cooling steps.

Figure 3.2.4 shows that, during these stages (*i.e.* at temperatures below 1100°C), the activator started to react with the metal source, leading to the formation of a thin chromium-rich layer on the outer surface of the component. The arrow in figure 4a points out to the presence of alumina-rich particles, probably caused by the secondary reactions among the NH_4Cl decomposition products and the inert filler discussed in *Section 3.2.1*, which may have caused the transport of some oxidized aluminum onto the sample surface or the direct oxidation of the aluminum contained in the Inconel738 alloy. Oxygen may have indeed been displaced from the inert filler and transported to the sample surface, where it reacted with Al on account of its highest affinity towards that element at high temperature.

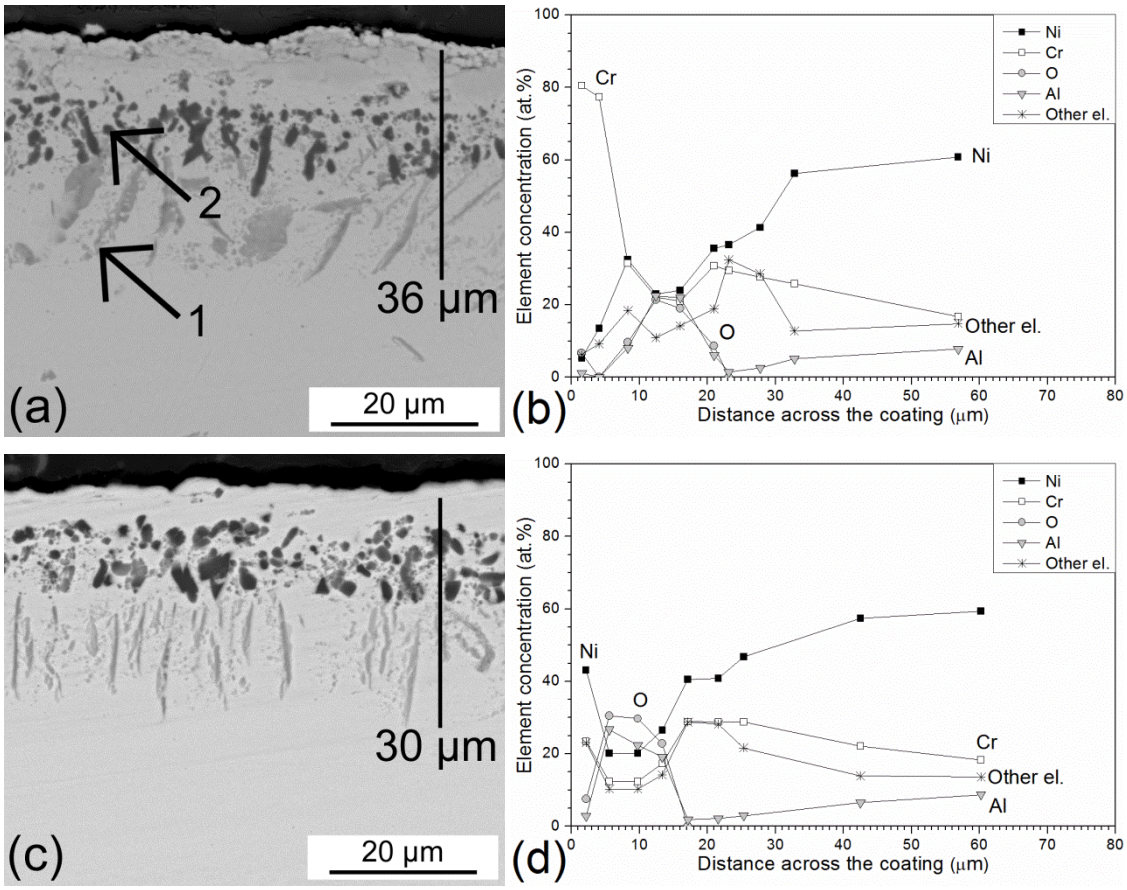

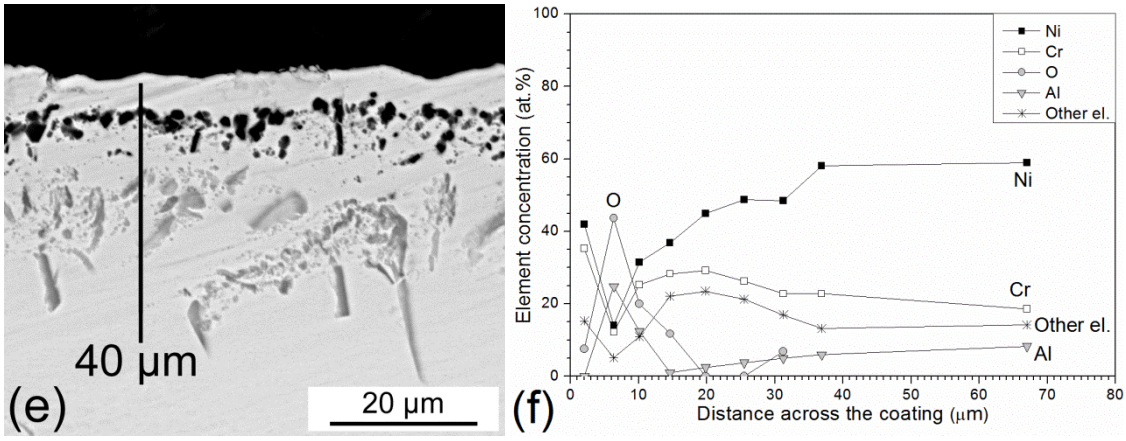

Fig. 3.2.5 – SEM micrographs and concentration profiles of pack-chromized samples: (a),(b) C10A2t12; (c),(d) C10A2t12-HT; (e),(f) C10A1t12. Arrow 1 indicates the Ti,Cr carbides and nitrides; Arrow 2 indicates the alumina-rich particles.

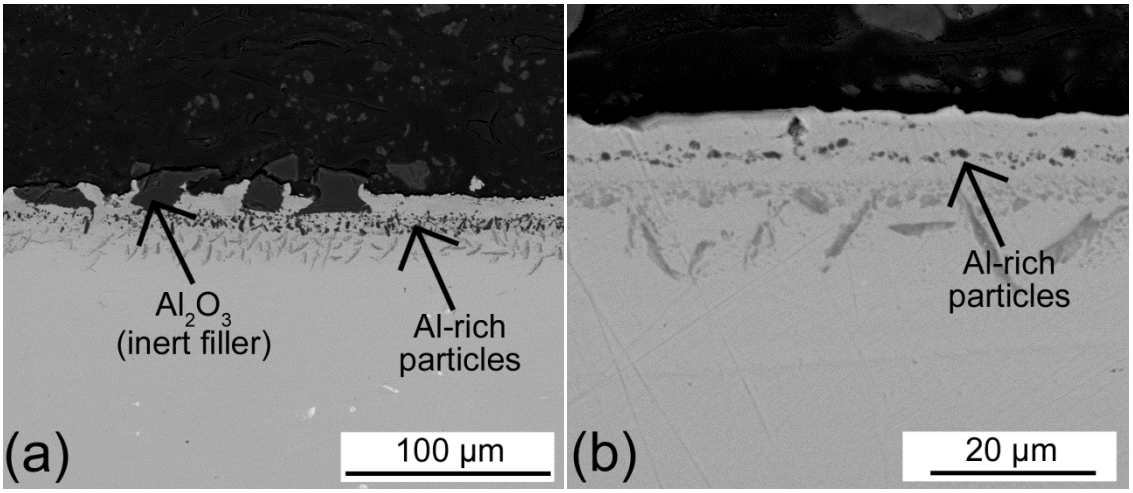

Fig. 3.2.6 – SEM micrograph of pack-chromized sample C10A2t12 (a), showing embedded inert particles (Al_2O_3) and an Al-rich layer, and SEM micrograph of the sample treated by an above-the-pack process with the same cycle (b), showing Al-rich layer but no embedded inert particle.

During the 12 hour-isothermal stage, Cr continued to be transported to the sample surface and, simultaneously, it interacted with the base alloy elements, leading to the formation of a fully developed chromized layer. Specifically, the chromium deposited onto the sample surface diffused inward while nickel simultaneously diffused outward: the resulting coating is therefore based on (i) a 5 µm-thick external layer (fig. 3.2.5a,b) and (ii) two precipitate-rich inner layers (fig. 3.2.5a, labels 1 and 2). Going into details of each constituent:

(i) In the outer layer, some alumina particles from the pack-mix (fig. 3.2.6a) were also entrained. They are clearly recognizable and distinguishable from the previously mentioned alumina-rich particles (also marked in fig. 3.2.6a for better clarity) because of their larger size and angular morphology. It is therefore inferred that, during the first steps of the diffusion

process, the reaction front that controls the growth of the coating moved outward, which means that the Cr deposition rate was higher than its inward diffusion rate. This is consistent with the previous observations made on sample C10A2t0, *i.e.* a surface layer extremely rich in Cr is formed during transient stages at T < 1100 °C. As these entrained alumina particles are not evenly distributed across the sample, it is possible to find areas where many of these particles are present (as in fig. 3.2.6a) as well as areas where none is present (as in fig. 3.2.5a).

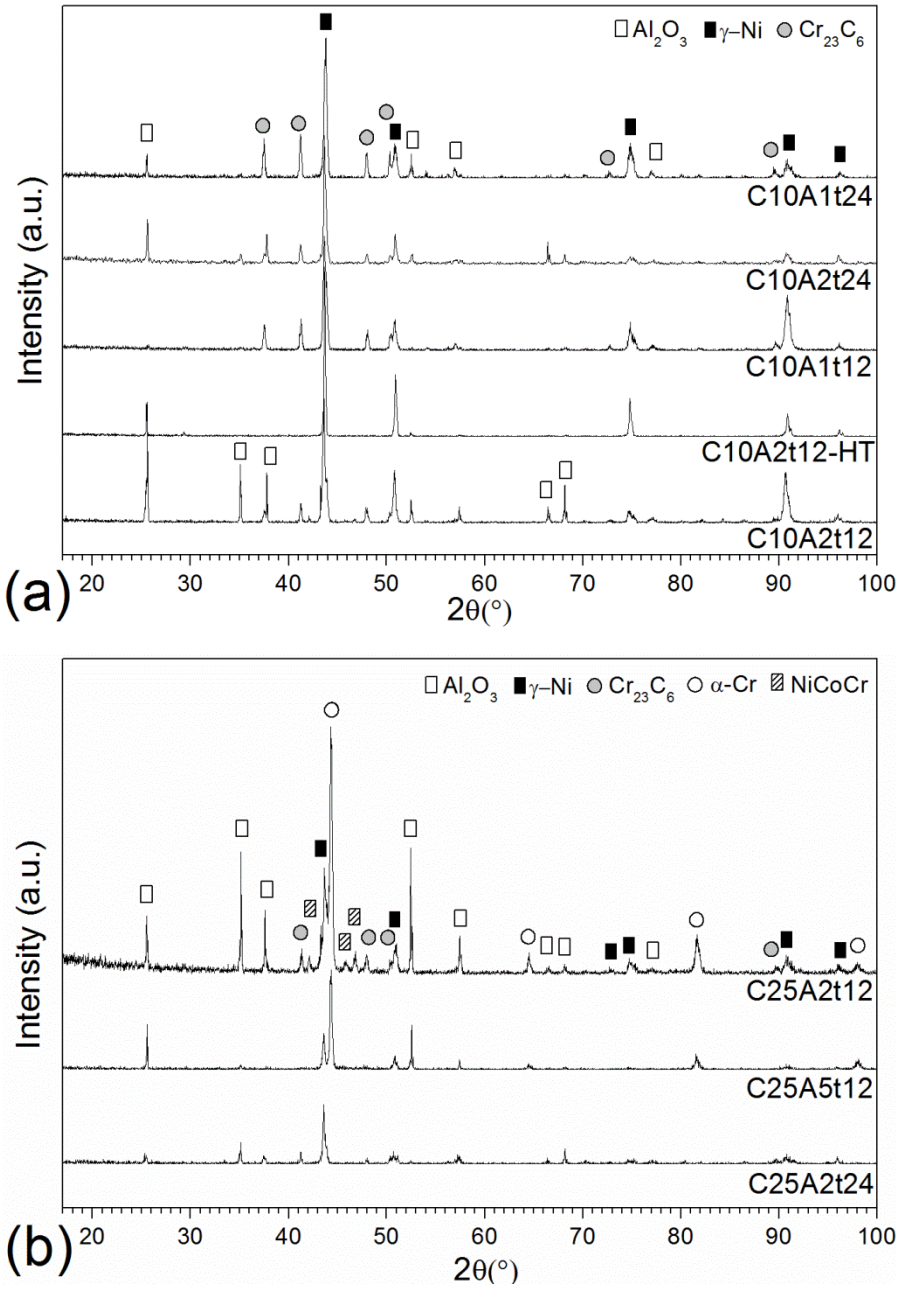

Fig. 3.2.7 – XRD patterns of the samples coated using a pack-mix containing 10 (a) and 25 (b) wt.% of Cr powder.

The XRD analysis (fig. 3.2.7a), apart from the obvious peaks of α-Al_2O_3 resulting from the embedded inert filler particles, shows the presence of two different phases within the external layer of the C10A2t12 chromized sample: γ-Ni and $Cr_{23}C_6$. The latter phase grew due to the reaction of Cr with carbon contained in the alloy: C probably diffused outward together with Ni during the isothermal period. The Cr-based carbide particles are also recognizable in SEM+EDS analyses performed on the electrochemically etched coating cross-section (fig. 3.2.8, label 1): they indeed stand slightly proud of the etched surface and look somewhat brighter in the secondary electron SEM micrographs (fig. 3.2.8). They are surrounded by a Ni,Cr-based phase (fig. 3.2.8, label 2) which clearly corresponds to the γ-Ni phase detected in the XRD patterns (fig. 3.2.7a). Consistently with the expectations put forward in the Introduction, this phase contains significant amounts of dissolved Cr. For this reason, this phase will be hereafter referred to as a γ-(Ni,Cr) solid solution.

Element concentration profiles (fig. 3.2.5a,b) confirm that the very surface of the chromized sample contains very little Ni (7 at. %), because of the formation of Cr-based carbides. Its concentration increases immediately below this layer, where more γ-(Ni,Cr) solid solution phase is found. This is caused by the outward movement of Ni during the prolonged isotherm period, made possible by the mobility of this element at the chosen process temperature, as demonstrated by several investigations performed on pack-aluminized coatings treated at temperature above 1000 °C [3-5].

(ii) Underneath the outer Cr-rich layer, the first precipitate layer contains small, rounded aluminum oxide-rich particles (fig. 3.2.5a, label 2 and fig. 3.2.6a). They were formed during the pack-chromizing process because of secondary reactions among some pack-mix components, including the inert filler, as mentioned previously. Those particles are not the result of a direct entrainment from the powder mixture.

Accordingly, this alumina-rich precipitate region is also found in coatings obtained by the above-the-pack process, where the Inconel 738 substrate was not in direct contact with the pack-mix components (fig. 3.2.6b).

The second precipitate layer, below the alumina-rich region, is mainly based on titanium and chromium carbides and nitrides (fig. 3.2.5a, label 1), which are clearly distinguishable on etched cross-sections as well (fig. 3.2.8). The formation of these phases is probably caused by the precipitation of Ti and Cr out of the Ni matrix, as Ni is depleted in this region by outward diffusion towards the chromized area. Ni depletion indeed decreases the solubility limit of Cr and Ti. Some Cr may also have diffused into this region from the outer chromized layer.

Precipitation was followed by the reaction of these elements with carbon and nitrogen: the latter came from the dissociation of the activator (NH_4Cl) and, due to its very high mobility, it could easily diffuse inward up to a significant depth below the sample surface.
Below the second precipitate layer, the superalloy substrate gradually recovers its normal γ – γ' two-phase structure (fig. 3.2.8).

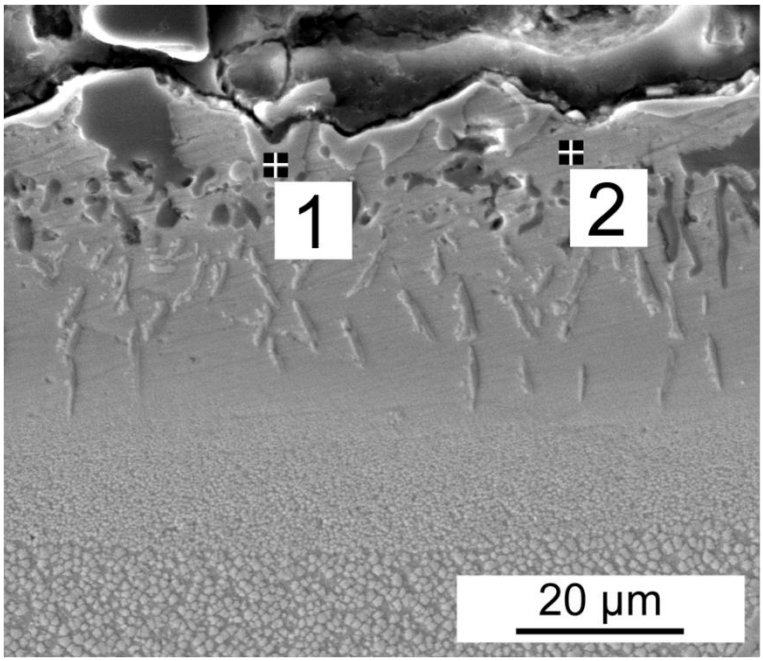

1		
Element	**Wt.%**	**At.%**
Ni	10.45	9.19
Cr	71.84	71.33
O	2.91	9.38
Al	-	-
Other	14.80	10.10

2		
Element	**Wt.%**	**At.%**
Ni	38.99	32.97
Cr	38.55	37.39
O	3.88	12.23
Al	0.93	1.73
Other	17.65	15.68

Fig. 3.2.8 – SEM micrograph of the electrochemically etched cross-section of sample C10A2t12.

Fig. 3.2.5c,d show sample C10A2t12 after the diffusion treatment (hereafter labeled C10A2t12-HT, where HT stands for *"heat treated"*), carried out in a vacuum atmosphere. The coating thickness remained almost constant and no major changes in the microstructure are observed. This probably occurred because the thermal treatment, carried out for only 2 hours at the same temperature of the pack-chromizing process, did not lead to large morphological alterations, even if the process was performed in a Cr-free atmosphere.
It is however observed that, during the vacuum process, further outward diffusion of Ni occurred: in the first microns of the outer region, the Cr content changed from 80 at. % (fig. 3.2.5b) to 25 at % (fig. 3.2.5d), whereas the Ni amount increased from 7 at.% to 45 at %. As a consequence, the $Cr_{23}C_6$ carbide phase was dissolved in the γ-Ni matrix and it is no longer identifiable in the XRD patterns (fig. 3.2.7a).
The interdiffusion movements also caused the resolubilization and re-organization of a limited amount of the carbides and nitrides in the second precipitate layer (fig. 3.2.5c).

Decreasing the activator content from 2 to 1 wt. % (sample C10A1t12, fig. 3.2.5e,f) resulted in a reduced amount of vapor phase formed during the pack-chromizing process, so that fewer Cr is available for the inward diffusion process. As a consequence, the reaction front that controls the growth of the external layer mainly moved inward, as demonstrated by the XRD pattern (fig. 3.2.7a), where the peaks of the α-Al_2O_3 phase were not detected. This also confirms that those peaks are due to embedded filler particles, not to the first alumina-rich precipitate layer. The latter, indeed, still exists in sample C10A1t12 (fig. 3.2.5e,f).

The lower diffusion rate of chromium and the higher diffusion rate of nickel led to an important reduction of the Cr content in the outer layer and to an increase of the Ni amount (fig. 3.2.5f), whereas the main phases within the outer layer (γ-(Ni,Cr) solution and $Cr_{23}C_6$ carbide, fig. 3.2.7a) and the precipitates morphology (fig. 3.2.5e) remain almost unaltered. The significant outward diffusion of Ni also caused the overall thickness of the coating to remain unaltered, as a thick precipitate layer was formed in these conditions as well.

3.2.3 Effect of the isothermal stage duration

With a pack-mix containing 2 wt. % of activator, changing the duration of the isothermal stage (from 12 to 24 hours) led to an increase of the amount of Ni diffusing up to the outer layer and simultaneously gave the inward-diffusing Cr sufficient time to move deeper below the sample surface. Due to these interdiffusion phenomena, the C10A2t24 coating (fig. 3.2.9a) is therefore thicker than the C10A2t12 coating (fig. 3.2.5a). In its outer layer, the Cr content also decreased to 35 at. % and that of Ni increased up to 45 at. % (fig. 3.2.9b), compared to sample C10A2t12 where large concentrations of Cr on the outer surface had been detected (fig. 3.2.5b), as discussed in *Section 3.2.2*.

Comparing samples C10A2t12 and C10A2t24, it is therefore inferred that, at the beginning of the isothermal stage, the deposition of Cr on the outer surface of the samples prevails and the sample grows outward (consistent with the discussion in *Section 3.2.2* and with the presence of alumina peaks in the XRD pattern of the C10A2t24 sample, fig. 3.2.7a), whereas, as the duration of the isothermal stage increases, depletion of the pack mix in both activator and Cr progressively reduces the Cr deposition rate, so that solid-state diffusion rates (including the diffusion of Ni to the top surface and that of Cr into the sample) prevail over the deposition rate.

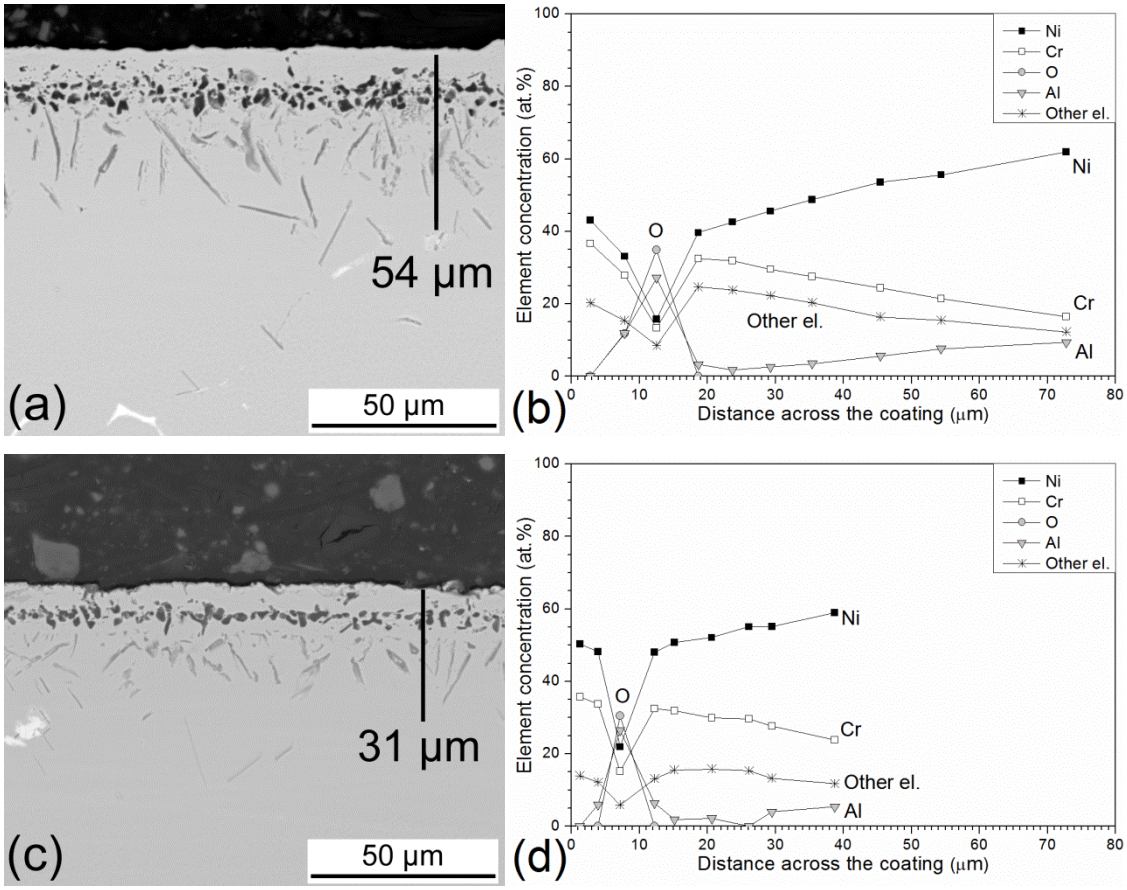

Fig. 3.2.9 – SEM micrographs and concentration profiles of samples after a 24-hours pack-chromizing process: (a),(b) C10A2t24; (c),(d) C10A1t24.

Despite this, the main phases of the outer layer remain the same, as shown in the XRD pattern (fig. 3.2.7a). SEM observations of the electrochemically etched cross-section also confirm the presence of Cr-rich areas (fig. 3.2.10, label 1), corresponding to the $Cr_{23}Cr_6$-based carbides (fig. 3.2.7a), and of a γ-(Ni,Cr) solid solution (fig. 3.2.10, label 2). The $Cr_{23}C_6$ phase, however, does not form a nearly uniform layer on the top surface (unlike the C10A2t12 sample, fig. 3.2.8); it is rather distributed in somewhat lower amount inside the γ-phase matrix (fig. 3.2.10), consistent with the higher amount of Ni as seen in fig. 3.2.9b.

After the heat treatment in a vacuum atmosphere, the morphology and the distribution of the elements inside the C10A2t24 coating are similar to the ones observed inside the C10A2t12 sample.

Unlike the sample C10A2t24, the thickness of the coating C10A1t24 did not increase (fig. 3.2.9c): probably, because of the lower amount of activator in the pack-mix (1 wt. % instead of 2 wt. %), the amount of Cr deposited onto this sample was not as large as in the former one. The Cr deposition rate eventually became very low, so that the carbides and nitrides

within the inner precipitate layer were partially re-dissolved in the matrix as Ni diffused from the underlying superalloy.

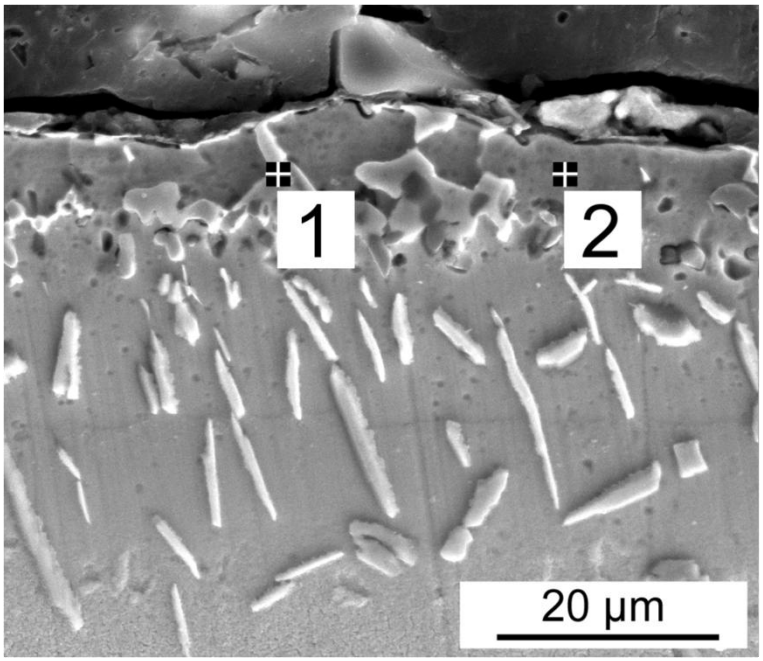

1		
Element	**Wt.%**	**At.%**
Ni	5.09	4.72
Cr	76.79	80.83
O	-	-
Al	2.61	5.26
Other	15.51	9.19

2		
Element	**Wt.%**	**At.%**
Ni	43.36	39.32
Cr	32.65	33.43
O	1.87	6.23
Al	0.70	1.39
Other	21.32	19.63

Fig. 3.2.10 – SEM micrograph of the electrochemically etched cross-section of sample C10A2t24.

The characterization tests, therefore, demonstrate that the effect of the activator amount and the process time are strongly correlated, showing that the microstructure and the coating thickness depend on the interaction between these two parameters.

3.2.4 Effect of the Cr amount

Increasing the amount of chromium powder into the pack-mix from 10 wt.% to 25 wt.% brought to an increase of the Cr partial pressure in the vapor phase, as already demonstrated in case of pack-cementation processes using aluminum as metal source [4]. Therefore, after a 12 hour-long pack-cementation treatment, the outer layer of sample C25A2t12 is mainly based on α-Cr phase (XRD pattern in fig. 3.2.7b), differently from sample C10A2t12 (fig. 3.2.7a and *Section 3.2.2*). Etched cross-sections (fig. 3.2.11) indeed show a significantly different morphology from that previously observed on the γ-(Ni,Cr) + α-Cr_3C_2 layers seen in *Section 3.2.2* and *3.2.3* (figs. 3.2.8, 3.2.10). In this case, the rate of Cr deposition from the vapor phase onto the outer surface far surpassed the inward diffusion rate of Cr itself and the outward diffusion rate of Ni from the superalloy.

Due to the thicker outer layer (now based on α-Cr), the overall thickness of the whole chromized layer increases (compare sample C25A2t12, fig. 3.2.12a, to sample C10A2t12, fig. 3.2.5a).

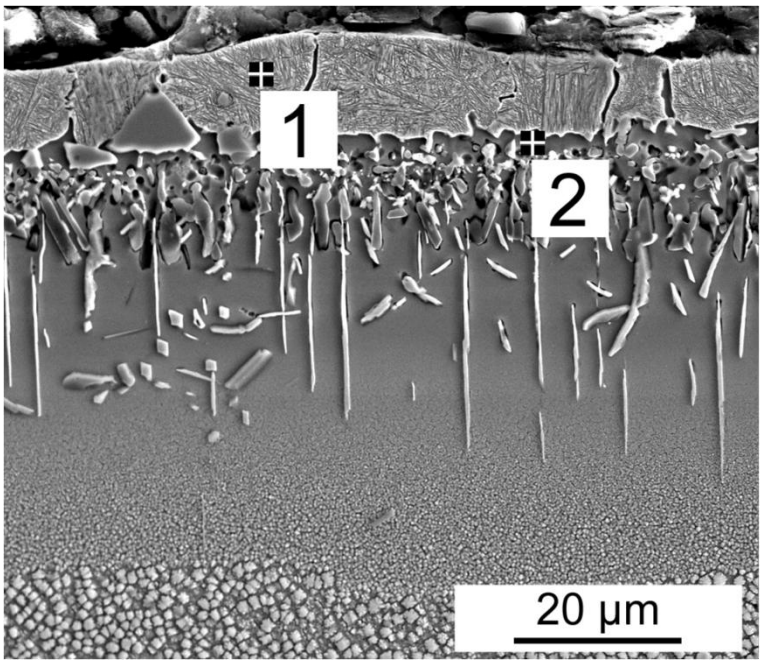

1		
Element	**Wt.%**	**At.%**
Ni	14.70	13.08
Cr	68.84	68.79
O	2.31	7.55
Al	-	-
Other	14.15	10.58

2		
Element	**Wt.%**	**At.%**
Ni	44.78	43.01
Cr	40.49	43.92
O	-	-
Al	-	-
Other	14.73	13.07

Fig. 3.2.11 – SEM micrograph of the electrochemically etched cross-section of sample C25A2t12.

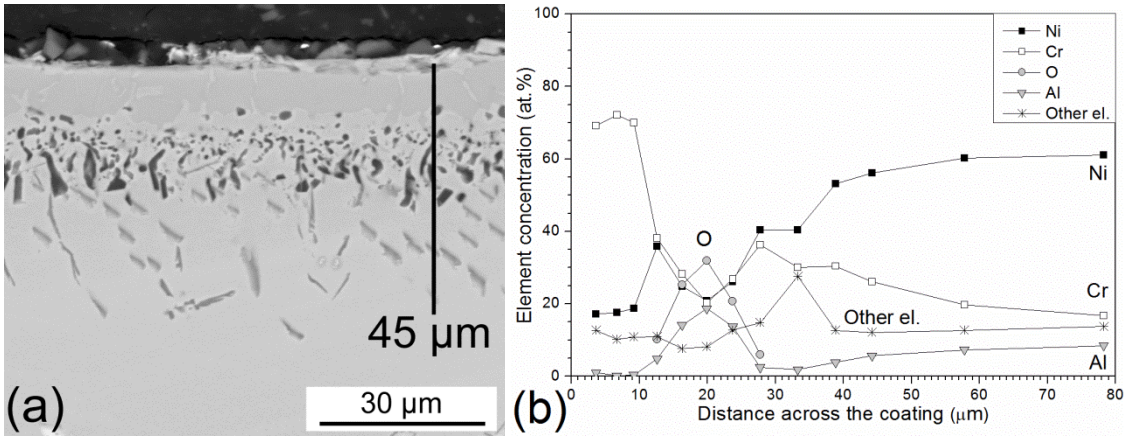

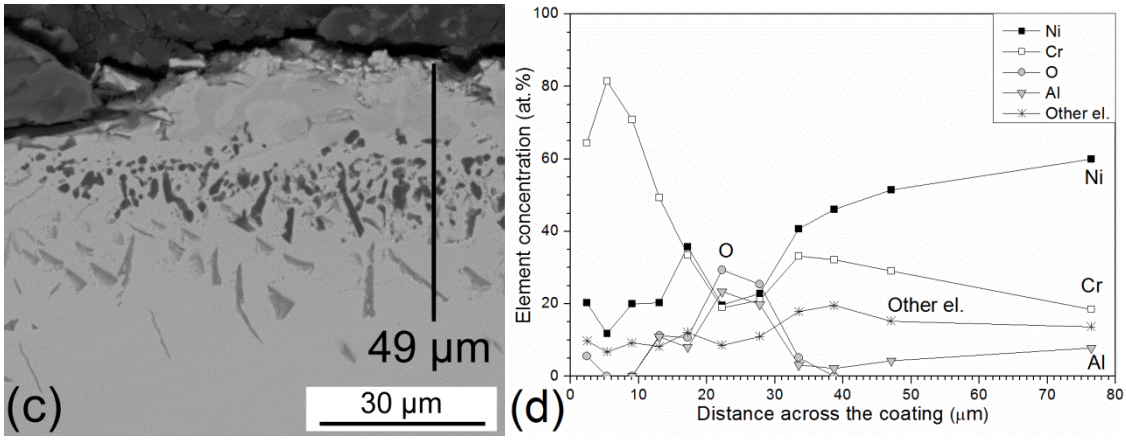

Fig. 3.2.12 – SEM micrographs and concentration profiles of samples C25A2t12 (a,b) and C25A2t24 (c,d).

After 24 h of isothermal treatment (sample C25A2t24), Ni and C from the bulk alloy can diffuse in substantial amounts towards the Cr-rich outer layer. In accordance with the previous discussion in *Section 3.2.3*, as the isothermal stage progresses, the partial pressure of the vapor phase decreases so that solid state diffusion rates eventually equal or surpass the Cr deposition rate. The phase composition of the outer layer accordingly reverts back to $Cr_{23}C_6$ and γ-(Ni,Cr) (XRD pattern in fig. 3.2.7b). $Cr_{23}C_6$ carbides and the surrounding γ-(Ni,Cr) matrix are recognizable again on etched cross-sections (fig. 3.2.13).

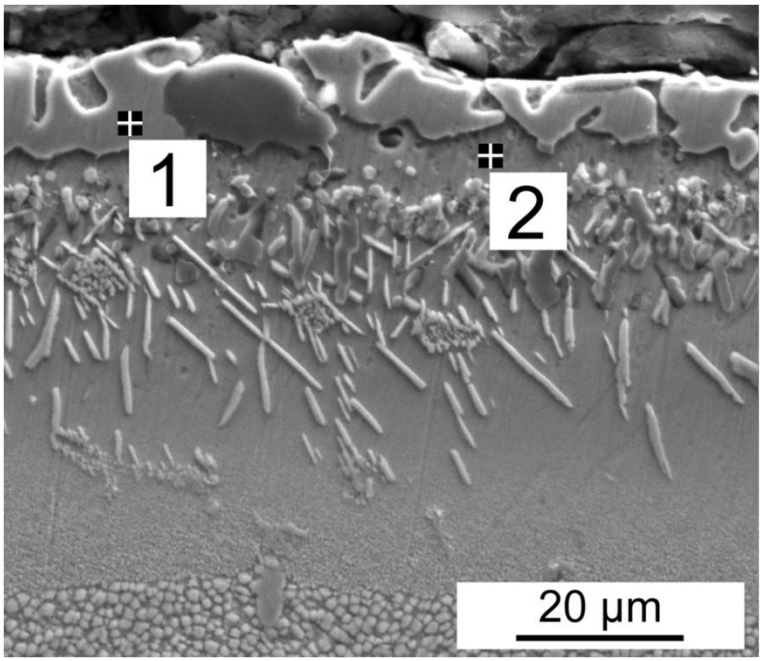

1		
Element	**Wt.%**	**At.%**
Ni	4.95	4.69
Cr	82.32	88.09
O	-	-
Al	-	-
Other	12.73	7.22

2		
Element	**Wt.%**	**At.%**
Ni	44.63	42.42
Cr	38.50	41.32
O	-	-
Al	0.50	1.04
Other	16.37	15.22

Fig. 3.2.13 – SEM micrograph of the electrochemically etched cross-section of sample C25A2t24.

Nonetheless, sample C25A2t24 (fig. 3.2.12c,d) differs significantly from sample C10A2t24 (fig. 3.2.9a,b), which was obtained with a 24 h-isotherm using 10 wt.% Cr powder. The external layer, though consisting of $Cr_{23}C_6$ and γ-(Ni,Cr) in both cases (fig. 3.2.7b, 3.2.13 and

fig. 3.2.7a, 3.2.10, respectively), is somewhat thicker and richer of inert particles for sample C25A2t24. The Cr content in the external layer rose from 34 to 70 at. %, which means the outward diffusion of Ni during the 24 h-long isotherm stage did not completely compensate for the much larger amount of Cr initially deposited from the vapor phase, though it could restore the same phase composition.

The Cr amount in sample C25A2t24 strongly decreases at 15 μm below the surface and, at 30 μm, its concentration is very similar to the values of the sample C10A2t24, as is the overall thickness of the whole chromized layer. The overall coating thickness, indeed, strongly depends on the thickness of the second precipitate layer, which is controlled by the outward diffusion of nickel. The latter was probably able to re-dissolve some of the precipitates as the isothermal stage progressed.

3.2.5 Effect of the activator and Cr amount

In order to study the synergistic effects of the amounts of the Cr source and of the activator, samples were treated using a pack-mix based on 25 wt.% of Cr source and 5 wt.% of NH_4Cl activator.

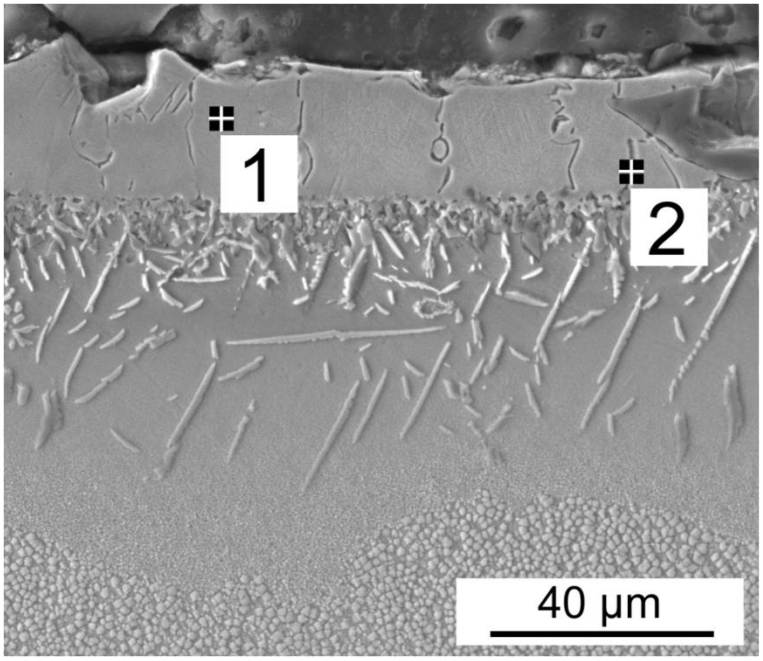

1		
Element	**Wt.%**	**At.%**
Ni	14.25	12.73
Cr	69.69	70.29
O	1.41	4.62
Al	-	-
Other	14.65	12.63

2		
Element	**Wt.%**	**At.%**
Ni	34.03	31.19
Cr	49.43	51.16
O	1.06	3.58
Al	-	-
Other	15.48	14.07

Fig. 3.2.14 – SEM micrograph of the electrochemically etched cross-section of sample C25A5t12.

The chromium deposition rate during the first steps of the pack-cementation process is even larger than in samples deposited using 25 wt.% Cr and 2 wt.% activator (described in Section 3.4) and much higher than the outward diffusion rate of Ni; therefore, after 12 hours, the

external layer of sample C25A5t12 is mainly based on α-Cr (fig. 3.2.14) and even thicker than that of sample C25A2t12 (fig. 3.2.15).

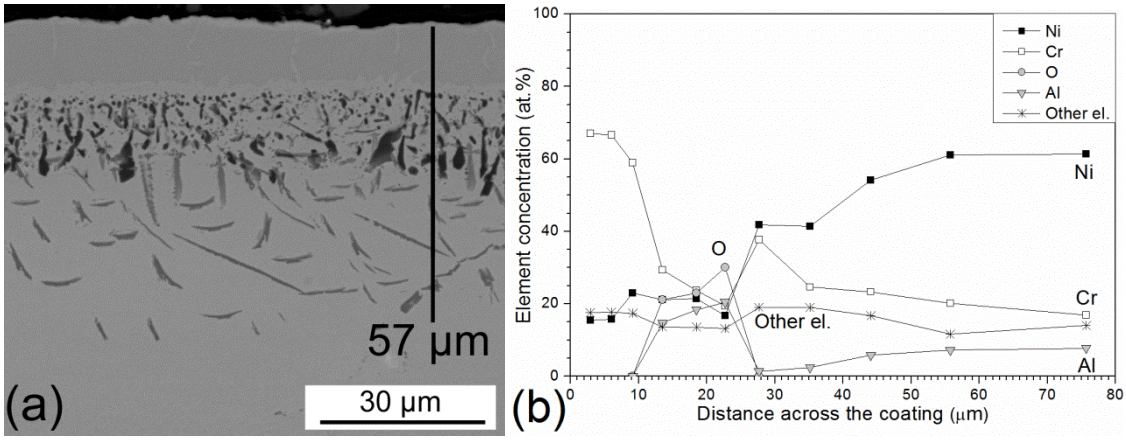

Fig. 3.2.15 – SEM micrograph (a) and concentration profile (b) of sample C25A5t12.

When the isothermal duration is increased to 24 h, the diffusion of Ni starts to become significant again, but the chromized layer of sample C25A5t24 (fig. 3.2.16) is eventually much thicker than that of samples C25A2t24 (*Section 3.2.4*, fig. 3.2.12c) and C10A2t24 (*Section 3.2.3*, fig. 3.2.9a), because of the extremely large amounts of Cr introduced into this sample.

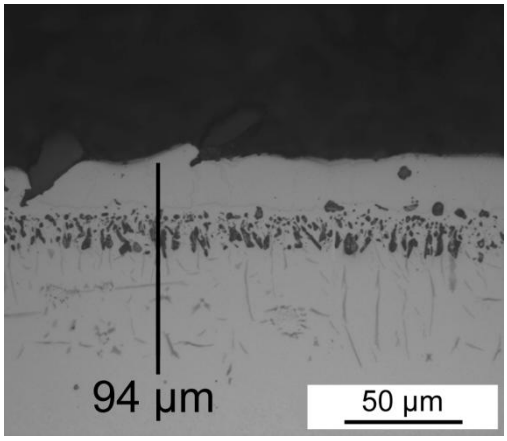

Fig. 3.2.16 – SEM micrograph of sample C25A5t24.

3.2.6 Two step pack-chromizing and aluminizing process

The SEM micrograph in fig. 3.2.17 reveals both an increase in the thickness and changes to the microstructure of the Al-Cr-rich diffusion coating, obtained by a pack-chromizing process followed by pack-aluminizing. These changes are caused by the inward diffusion of a relevant amount of aluminum, which took place during the pack-aluminizing step.

The thickness increase affected both the outer layer and the inner region. The former grew due to the massive aluminum diffusion, which reacted with the main constituents of the Cr-rich coating. Apart from the inward diffusion of Al, some outward growth took place as well; indeed, the thickness of the oxide-free layer above the region based on aluminum-rich oxide particles increased. Accordingly, outward diffusion of nickel took place as well, as demonstrated by the formation of the interdiffusion layer at the interface with the base alloy.

The inward diffusion of Al caused the formation of an Al-rich matrix with secondary Cr-rich phases (Fig. 3.2.18, spectrum 1). The solubility of Cr in the γ-(Ni,Cr) matrix indeed decreases as Ni interacts with Al.

Due to the higher mobility of Al compared to Cr, the aluminized layer also comprises the two precipitates-rich layers described previously. These layers, however, are still distinguishable (fig 3.2.18). No changes occurred to the morphology of the aluminum-rich oxide particles (fig 3.2.18), whereas important transformations affected the titanium and chromium carbides and nitrides. The precipitates formed during the pack-chromizing treatment indeed changed their morphology.

Furthermore, new carbides, mainly based on tungsten, grew in the inner regions of the new coatings, forming a new interdiffusion layer below the aluminized one (fig. 3.2.19).

These new carbides were formed due to the aluminum diffusion, which caused a decrease in the solubility of the alloy elements in the new Al-rich matrix. Since the mobility of Al atoms is way higher than the mobility of Cr atoms, during the pack-aluminizing process, this element was able to diffuse deeper. As a consequence, new W-rich carbides were formed.

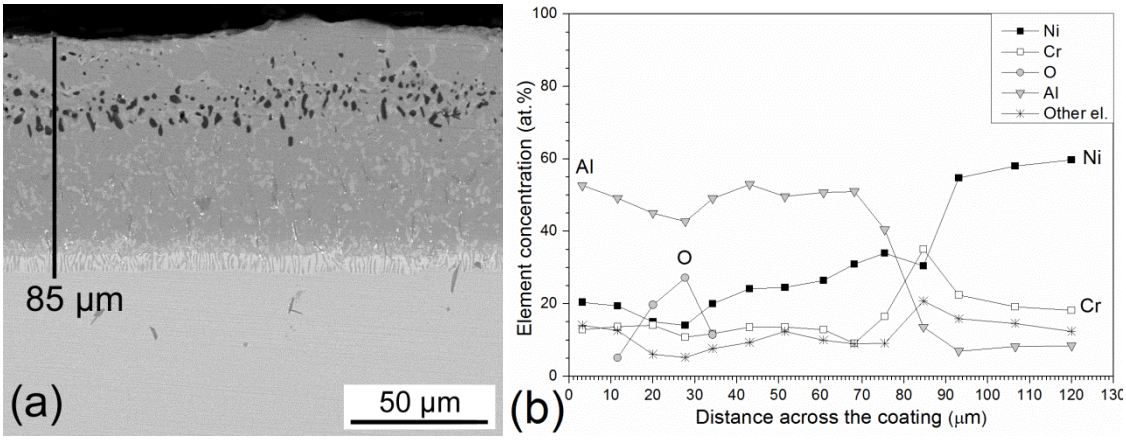

Fig. 3.2.17 – SEM micrograph (a) and concentration profile (b) of sample C10A2t24 after the pack-aluminizing treatment.

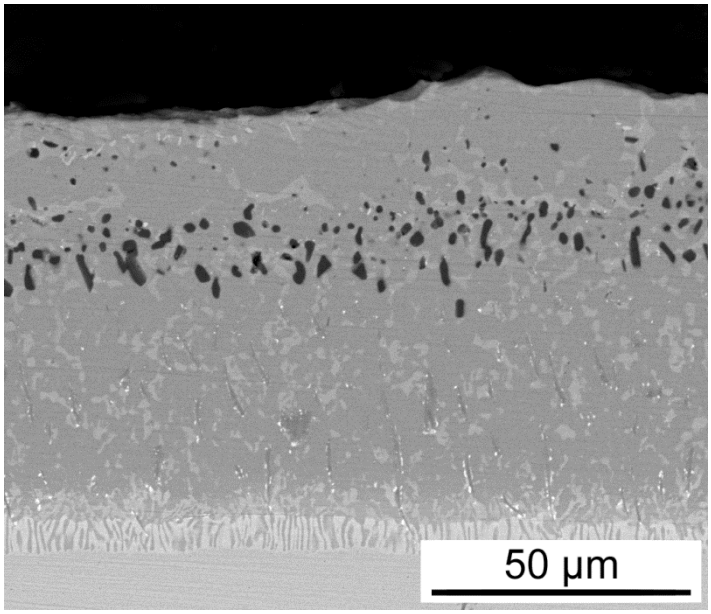

Fig. 3.2.17 – SEM micrograph of the sample C10A2t24
after the pack-aluminizing treatment.

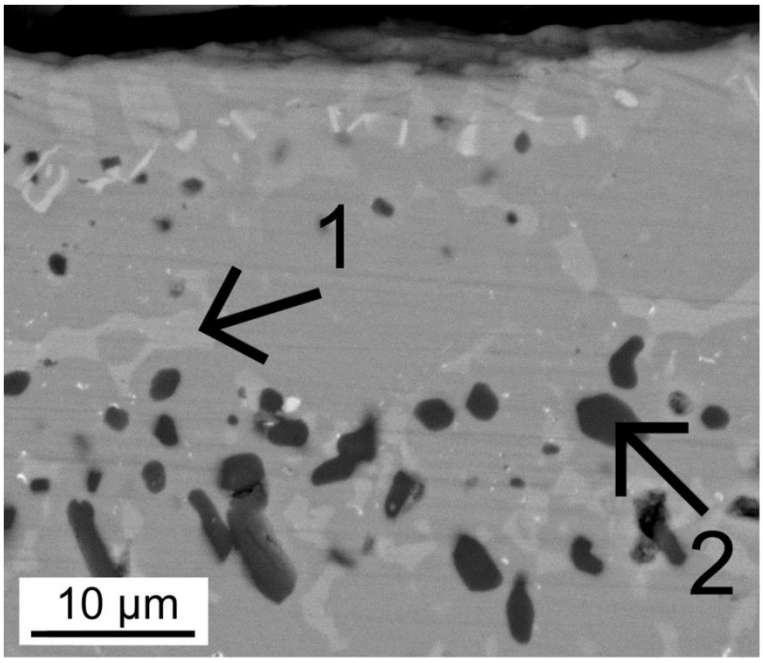

1		
Element	**Wt.%**	**At.%**
Al	22.75	38.45
Cr	60.19	52.79
Fe	3.75	3.06
Ni	2.39	1.86
Mo	4.94	2.35
W	5.98	1.48
2		
Element	**Wt.%**	**At.%**
O	51.64	65.72
Al	42.77	32.27
Cr	1.36	0.53
Fe	0.86	0.31
Ni	3.36	1.16

Fig. 3.2.18 – SEM micrograph of the sample C10A2t24 after the pack-aluminizing treatment. Tables contain the results of the EDS analysis performed on spot 1 and spot 2.

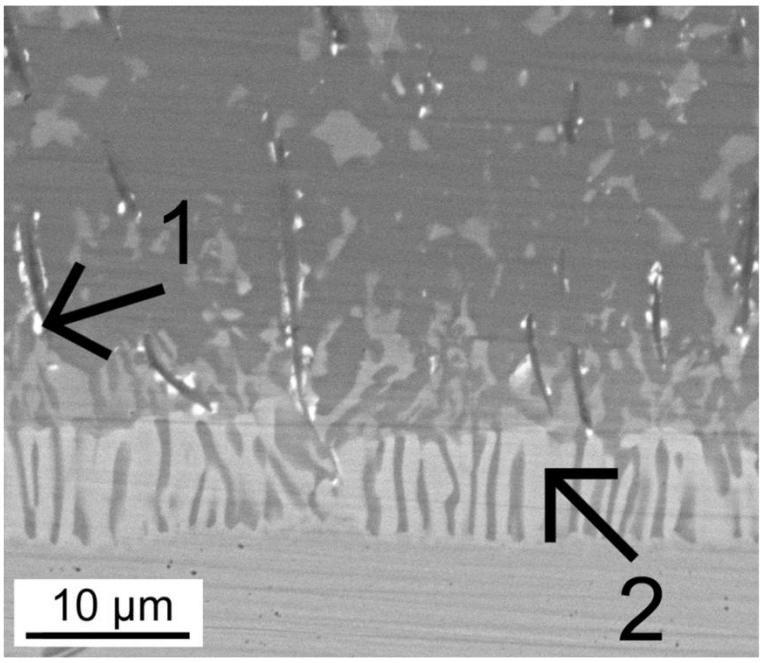

1		
Element	**Wt.%**	**At.%**
Al	8.07	20.91
Ti	16.38	23.92
Cr	11.45	15.40
Ni	18.68	22.25
Ta	41.08	15.87
W	4.35	1.65

2		
Element	**Wt.%**	**At.%**
Al	2.43	5.28
Cr	42.64	48.06
Fe	6.63	6.96
Co	8.13	8.09
Ni	25.15	25.10
Mo	5.92	3.61
W	9.10	2.90

Fig. 3.2.19 – SEM micrograph of the sample C10A2t24 after the pack-aluminizing treatment. Tables contain the results of the EDS analysis performed on spot 1 and spot 2.

Concluding remarks

The characterization of Cr diffusion layers obtained by pack cementation using different parameter sets (including different pack mix compositions and different treatment durations) allowed to understand the effect of process conditions on the formation mechanisms of the chromized layers and on their microstructures.

- First of all, the importance of transient effects occurring below the isothermal treatment temperature is underlined by the formation of a thin, Cr-rich layer on the surface of samples subjected to a heating cycle comprising heating and cooling stages only (with no isothermal holding period). The activator reaction and the resulting Cr transport are triggered at T < 1100 °C, when the diffusion coefficient of Ni is still very low.
- The chromized layers produced after complete treatments consist of a three-layer structure: a Cr-rich outer layer, a first precipitate layer consisting of fine, rounded Al-rich oxides and a second precipitate layer consisting of needle-shaped Ti,Cr-carbides and nitrides.
- The thickness and the chemical and phase composition of the outer layer are the result of the interaction between two simultaneous, competing phenomena: (i) reduction of Cr from the vapor phase onto the sample surface, and (ii) solid state diffusion, including inward

diffusion of Cr and outward diffusion of Ni and C. Diffusion is obviously triggered by the compositional gradient caused by the reduction of Cr onto the sample surface.

- These competing phenomena are strongly influenced by the pack mix composition and by the treatment duration. As long as the pack mix does not contain extremely large amounts of activator (1 wt.% or 2 wt.%), the rates of both processes are quite balanced and the resulting outer layer consists of a γ-(Ni,Cr) matrix containing $Cr_{23}C_6$ phase. As the amount of Cr source and/or of activator in the pack mix are increased (pack mixes containing 10 wt.% or 25 wt.% of Cr powder and 2 wt.% or 5 wt.% of activator), the rate of deposition of Cr prevails over the solid state diffusion rate, at least for short isotherm durations. The chromized layer therefore mainly grows outward, embedding some coarse alumina particles from the pack mix, and its phase composition can eventually change to α-Cr, containing very little Ni.
- In all cases, the rate of deposition from the vapor phase decreases and diffusion processes become comparatively faster as the isothermal duration increases, because of progressive depletion of the pack mix in both the activator and the Cr source. Longer treatments (24 h isotherm duration), therefore, always lead to an overall increase of the Ni content in the outer layer. Even with pack mixes rich in Cr source and activator, the α-Cr outer layer is therefore converted back to γ-(Ni,Cr) + $Cr_{23}C_6$.
- The first precipitate layer, consisting of fine, rounded Al-rich oxides, may originate from additional interactions within the pack mix involving the Al_2O_3 inert filler, which may release oxygen.
- The second precipitate layer (Cr,Ti-based carbides and nitrides) is produced by inward diffusion of Cr and of nitrogen from the outer surface and by the simultaneous precipitation of Cr and Ti out of the original γ – γ' structure of the Inconel substrate as Ni diffuses outwards. Its thickness strongly influences the overall thickness of the whole chromized layer.

Even when process conditions result in a thicker outer layer and/or in its enrichment in Cr, the overall thickness of the chromized layer may therefore not increase, because the diffusion of Ni from the bulk of the sample may favor partial re-solubilization of these precipitates.

The coating produced using a pack-mix based on 10 wt.% of Cr and 2 wt.% of NH_4Cl, together with a 24 hours isothermal stage, was found to be a perfect intermediate step for a subsequent pack-aluminizing process.

Due to the higher mobility of Al, the overall thickness at the end of the two step process increased. The growth of the new coating was controlled by the inward diffusion of Al and the outward diffusion of nickel. Also the carbides-rich region was affected by the diffusion of Al atoms. This results in the change of the precipitates morphology and in the formation of new tungsten-rich carbides.

References

[1] P.N. Walsh, Chemical Aspects of Pack-Cementation, The Electrochemical Society, 1973, pp. 147-168.

[2] H.W. Brill-Edwards, Method for coating heat resistant alloys, United States Patent 3801353, 1974.

[3] G.W. Goward, D.H. Boone, Mechanisms of Formation of Diffusion Aluminide Coatings on Nickel-Base Superalloys, Oxid. Met. 3 (1971) 475-495.

[4] Z.D. Xiang, J.S. Burnell-Gray, P.K. Datta, Aluminide Coating Formation on Nickel-Base Superalloys by Pack Cementation Process, J. Mater. Sci. 36 (2001) 5673-5682.

[5] F. Bozza, G. Bolelli, C. Giolli, A. Giorgetti, L. Lusvarghi, P. Sassatelli, A. Scrivani, A. Candeli, M. Thoma Diffusion mechanisms and microstructure development in pack aluminizing of Ni-based alloys, Surf. Coat. Technol. 239 (2014) 147-159.